(NASA-CR-4138) MODELLING AND CONTROL OF AN ANNULAR MOMENTUM CONTROL DEVICE (SatCon Technology Corp.) 111 p CSCL 13J

N88-20491

Unclas
H1/31 0129409

NASA Contractor Report 4138

Modelling and Control of an Annular Momentum Control Device

James Downer and Bruce Johnson
SatCon Technology Corporation
Cambridge, Massachusetts

Prepared by
SatCon Technology Corporation
for The Charles Stark Draper Laboratory, Inc.
for Langley Research Center under
NASA Contracts NAS9-16023 and NAS9-17560

National Aeronautics
and Space Administration

Scientific and Technical
Information Division

1988

MODELLING AND CONTROL OF AN ANNULAR MOMENTUM CONTROL DEVICE

by

James Downer
Bruce Johnson

ABSTRACT

This document reports research into the modelling and control of an advanced Angular Momentum Control Device (AMCD), used to control the attitude of spacecraft. These systems consist of a angular momentum storage flywheel supported in magnetic bearings. The specific AMCD analyzed is an AMCD Combined Control Energy Storage System (ACCESS). This system presents a challenging control problem because the system dynamics are a strong function of rotaional speed and the open-loop system becomes unstable at high rotational speeds. These open-loop instabilities place minimum and maximum bandwidth and gain requirements on stabilizing controllers.

The stability properties of the closed-loop system are one of the major results of this study. The closed-loop stability properties were analyzed using recently developed control analysis tools for systems described by complex coefficient differential equations. In addition to measures of stability and stability robustness, the research also explicitly determined the stability robustness to variation in plant speed and variation in plant parameters.

Various feedback controllers are investigated including variable-gain, full-state feedback controllers based on linear-quadratic regulators (LQR); fixed-gain, full-state feedback LQRs; output-feedback, model-based-compensators (MBC) designed using fixed-gain Kalman filters as state estimators in conjunction with fixed-gain LQRs; and simple output-feedback, lead-lag compensators. For both the translational and angular dynamics, simple lead-lag compensators acting on parallel measurements provide good stability and stability robustness over a wide speed range.

 PRECEDING PAGE BLANK NOT FILMED

ACKNOWLEDGMENT

This report was prepared by SatCon Technology Corporation under subcontract to the Charles Stark Draper Laboratory (CSDL) in support of Annular Momentum Control Devices (AMCD) under NASA contracts NAS9-16023 and NAS9-17560. The authors would like to thank Claude Keckler of NASA Langley and Ken Greene of CSDL, the technical monitors for this research for their guidance.

This report draws extensively on the master's theses of Tom Foley and Laura Larkin as well as the doctoral theses of the authors. The authors would like to acknowledge the help Tom and Laura have provided to both this research and this report.

PRECEDING PAGE BLANK NOT FILMED

PAGE IV INTENTIONALLY BLANK

TABLE OF CONTENTS

1 INTRODUCTION 1

1.1 Background 1
1.2 AMCD Combined Control Energy Storage Systems. . . . 3
1.3 Magnetic Bearing Control: State-of-the-Art 6
1.4 Research Focus. 9

2 COMPONENT MODELLING AND DESIGN 11

2.1 Large Angle Magnetic Suspension 11

2.1.1 Lorentz-Force LAMS 14
2.1.2 Magnetic Field Model and Test 17
2.1.3 Stator Coil Impedance Model and Test 23
2.1.4 Force/Current Model and Test. 25

2.2 Motor/Generator 25
2.3 Flywheel and Spoke Structure 33

3 SYSTEM DYNAMICS MODEL 38

3.1 Translational Open-Loop Model. 41
3.2 Angular Open-Loop Model. 47

4 STABILITY REQUIREMENTS. 55

5 CONTROLLER EXAMPLES. 57

5.1 Closed-Loop Translational Model 57
5.2 Closed-Loop Angular Model 61

6 CONCLUSIONS 66

BIBLIOGRAPHY 69

APPENDIX A. 73

APPENDIX B. 92

PRECEDING PAGE BLANK NOT FILMED

PAGE VI INTENTIONALLY BLANK

LIST OF TABLES

Table		Page
I	Characteristics of the Laboratory ACCESS Module.	5
II	Basic Dimensions for Lorentz-Force LAMS	15
III	Coil Characteristics	15
IV	PM-field Model Predictions.	18
V	Model Parameters	23
VI	Static Force/Current Gains	25
VII	Prototype Development Specifications	29
VIII	Motor/Generator Candidates	29
IX	Final Machine Candidates	30
X	Candidate Machine Side-Loading Forces	30
XI	ACCESS Inertia Values	34
XII	ACCESS Spoke Characteristics	37
XIII	Closed-loop Eigenvalues for the Translational Case.	57
XIV	Angular Closed-Loop Eigenvalues	65

PRECEDING PAGE BLANK NOT FILMED

PAGE VIII INTENTIONALLY BLANK

LIST OF FIGURES

Figure		Page
1	Laboratory-model ACCESS.	4
2	Attraction-force LAMS Design Options	12
3	Lorentz-force LAMS Design Option	13
4	Finished LAMS Rotor Parts	14
5	Machine-wound Stator Coil	16
6	Hand-wound Stator Coil	17
7	Lumped-parameter Magnetic Load Model	19
8	Lumped-parameter Magnetic Source Model	20
9	Permanent-magnet Field Model	21
10	Permanent-magnet Field Measurements	22
11	Stator-coil, Equivalent-circuit Model	23
12	Useful-air-gap Flux Density Measurements	24
13	Thrust Force Produced by a Centered LAMS Coil	26
14	Effect of Linear Motion of the Rotor	27
15	Effect of Angular Motion of the Rotor	28
16	Spherical Air-gap Ironless Stator/Rotating Back-iron PM Machine	31
17	Prototype Motor/Generator Rotor	32
18	Figure 2.16b Spherical Air-gap Ironless PM Rotor Sketch - Plan View	32
19	Prototype Motor/Generator Stator	33
20	Configuration Using 3 Cylinder Supports	35
21	Sample Arc-spoke	35
22	Best U-spring Spoke	36
23	Sample Dogleg Spoke	36
24	Optimized Dogleg Spoke	37
25	Block Diagram of a Magnetic Bearing System	38
26	Cut-away of a Torodial, Multi-body, Flexible Rotor System	39
27	Root-Locus as a Function of Rotational Speed, Open-Loop Translational Model	43
28	Eigenvalue Damping versus Rotational Speed	44
29	Bode Magnitude and Phase Plots of the Complex Coefficient Transfer Function for Positive and Negative Frequencies: Translational Model at a Sub-flexible Rotational Speed of 100 rad/sec.	45
30	Bode Magnitude and Phase Plots of the Complex Coefficient Transfer Function for Positive and Negative Frequencies: Translational Model at a Sub-flexible Rotational Speed of 1000 rad/sec	46
31	Root Locus versus Rotation Speed: Open-loop Angular Model	49
32	Eigenvalue Frequency and Damping	51
33	Bode Magnitude and Phase Plots of the Parallel Complex Coefficient Transfer Functions: Angular Model at Zero Rotational Speed	52

PRECEDING PAGE BLANK NOT FILMED

PAGE X INTENTIONALLY BLANK

34 Bode Magnitude and Phase Plots of the Complex Coefficient Transfer Function for Positive and Negative Frequencies: Open-loop Angular Model at a Sub-flexible Rotational Speed of 100 rad/sec 53
35 Bode Magnitude and Phase Plots of the Complex Coefficient Transfer Function for Positive and Negative Frequencies: Open-loop Angular Model at a Super-flexible Rotational Speed of 2000 rad/sec 54
36 Bode Plot of Translational MBC: Medium-bandwidth Controller with Low-frequency Loop Recovery, 1000 rad/sec Rotational Speed 58
37 Nyquist Plot of Translational MBC & Plant Loop Transfer Functions: Medium-bandwidth Controller with Low-frequency Loop Recovery, 1000 rad/sec Rotational Speed 59
38 Translational Closed-loop Pole Locations versus Rotational Speed: Medium-bandwidth MBC designed at a Rotational Speed of 1000 rad/sec 60
39 Bode Plot of the Lead-lag Compensator for the Angular model 62
40 Bode Plot of the Angular Loop Transfer Function: Lead-lag Compensator at a Rotational Speed of 200 rad/sec . . . 63
41 Angular Closed-loop Eigenvalues versus Rotational Speed: Lead-lag Compensator 64

A.1.1 Rotating Coordinate System 75
A.1.2 Relation of Rotating Coordinate System to Fixed Coordinate System: Relative Angular Orientation. . . 76
A.1.3 Relation of Rotating Coordinate System to Fixed Coordinate System: Relative Angular and Translational Orientation 78
A.1.4 Spinning Coordinate System 79

B.1.1 Linear Quadratic Regulator Loop Configuration. . . . 94
B.2.1 Model Based Compensator Loop Configuration. 97
B.2.2 Block Diagram of Model Based Compensator and Plant . . 98

1.0 INTRODUCTION

This document reports research into the modelling and control of an advanced Annular Momentum Control Device (AMCD), used to control the attitude of spacecraft. These systems consist of a angular momentum storage flywheel supported in magnetic bearings. This research was performed by SatCon Technology Corporation under subcontract to the Charles Stark Draper Laboratory (CSDL) in support of a specific AMCD, the AMCD Combined Control Energy Storage System (ACCESS) developed at CSDL. SatCon Technology Corporation was tasked to develop a dynamic model and stabilizing controller for the system.

The first chapter of this report provides background and introductory material. The next section, Section 1.1, provides background material for the combined energy storage and attitude control systems and the angular momentum control device. Section 1.2 introduces the specific system analyzed in this report, the AMCD Combined Control Energy Storage (ACCESS) System. Section 1.3 discusses the background in flexible rotor control that is applicable to the ACCESS system. Section 1.4 then discusses the specific problems that are addressed in this research.

Chapter 2 contains a brief discussion of the important subcomponents in the ACCESS system; the motor generator, the flywheel and spokes, and the large angle magnetic suspension. Chapter 3 combines these subcomponent models into a system model. The dynamics of the ACCESS system will be shown, under suitable assumptions, to decouple into separate translational (radial) and angular (tilt) models. The open-loop characteristics of the ACCESS model are then presented including the important open-loop instabilities that result from operation at speeds greater than the flexible mode frequencies of the suspended rotor.

Based on this system model, the controller requirements are presented in Chapter 4 along with the form of the linear, feedback controllers that are investigated. Chapter 5 presents some representative examples of these controllers for both the translational and angular models. Finally, Chapter 6 presents conclusions and recommendations for further work.

1.1 Background

The use of flywheels as attitude control actuators for orbiting spacecraft began in the early days of the space program [Roberson 1958] and has steadily progressed to a state of relative maturity [Weinberg 1982; Wertz 1978]. Reaction wheels, momentum wheels, and control moment gyros are the current approaches by which torques are applied to satellites. All of these devices effect attitude control by exchanging angular momentum between a flywheel and the spacecraft. Reaction and

momentum wheels contain variable-speed flywheel rotors with a fixed orientation relative to the spacecraft. Reaction wheels are designed to spin in either direction and are nominally non-spinning. Momentum wheels spin in only one direction about a nominal bias speed. A control moment gyro (CMG) contains a constant-speed flywheel with either a single- or a two-degree-of-freedom gimbal system. Angular momentum is exchanged between a CMG and a spacecraft through the variation of the relative orientation of the flywheel [Kennel 1970; Wertz 1978].

The primary cause of torque jitter in these devices is the mechanical bearings that are unable to precisely maintain the orientation of the angular momentum of the flywheel with respect to the satellite. This problem is typically solved by demanding extremely close manufacturing tolerances in the mechanical bearings [Wienberg 1982].

A magnetic bearing allows the angular momentum of a flywheel and its related dynamics to be controlled in a spacecraft environment. The earliest attempt at utilizing a magnetically suspended flywheel as an attitude control actuator was made at NASA/LaRC with the construction of an Annular Momentum Control Device (AMCD) that consists of a magnetically suspended graphite/epoxy hoop designed to be used as a momentum wheel [Anderson 1975; Groom 1978]. There has also been a great deal of research performed by Sperry Flight Systems [Sabnis 1975; 1976; Stocking 1984], the European Space Agency [Robinson 1984], and the Japanese National Aerospace Laboratory [Murakami 1982] aimed at developing magnetically suspended angular momentum exchange effectors.

The first study of a combined attitude control and energy storage system using flywheels was performed by Rockwell International for NASA in 1974 [Notti 1974]. This system, call an Integrated Power and Attitude Control System (IPACS), contained high-speed ball bearings and a permanent magnet motor/generator supporting and driving a titanium rotor. The study identified magnetic suspensions, composite rotors, and high-efficiency motor/generators as subsystems important for improved performance [Anderson 1973; Keckler 1974; Notti 1974].

These combined energy storage and attitude control systems have been investigated at CSDL since 1981 [Eisenhaure 1984a; 1984b], growing out of earlier work in magnetic bearings for terrestrial energy storage flywheels begun in 1975 [Eisenhaure 1977]. The first concept consisted of a pair of magnetically suspended, counter-rotating flywheels mounted along the roll axis of a small satellite. This system can provide adequate control torques when the energy and angular momentum wheels are gimballed through only small angles ($< 0.7°$) [Eisenhaure 1984a].

1.2 AMCD Combined Control Energy Storage System (ACCESS)

An advanced ACCESS effector evolved out of a study that considered the ACCESS concept for use in Space Station. This joint CSDL and Rockwell International study resulted in the design of an Attitude Control and Energy Storage System (ACESS) based on an advanced ACCESS effector [Oglevie 1985]. A unique feature of this advanced ACCESS design is the large-angle magnetic suspension (LAMS). This suspension allows limited gimballing freedom of approximately five degrees. This magnetic gimballing eliminates the need for mechanical gimbals.

A scale model of the advanced ACCESS module is being developed at CSDL to prove concept viability. This laboratory module is an approximately 1/20th scale model of an Space Station ACCESS module. The size of a full-scale module and scaling decisions can be found in [O'Dea 1985]. The laboratory module shown in figure 1 consists of a central, electromechanical hub connected to the flywheel by a spoke structure. The electromechanical hub contains the large-angle magnetic suspension, motor/generator, and sensors. The electromechanical hub also contains touchdown bearings in case of magnetic bearing failure. An auxillary lifting electromagnet is shown at the top of the figure. This magnet is needed to unload the weight of the suspended flywheel system from the large-angle magnetic suspension, which is not designed for earth gravity environment.

ORIGINAL PAGE IS
OF POOR QUALITY

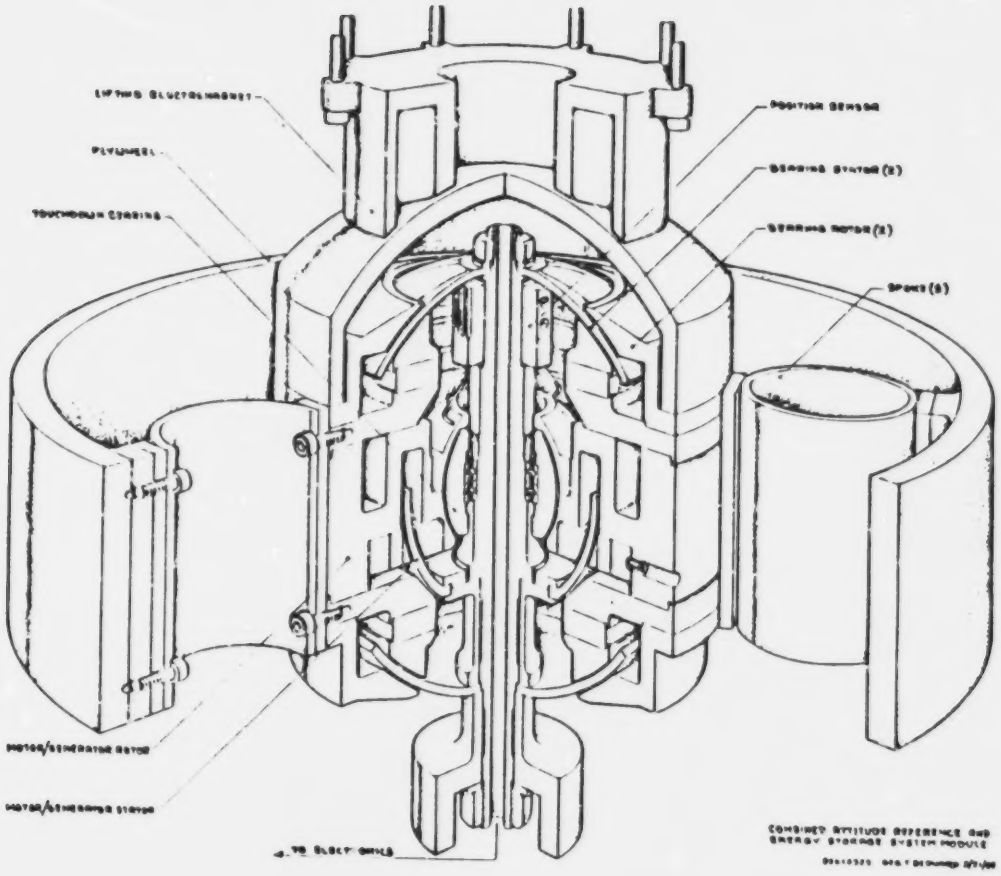

Figure 1. Laboratory-model AMCD Combined Control Energy Storage System (ACCESS)

The following paragraphs provide a brief description of the important ACCESS subsystems. The design size and capabilities of the laboratory module are given in Table I. The paper by O'Dea [1985] provides a more detailed overview of the system while Chapter 2 of this report provides more detailed descriptions of the designs of each subsystem.

Table I. CHARACTERISTICS OF THE LABORATORY ACCESS MODULE

Flywheel Mass (kg)	18
Flywheel Angular Momentum (kN-m-s)	2.2
Maximum Gimbal Angle (degrees)	± 5
Power (kW)	1
Maximum Control Torque (N-m)	5
Maximum Rotational Speed (rad/sec)	1690

The large-angle magnetic suspension chosen for the laboratory ACCESS module is a Lorentz-force, spherical air-gap bearing. The bearing uses Series 2-17 rare-earth-cobalt permanent magnets with a 22MGoe maximum energy product to produce a spherically radial magnetic field in the spherical air gap. The spherical configuration allows limited gimballing freedom in the bearing. The eight stator coils mounted in the spherical air-gap are capable of providing translational and axial forces and radial torques by appropriate excitation of the coils. This type of Lorentz-force bearing has the advantages of linearity, high bandwidth, and negligible coupling between bearing force and motion.

The motor/generator transfers power bidirectionally between the flywheel and electrical power bus. The motor/generator must have high efficiency in both motor and generator modes. Other requirements include low side loading on the magnetic suspension and gimballing capability. A variety of machine types were investigated from which a permanent magnet, ironless stator/rotating backiron machine was chosen. This design gives high efficiency and low side loads. The machine also features a spherical air-gap to allow limited gimballing.

The ACESS study concluded that a thin-wall annular flywheel made of Boron/epoxy was the most suitable for the advanced ACCESS module. For a composite flywheel, the method of torque transfer and support between the flywheel and hub is a critical area of

design. This spoke system must accommodate the high radial growth that will be seen with a composite flywheel. Because of time and cost constraints, the laboratory ACCESS flywheel is constructed of AISI 4340 steel rather than Boron/epoxy. The spoke system, however, was designed to meet the flexibility requirements imposed by a composite flywheel.

Due to the flexibility requirements of the spoke structure and the high rotational speed of the flywheel, the ACCESS system is required to run at a rotational speeds higher than the first natural frequency of the freely suspended rotor. SatCon Technology Corporation was tasked to understand the controller design issues and requirements posed by this super-flexible operation. The focus of this research is to address the control problems associated with the flexible nature of the ACCESS rotor system and not to address directly the control issues associated with using the ACCESS modules to control energy storage and attitude of a spacecraft.

Before beginning a more detailed discussion of the modelling and control of the ACCESS system in Chapter 2, the next section briefly reviews previous research into active control of magnetic bearing systems.

1.3 Magnetic Bearing Control: State-of-the-Art

Magnetic bearings are a technology still undergoing rapid development. Products that include magnetic bearings are now available, however, and some types of magnetic bearings have become relatively common. Mature magnetic bearing technology is exemplified by systems comprised of biased ferromagnetic, attractive bearings with inductive position sensors feeding single-loop designed controllers. The bearings maybe permanent magnet biased or electromagnet biased. The controllers are usually implemented with analog electronics. The rotating structure is modelled as a rigid body and the magnetic bearings are made to behave dynamically as conventional spring/damper bearings by the use of "local" feedback.

During the last ten years a handful of researchers have begun investigating the use of magnetic bearings to support and control flexible rotors, which are rotors running at rotational speeds higher than their lowest frequency of free vibration. Schweitzer was the first to publish research about the active control of flexible rotors [Schweitzer 1974]. The system he investigated consisted of a three rotor masses connected by well damped, flexible segments. The multi-mass rotor was supported by conventional bearings with an actively controlled magnetic bearing added for use as an active damper. This early work used state-space methods to place closed loop system poles. Another thrust of their research was optimal placement of the sensors and active damper using generalized stabilizability and observability

criteria over the modes for which active control is desired. Using the active damper, Schweitzer, et. al. were able to approximately double the range of stable operation, where the destabilizing mechanism was the rotor internal damping. They also showed improved synchronous response to mass unbalance with the active damper.

In later work they found that non-colocation of the sensors and actuator as placed by optimal stabilizability and observability criteria can lead to spillover effects, including instability [Salm 1984]. They designed reduced order controllers to that provided robust, stable control when combined with collocated sensor/actuators. The design of these integrated sensor/actuator sub-systems is discussed in [Ulbrich 1984]. The development of integrated sensor/actuators has led to interest in localized control of the actuator based only on information available from the integrated (collocated) sensor. This decentralized control problem is addressed by [Bleuler 1984] for rigid-body rotors. His thesis also reports the use of a scheduled gain controller with two gains schedules, one used at low speeds and the other at high speeds. These scheduled gain controllers are needed because of the variation in plant dynamics caused by the gyroscopic effects that vary with rotational speed.

Linear-quadratic design methods were used in a study by [Hubbard 1980] and [McDonald 1985]. They considered a pendulously supported flywheel system where the magnetic bearing was assumed to apply both forces and torques. Their model included the effect of quill-shaft flexibility, but neglected shaft damping.

The works mentioned above used numerical techniques to design specific controllers while [Johnson 1985a; 1985b] examined the range of behavior that is possible given a specific controller structure. His work analytically examined the lateral dynamics of a flexible rotor supported by active bearings. The rotor system consisted of a single mass rotor with mass unbalance mounted on a symmetrical shaft (Jeffcott rotor) with internal damping. The active bearings were assumed to be ideal actuators driven by fixed-gain or variable-gain, linear controllers. Measurements of the position and velocity of the shaft-rotor at the rotor and at the shaft ends (bearings) were the controller inputs. The goal was a qualitative and quantitative understanding of the differences between rotor and bearing feedback.

An interesting flexible rotor, which utilizes the unique capabilities of magnetic bearings, is the Annular Momentum Control Device (AMCD) [Anderson 1979]. This device consists of a rotating annular rim suspended by noncontacting magnetic bearings mounted along its periphery. The magnetic bearings interact with a low-loss ferrite material, embedded in the graphite-epoxy rim,

producing radial and axial suspension forces. The five-degree-of-freedom control problem associated with this system was found to be challenging [Groom 1981, p130]. The early approaches used single-input, single-output (SISO) control theory, which was found to be inadequate. Later approaches considered the system as a multi-input, multi-output, flexible system and used digital control with table look-up linearization of the magnetic bearing force laws [Groom 1984, p297; Groom 1981].

A number of authors have investigated the use of magnetic bearings in conjunction with conventional oil-film bearings to control instabilities in flexible shaft systems. The dominant instability mechanism in these cases is not shaft internal damping, but oil-film bearing instabilities. The use of magnetic bearings to add damping to a conventionally supported, flexible, marine power transmission shaft was investigated by Holms and coworkers [Nikolajsen 1979]. They found that increased stable operating speeds were possible with the use of the active dampers and that synchronous vibration was also reduced. They included magnetic flux feedback to reduce the destabilizing force-gap interaction of their actuators. In related work, they determined the optimum force versus frequency of an actuator used to stabilize these oil-film supported shafts [Kaya 1984].

Eigenstructure assignment was used in a study by [Stanway 1984] and O'Reilly. They considered a system consisting of a flexible, multi-mass rotor supported in conventional, flexibly mounted, oil-film bearings. The housings of the oil-film bearings were assumed to be controlled by active forces, supplied in addition to the forces generated by the flexible mounting structure. Damping in the rotor shaft and bearing support structure was neglected. They showed that this system can be controlled through forces applied to the bearing housing and that rotor position and velocity feedback gains are small compared to bearing position and velocity feedback gains.

In summary, the last decade has seen substantial advancement of the state-of-the-art in actively controlled, flexible rotors. This research field, which started during the late 1960's and early 1970's, now draws the attention of a handful of researchers. Early research viewed the magnetic bearings as a source of additional external damping applied to conventionally supported, flexible rotors. The emphasis in this early work was the placement of the actuators (magnetic bearings) and sensors. Also, during this early period state space models of the flexible rotor systems that included shaft damping were developed. The development of these state space models allowed the tools of modern, state-space based control techniques to be applied to controller design, which is particularly important because of the multi-input, multi-output characteristic of magnetic bearing/rotor systems. Examples of state-space based controller

designs include eigenvalue and eigenstructure assignment and linear-quadratic optimal regulators.

1.4 Research Focus

The research reported in this document can be divided into two areas, modelling and control design. The modelling effort consists of modelling the separate subcomponents of the ACCESS system and combining these component models into a system model useful for controller design. These subcomponent models for the large angle magnetic suspension, flywheel and attachment, and motor/generator are contained in Chapter 2. The system model based on these subcomponent model is presented in Chapter 3.

The emphasis in the development of the system model is to model, in a form suitable for controller analysis and design, the unique features of actively controlled rotor systems. The most important of these features is that the measurements of rotor position and orientation need not be colocated with actuation. Restated, the bearings (actuators) and measurement system (sensors) are not necessarily interacting with the same part of the rotor. In conventionally supported rotors, in contrast, the force produced at each bearing is a function of the time history of the position of the rotor at that bearing.

The second area of investigation is controller design and analysis for the ACCESS system. A variety of controllers have been designed, based on design methods ranging from "common sense" control engineering to model based compensators using linear-quadratic regulator and Kalman filtering algorithms. The behavior of the controlled system to the two main problems of rotor dynamics, non-synchronous stability and synchronous response, are investigated. In building on the existing research in the field, three main areas are emphasized. These are:

1) the effect of plant variation with speed and

2) the controller requirements, especially those imposed by the unstable nature of flexible rotor systems.

Both gyroscopic and internal damping effects cause the plant to change with rotational speed. Gyroscopic effects cause the frequencies of some of the plant open-loop eigenvalues to become strong functions of rotational speed. Internal damping causes the damping of some of the plant open-loop eigenvalues to become strong functions of rotational speed. Because of internal damping, some modes will show increased damping with increased rotational speed while others will become less damped, becoming open-loop unstable at high rotational speeds. The development of controllers for this speed variable plant is one goal of this research.

Another goal is to investigate the controller/estimator requirements of actively controlled flexible rotor systems. In particular, what are the bandwidth requirements and what controller/estimator complexity is required to stabilize a high-speed, unstable, flexible rotor?

2. COMPONENT MODELLING AND DESIGN

This chapter contains a brief discussion of the designs and models for the large angle magnetic suspension, the flywheel and attachment, and the motor/generator. More extensive presentations can be found in the referenced theses.

2.1 Large Angle Magnetic Suspension

Several magnetically-gimballed flywheel designs have been reported in the United States [Anderson 1975; Eisenhaure 1984a], West Germany [Sindlinger 1976; 1977], and Japan [Murakami 1982]. These flywheels were designed to be used in active stabilization of the attitude of small satellites. Gimbal angles up to about 2° have been reported. Among these designs, several employ thin-walled, large-diameter flywheels [Anderson 1975; Sindlinger 1977; Teldix 1978]. One such design is the Annular Momentum Control Device (AMCD) [Anderson 1975]. These devices demonstrate the design freedom that results from employing magnetic bearings [Hendrickson 1974]. The AMCD, for example, is a thin hoop that is nearly six feet in diameter. Supporting this rotor by more conventional means would be difficult, if not impossible. Since that time, several alternative approaches to magnetically supporting and gimballing large, thin annuli have been developed [Groom 1981; Sindlinger 1977; Teldix 1978]. In the first of these references, Groom describes an upgraded magnetic bearing and microprocessor-based controller for the AMCD. In the second of these references, Sindlinger describes two magnetic bearing designs. The first of these is an axially-passive, attraction-force design which he refers to as "electromagnetic". The second is a Lorentz-force approach which he refers to as "electrodynamic". Both of the design approaches which were discussed by Sindlinger are featured in the third reference which is a manufacturer's catalog of momentum exchange effectors.

For many proposed large spacecraft, however, the limited gimbal angle capability of conventional magnetic bearings is not adequate. This has led to the design and investigation of "large angle magnetic suspensions" (LAMS) that allow gimballing of up to 15°. The LAMS actuator applies forces and torques in response to measurements of three translational and two angular positions of the flywheel in order to regulate the translational position (center the flywheel) and servo-control the angular position (gimbal the flywheel).

As with conventional magnetic bearings, LAMS forces may be exerted through ferromagnetic-attraction or Lorentz forces. The LAMS system operates in an all-axes-actively-controlled mode since gimballing is required. Three LAMS design options (two attraction-force and one Lorentz-force) have been developed and analyzed [Downer 1986]. The two ferromagnetic attraction

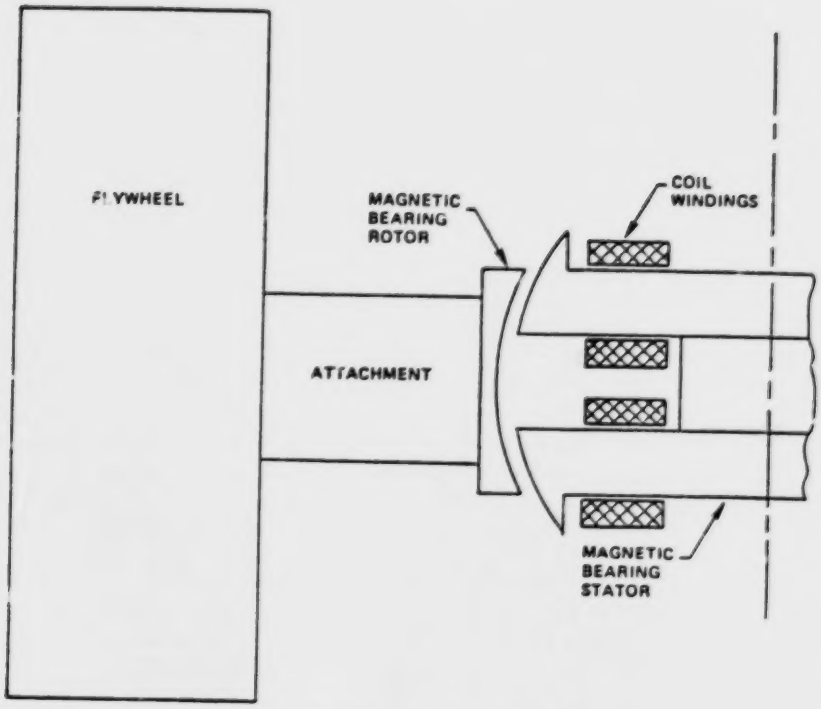

a) Heteropolar Design

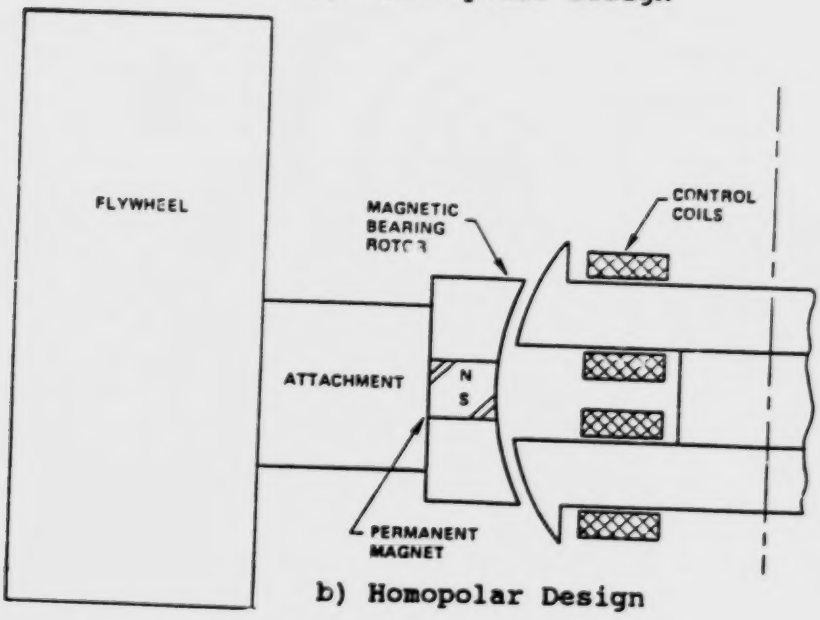

b) Homopolar Design

Figure 2. Attraction-force LAMS Design Options

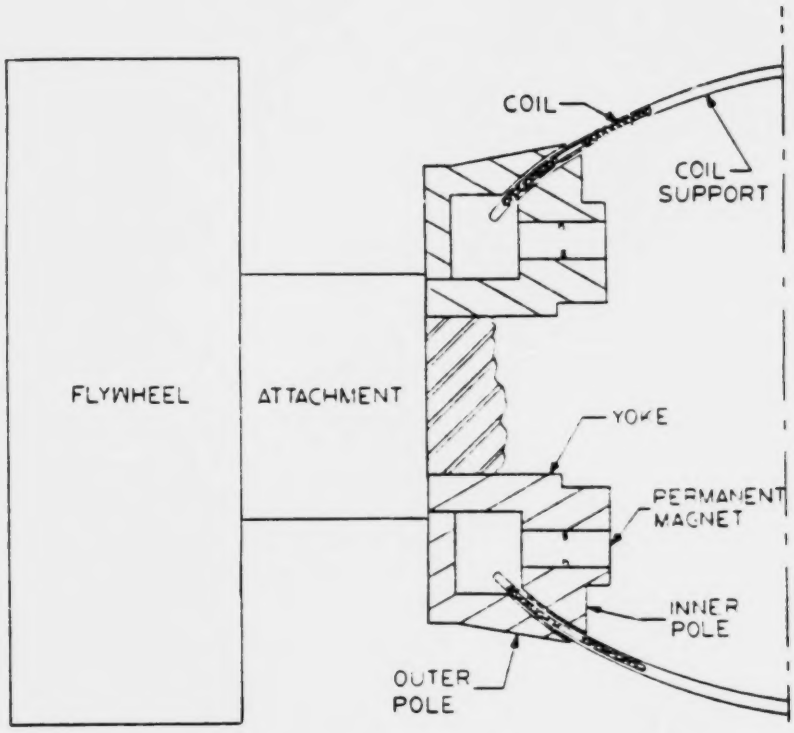

a) Section View

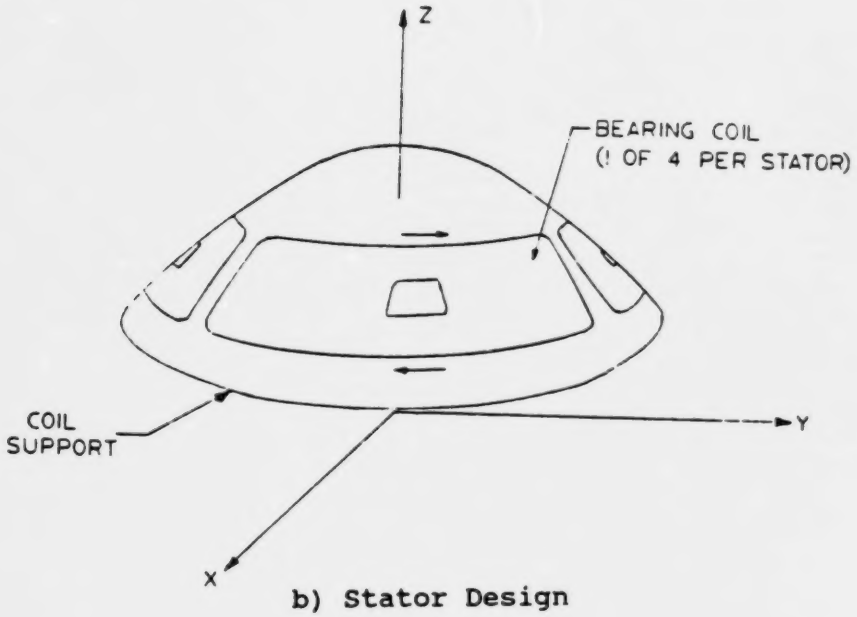

b) Stator Design

Figure 3. Lorentz-force LAMS Design Option

LAMS are shown in figure 2. The Lorentz force design is shown in figure 3.

2.1.1 Lorentz-Force LAMS

After a comparative study [Downer 1986], the Lorentz-force LAMS was chosen for the laboratory ACCESS module. The Lorentz-force LAMS (figure 3) consists of two identical actuators each containing a rotor and a stator. Each rotor contains an axially-oriented, permanent magnet and sufficient core material to yield an approximately spherically-radial magnetic field in the air gap. Each stator consists of a thin shell containing four control coils as is shown in figure 3b.

The PM-field, Lorentz-force LAMS is similar to a conventional Lorentz bearing or actuator, such as a speaker coil. By appropriately exciting the coils, axial forces, radial forces, and radial torques are produce. All five control channels have linear force/excitation characteristics. No steady excitation is required to maintain the magnetic field. A fixed-air-gap-length magnetic circuit is used to reduce core losses to those caused by the magnetic fields produced by the stator coils.

Figure 4. Finished LAMS Rotor Parts

The basic dimensions of the prototype LAMS are given in Table II. The finished rotor parts are shown in figure 4. The intermediate assembly (called the inner assembly) at the left of the photograph is made up of the inner pole, permanent magnet, and yoke. The permanent magnet is magnetized within this assembly. The rotor parts are fabricated from AISI 1018 carbon steel and a relatively inexpensive RE_2TM_{17} permanent magnetic material.

ORIGINAL PAGE IS
OF POOR QUALITY

Table II. BASIC DIMENSIONS FOR LORENTZ-FORCE LAMS

Nominal Spherical Radius	9.52 cm	3.750 in
Air-Gap Length	0.51 cm	0.200 in

The prototype LAMS stator was designed with a machined aluminum coil support. Two methods of coil fabrication were investigated. The baseline approach is shown in figure 5. Individual coil segments are machine wound using a series of winding fixtures. Two of the fixtures are shown in figure 5b (one disassembled and one assembled). The round steel washers and tetrahedral arbors are used to ensure the thickness of the coil. After winding, the flat coils are hand formed to the final shape.

Figure 6 shows an alternate approach to coil fabrication. Wire is hand-wound onto a spherical fixture which approximates the shape of the coil support. Although the coil shown in the figure appears to be inefficient in terms of filling the available space, slightly more (≈7%) turns were obtained using this technique. The shape of the hand-wound coils is somewhat better than that of the machine-wound coils.

Table III compares the construction and resistance of the two types of coil. Design estimates of the resistance of the coil are also provided (in parentheses). The discrepancy in the estimated and actual resistances for the hand-wound coil indicate that the fill factor is only about 81% of a perfect wire arrangement (≈64%). Although more turns were obtained for the hand-wound coil (reduced power at the expense of increased voltage), the finished pieces were unusable because of several "high spots" which would have interfered with the spin of the rotor. The amount of manual labor that is required to hand wind a coil also produces a process that is quite expensive. Machine-wound coils were the baseline for the ACCESS system.

Table III. COIL CHARACTERISTICS

	Turns	Wire Size (AWG)	Resistance (Ω)
Machine-Wound	750	31	49
Hand-Wound	800	31	61

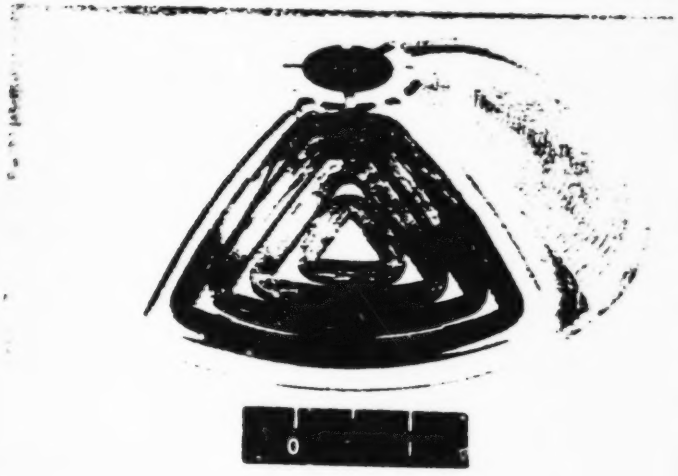

a) Finished Coil

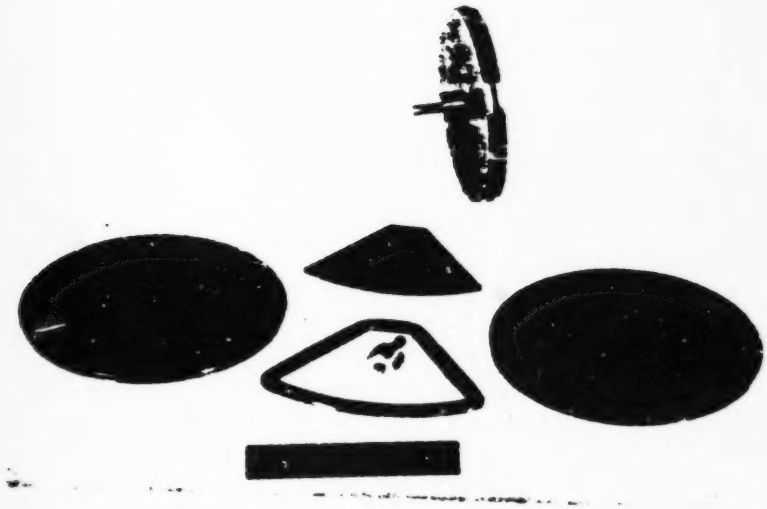

b) Fixturing

Figure 5. Machine-wound Stator Coil

ORIGINAL PAGE IS
OF POOR QUALITY

ORIGINAL PAGE IS
OF POOR QUALITY

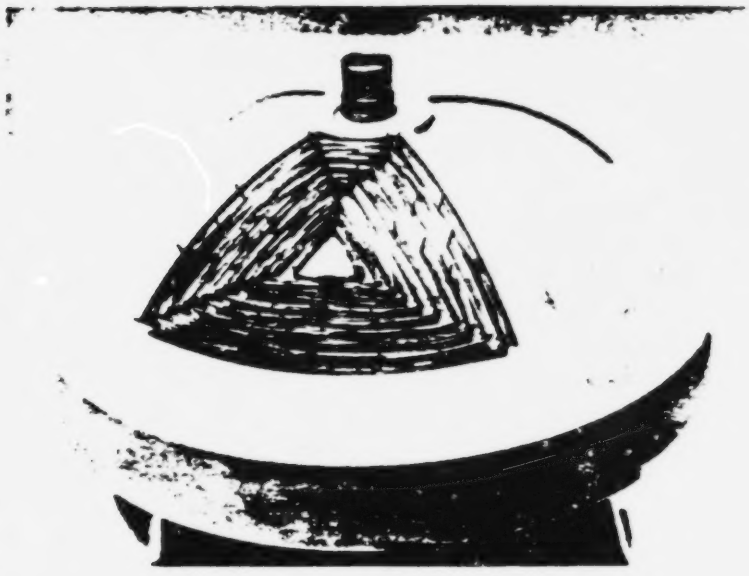

Figure 6. Hand-wound Stator Coil

2.1.2 Magnetic Field Model and Test

A series of tests on the LAMS were performed and compared with the predictions of models using lumped-parameter, methods to find the magnetic fields produced by the permanent magnet. A semi-analytical method [Rotors 1941; Downer 1986] is employed in order to create a network of lumped elements which approximates the actual field (magnetic load) and PM (magnetic source). figure 7a shows the flux paths that were used to approximate the magnetic field in the air space near the LAMS rotor. A network representation for this field is shown in figure 7b. The lumped permeances (shown in figure 7b) are related to the permeances of the flux paths (shown in figure 7a) as follows. The useful permeance P_u is that of the useful air gap (path u). The fringing permeance (P_f) is the sum of the permeances of the fringing flux paths (paths f1, f2, f3, and f4).

$$P_f = P_{f1} + P_{f2} + P_{f3} + P_{f4}$$

The leakage permeance (P_L) is the sum of the permeances of the leakage flux paths (paths L1, L2, L3, and L4)

$$P_L = P_{L1} + P_{L2} + P_{L3} + P_{L4}$$

The self-demagnetizing permeance (P_S) is the sum of the

permeances of the self-demagnetizing flux paths of the permanent magnet (paths S1 and S2)

$$P_S = P_{S1} + P_{S2}$$

The permanent magnet is represented by the Thevenin equivalent circuit shown in figure 8. The ideal potential source (F_m) and permeance (P_m) are functions of the permanent magnet operating point as shown in figure 8a [Downer 1986 p236].

The field and permanent magnet models are combined in figure 9. The load flux and its components are calculated from elementary network theory and are tabulated in Table IV.

TABLE IV. PM-FIELD MODEL PREDICTIONS

Useful Flux	4.08 mWb
Fringing Flux	0.90 mWb
Leakage Flux	0.91 mWb
Self-demagnetizing Flux	0.35 mWb
Load Flux	6.24 mWb
Useful-air-gap Flux Density	4.5 kG

In order to verify the predictions of this analytical model, a series of flux density measurements (using a Hall effect probe) were taken at the radial center of the air gap of the rotor. The elevational angle of the flux probe (see figure 10a) was varied in order to show the flux density profile, at the radial center (Ro) of the air gap, within the active region. Figure 10a describes the variable that was used to define position within the air gap. Figure 10b compares the predictions of the lumped-parameter model with flux density measurements. The useful-air-gap field (B_u) predicted by this analysis is reasonably close to the measurements except that the fringing paths (f1 and f2) adjacent to the useful air gap appear to be larger than predicted (note the rounding of the flux density profile). The prediction of the model and the mean flux density in the useful air gap are within 6% of each other.

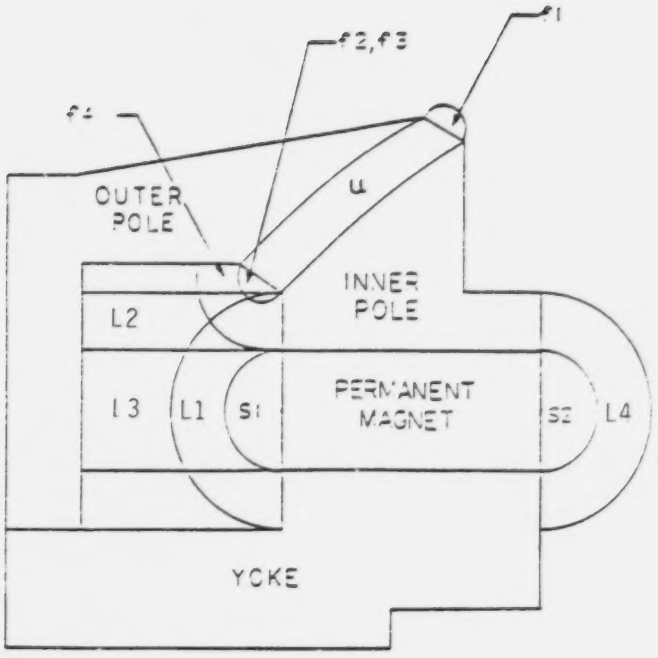

a) Flux-path Approximation of a Magnetic Field

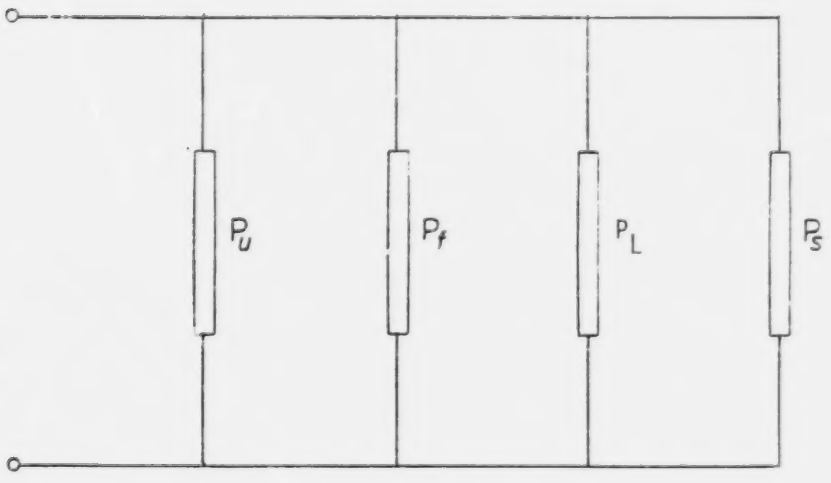

b) Network Representation

Figure 7. Lumped-parameter Magnetic Load Model

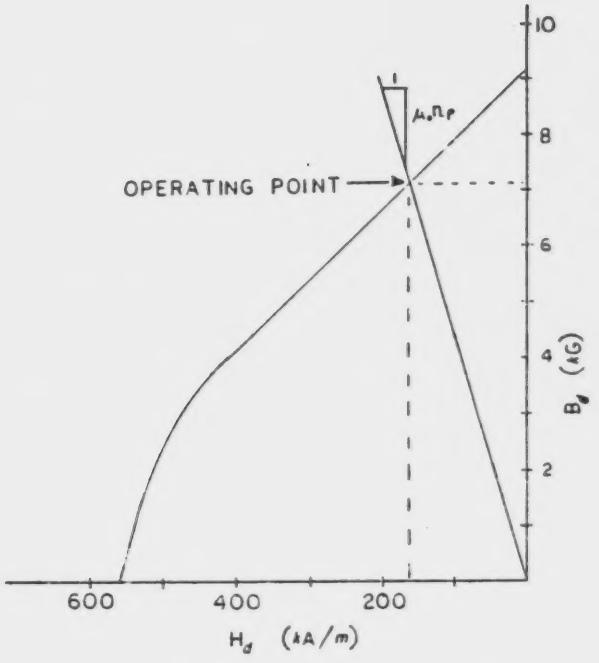

a) Operating Point of the PM

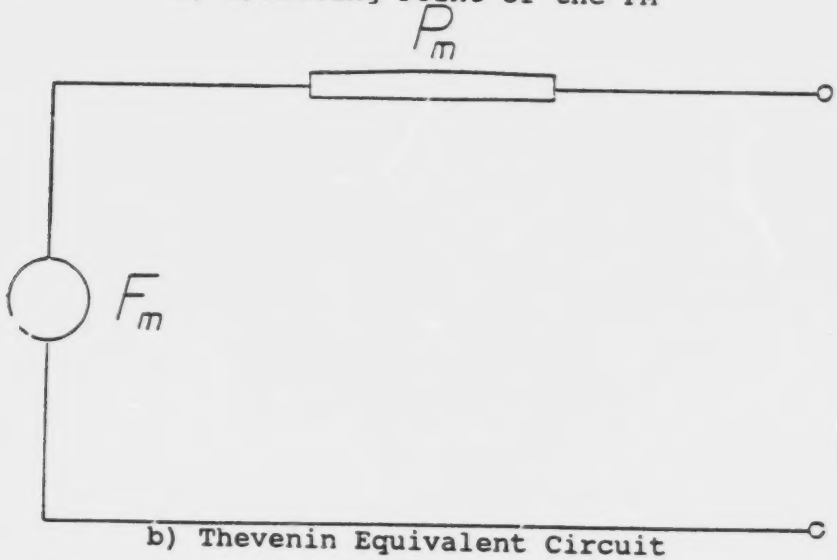

b) Thevenin Equivalent Circuit

Figure 8. Lumped-parameter Magnetic Source Model

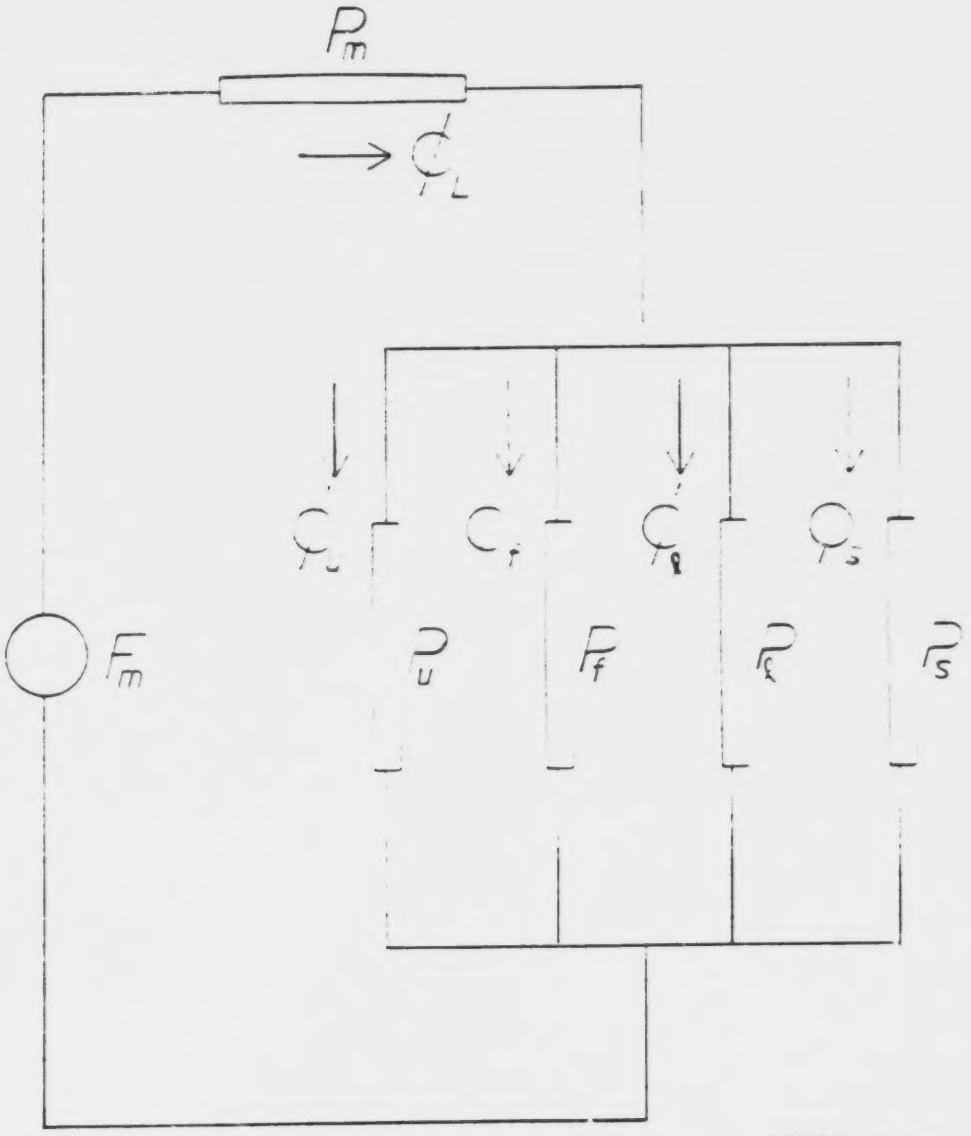

ORIGINAL PAGE IS
OF POOR QUALITY

Figure 9. Permanent-magnet Field Model

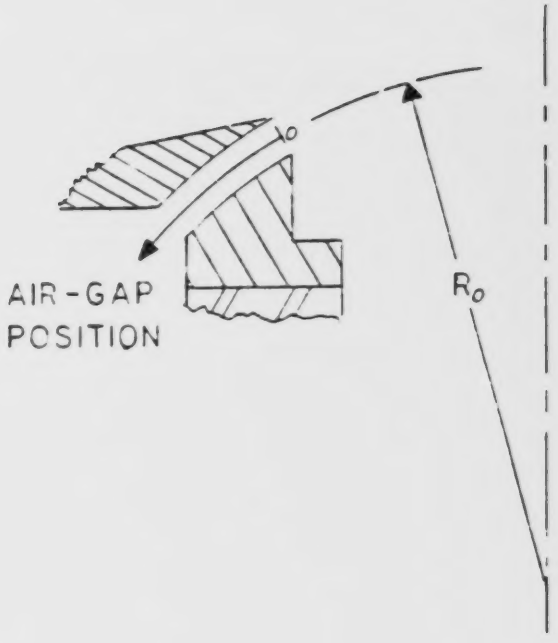

a) Air-gap-position Variable

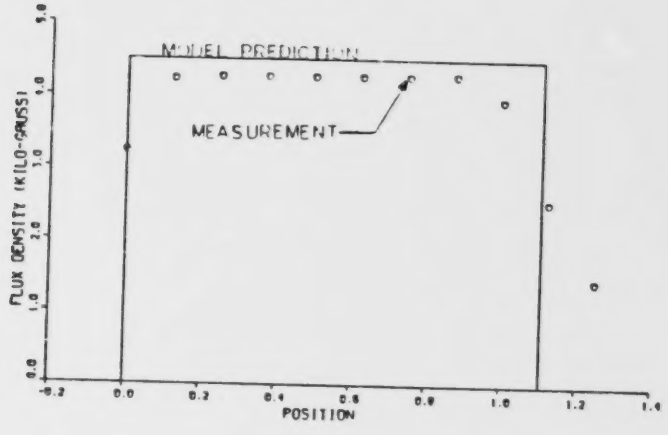

b) Model Prediction and Measurements

Figure 10. Permanent-magnet Field Measurements

2.1.3 Stator Coil Impedance Model and Test

A third order model of the stator coil impedance was developed that considers both conservative (magnetic fields) and dissipative (core losses in the rotor and eddy-current losses in the coil support) factors [Downer 1986, p237]. Figure 11 is an equivalent electrical circuit which describes the model. The series-connected resistor and inductor (r_{dc} and l_{ca}) account for the dc resistance of the coil and that portion of the magnetic field which does not link any lossy material. Eddy-current losses within the coil are not considered. The two sets of shunt-connected resistors and inductors (r_{cs}, l_{cs} and r_r, l_r) model the losses and magnetic fields in the coil support and rotor respectively.

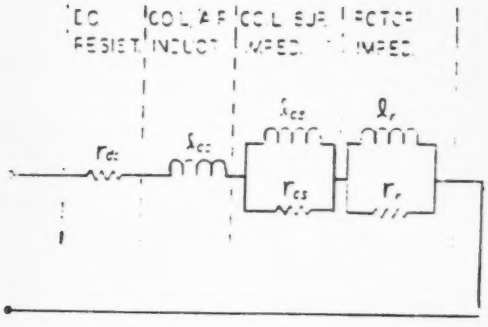

Figure 11. Stator-coil, Equivalent-circuit Model

In conjunction with the stator model, measurements of the actual ACCESS stator were performed. The parameters used in the model were determined empirically and are given in Table V below. The comparison of measurement and model is shown in figure 12, a plot of stator coil impedance magnitude versus excitation frequency. As can be seen from this figure, adequate agreement between the model (using empirically determined parameter values) and the measured data was obtained.

TABLE V. MODEL PARAMETERS

	RESISTANCE (Ω)	INDUCTANCE (mH)
dc	49.	--
coil/air	--	4.
coil support	65.	15.
rotor	30.	50.

ORIGINAL PAGE IS
OE POOR QUALITY

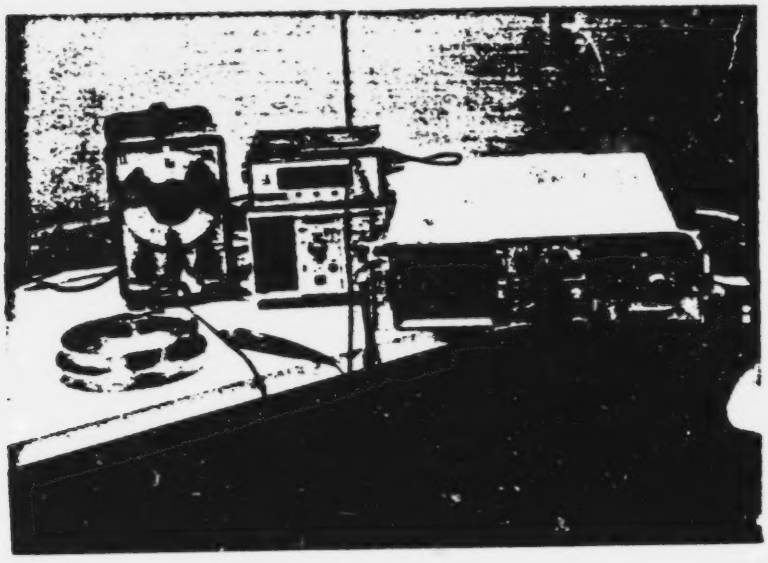

a) Test Fixturing

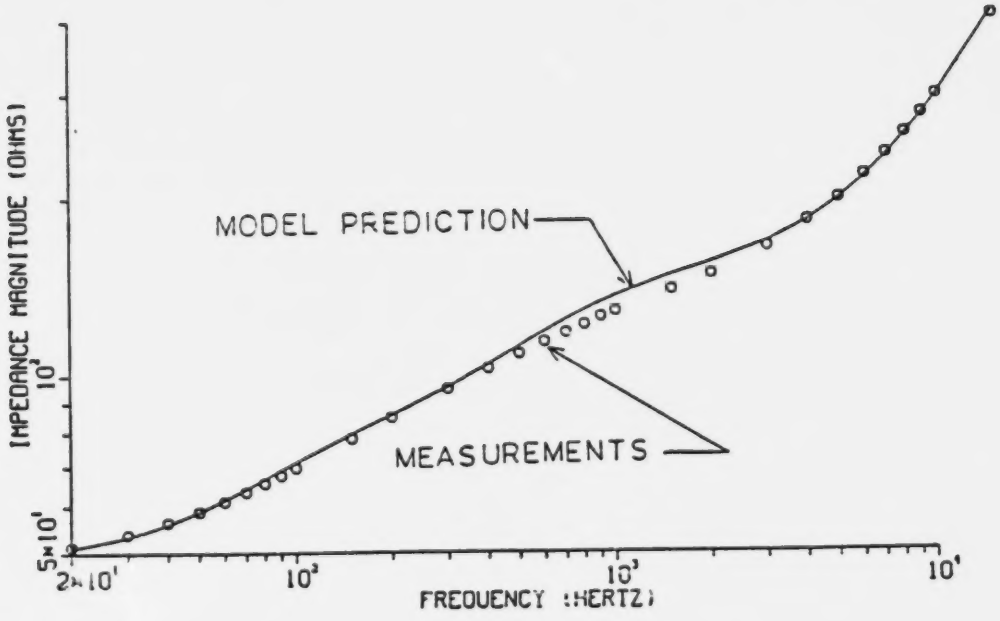

b) Test Results

Figure 12. Useful-air-gap Flux Density Measurements

2.1.4 Force/Current Model and Test

A model relating bearing force to coil current was developed by combining the magnetic field model, the stator coil model, and geometric considerations [Downer 1986, p243]. From this model, the gain constants relating bearing force or torque to coil current were found and are presented in Table VI.

TABLE VI. STATIC FORCE/CURRENT GAINS

Radial force constant	9.95 N/A
Axial force constant	8.82 N/A
Radial torque constant	1.27 Nm/A

In conjunction with this model development, the static, axial thrust of the LAMS was measured through the use of a tension-test machine. The stator of the LAMS was attached to the load cell and one coil was excited with constant current while the rotor was attached to the base via a three-degree-of-freedom test fixture. This three-degree-of-freedom test fixture allows the stator coils to be moved relative to the rotor along the radial and axial directions and rotated along a radial axis.

The results of the axial force test with the coil centered in the air gap are compared to the model in figure 13. The data show that the actual gain is about 7% lower than predicted. Figure 14 shows the effect on axial force of translational motion of the stator relative to the rotor. Figure 14a shows the effect on axial force of motion along the radial axis on which the coil is mounted. No variation in force was found for motion along the perpendicular radial axis. Figure 14b shows the effect of axial motion on the axial force. Figures 15a and 15b show the variation in thrust force with the relative angular position of the rotor. Angular motion about the axis perpendicular to the axis on which the coil is located has the greatest effect on the force. This is caused by the coil moving into or out of the useful air gap thereby increasing or decreasing the size of the active region.

2.2 Motor/Generator

A flywheel energy storage system requires a very high efficiency motor/generator to transfer energy bidirectionally between the spinning flywheel and the electrical bus. This machine must operate as both a motor and generator over the anticipated 2:1 speed range of the flywheel. For lightweight and relatively small spacecraft, weight and volume of system components are critical factors. This design goal demands a high-efficiency motor/generator. The specifications for the prototype ACCESS module are shown in Table VII.

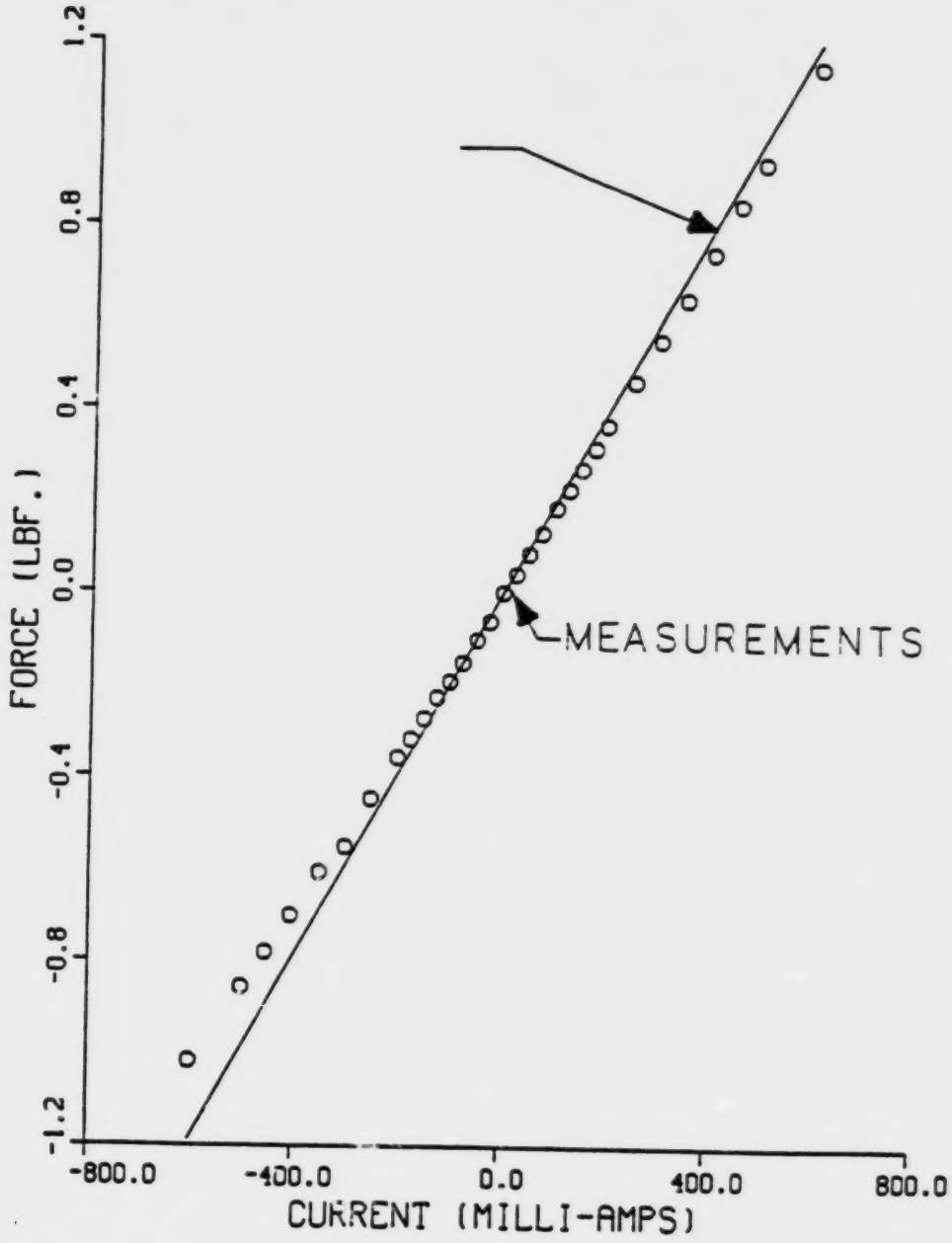

Figure 13. Thrust Force Produced by a Centered LAMS Coil

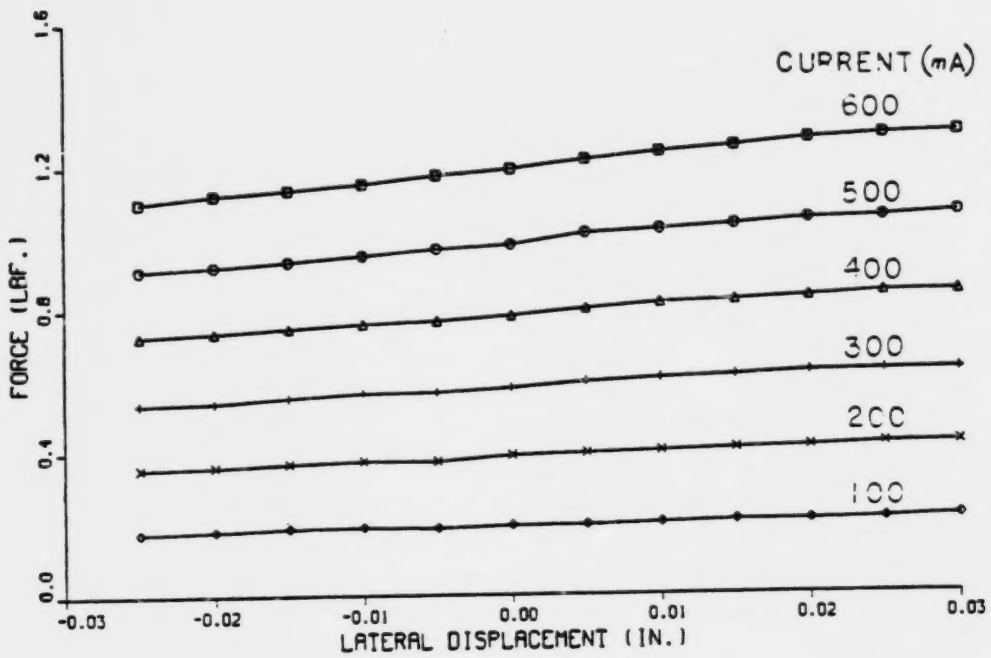

a) Lateral Motion

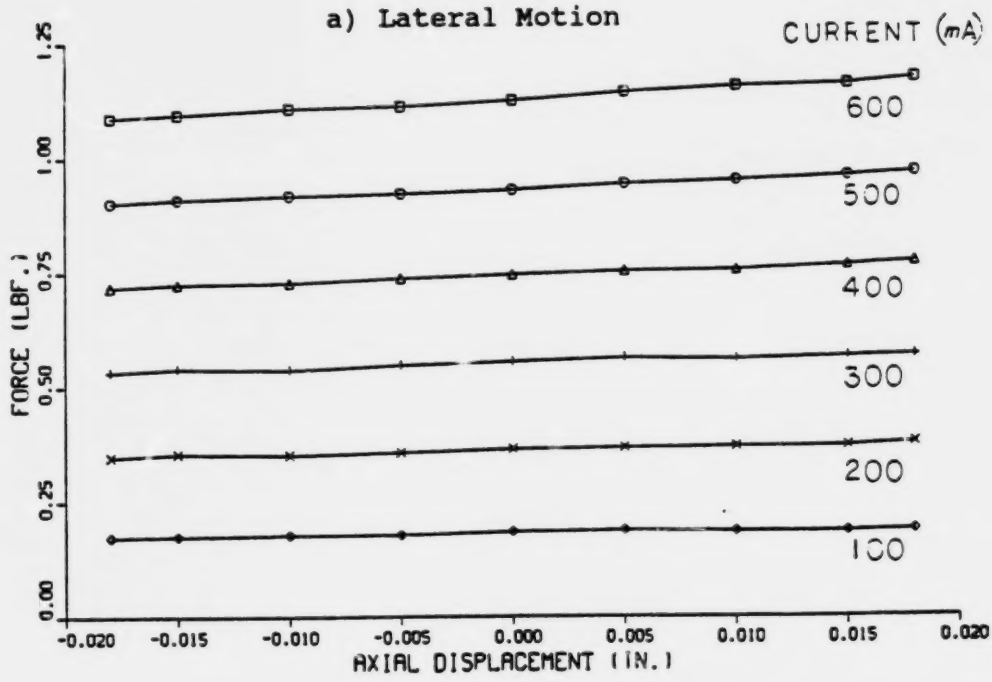

b) Axial Motion

Figure 14. Effect of Linear Motion of the Rotor

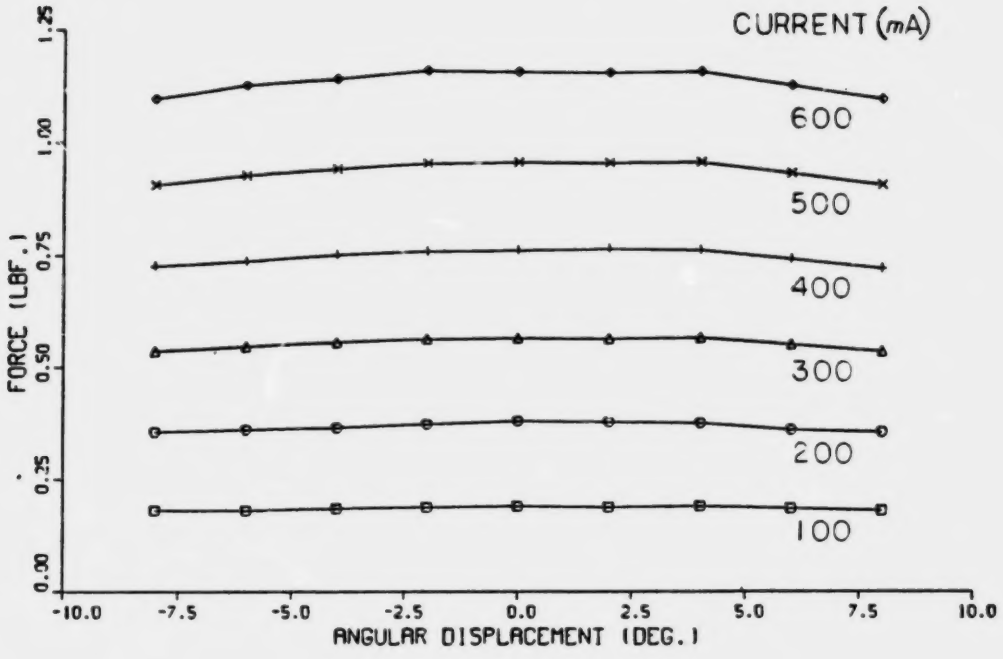

a) About the Axis of the Coil

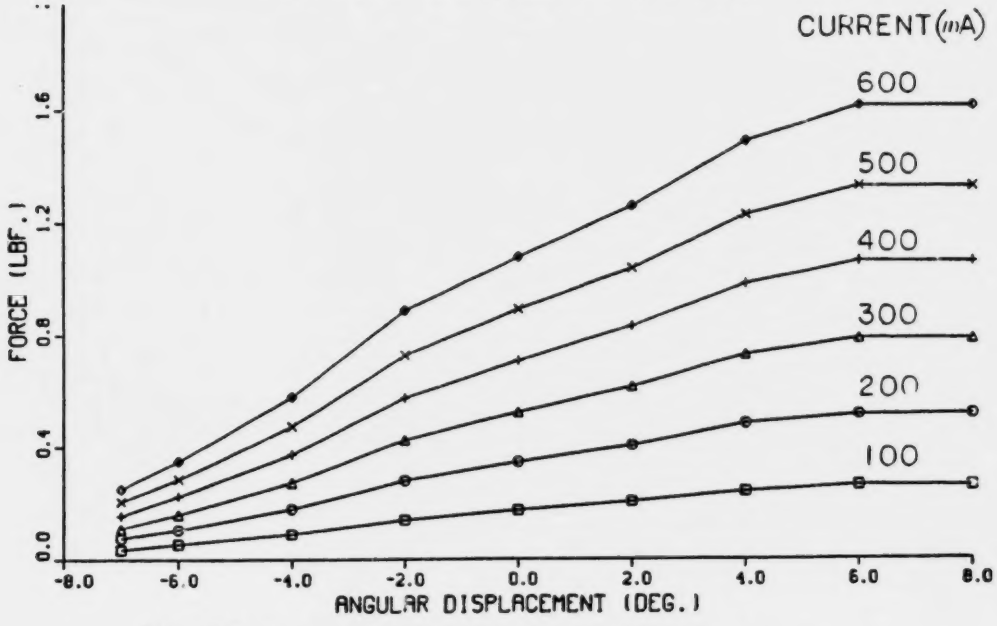

b) About an Axis Perpendicular to the Coil

Figure 15. Effect of Angular Motion of the Rotor

TABLE VII. PROTOTYPE DEVELOPMENT SPECIFICATIONS

Generator Output	1 kW
Operational Speed Range	10/20 krpm
Bus Voltage	200 Vdc

The primary considerations in the choice of machine type were copper loss, iron loss, and side-loading forces (acting to pull the rotor towards the stator) which would effect the dynamics of the magnetic suspension. Of secondary concern were level of integration with other system components and machine complexity.

Based on a literature search, five candidate machines were evaluated. These machines, along with a qualitative list of their attributes, are presented in Table VIII. These original five candidates were narrowed to the three presented in Table IX [Larkin 1985, p20]. This table includes qualitative information on machine losses, side-loading forces, and complexity in fabrication. R_{sta} is the resistance of the stator windings and R_{rot} is the resistance of the rotor windings.

TABLE VIII. MOTOR/GENERATOR CANDIDATES

Type	Advantages	Disadvantages
PM Reluctance	No field windings. PM's are stationary.	Potential large side forces. Voltage is a function of speed only.
Wound-field Synchronous	Can control voltage by changing field strength.	Power used to generate field is lost. Rotor and stator copper loss. Side forces.
Induction	Has simple, rugged design	Inherent rotor losses. Hard to remove heat from rotor. Large side forces. Rotor and stator copper loss.
Conventional Synchronous PM	No field windings.	Magnets typically rotate; potential large side forces. Voltage is a function of speed only.
Ironless/ Rotating Back-iron	Minimizes hysteresis and eddy current losses. Low side force. Readily available high energy product magnets.	More complex mechanically. Voltage is a function of speed only. Expensive magnets.

TABLE IX. FINAL MACHINE CANDIDATES

	PM SYNCHRONOUS	PM "IRONLESS"	INDUCTION
LOSS — IRON	MED	VERY LOW	LOW
LOSS — COPPER	I^2R_{sta}	I^2R_{sta}	$I^2(R_{sta} + R_{rot})$
SIDE-LOAD	YES	NEGLIGIBLE	YES
COMPLEXITY	MED	HIGH	LOW

Machine choices were further reduced by calculating [Larkin 1985, p22] the side-force negative spring constant for each machine. This is the force which acts to pull the rotor toward the stator and is therefore an unstable rotor force and must be counteracted by the magnetic bearing. The results of this analysis using parameters from existing machines and assuming a 1000 pound flywheel are shown in Table X. An unstable "frequency" (exponential rate of growth) of 150 rad/sec is sufficiently high to rule out the induction machine since it would place bandwidth restriction on the magnetic suspension which is much greater than that dictated by momentum control considerations [Oglevie 1985]. While techniques exist to inherently stabilize the side-force of an induction machine, they have been shown to require operation in the high-slip region, which is the low efficiency region of operation [Basore 1982].

TABLE X. CANDIDATE MACHINE SIDE-LOADING FORCES

	SPRING CONSTANT	NATURAL FREQUENCY (m = 455 kg)
INDUCTION MACHINE	11×10^6 N/m	154 rad/s
PM "IRONLESS"	NEGLIGIBLE	< 0.1 rad/s
CONVENTIONAL PM	285×10^3 N/m	25 rad/s

The ironless stator/rotating back-iron permanent magnet machine has comparatively lower losses and a lower spring constant than a more conventional permanent magnet motor/generator, making it the most efficient alternative for a satellite application. A cutaway sketch of such a machine is shown in figure 16. The unusual spherical air gap is required to allow angular tipping of the flywheel by the large angle magnetic suspension, discussed above. The following few paragraphs briefly discuss the unique spherical air gap design. For a more detailed description of the machine and presentation of the design analysis, refer to the recent thesis by Larkin [1985], "Design and Optimization of a Motor/Generator for Use in a Satellite Flywheel Energy Storage System".

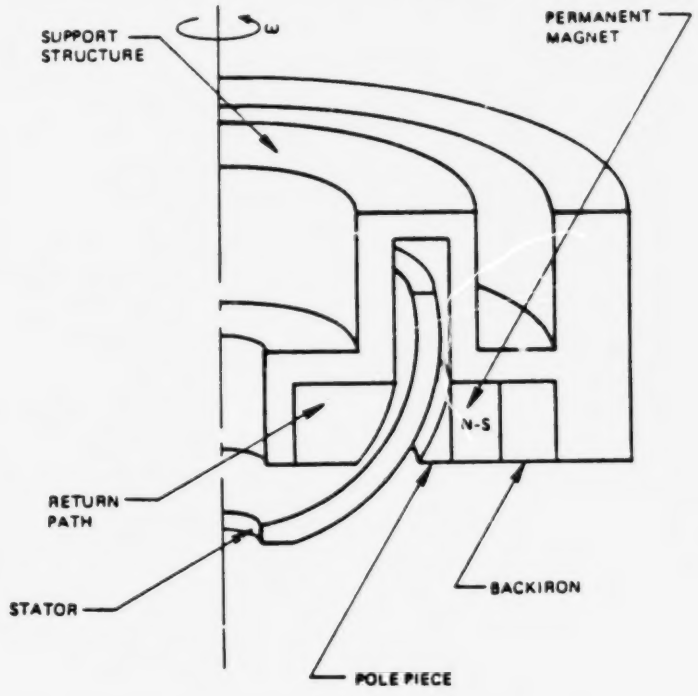

Figure 16. Spherical Air-gap Ironless Stator/Rotating Back-iron PM Machine

As shown in figure 16, all steel portions rotate with the machine ("rotating back-iron") while the stator is comprised of copper windings and a thermal/structural epoxy support ("ironless stator"). The spherical design for the air gap and stator is required to allow tipping of the rotor.

The rotor assembly is shown in figure 17 and depicted schematically in plan view in figure 18. The rotor is comprised of a back-iron, a magnetic ring, eight pole pieces and a return

path. The cylindrical permanent magnet ring is made up of eight radially magnetized, alternating N-S segments of $SmCo_5$ permanent magnet. The steel alloy cylindrical back-iron and spherical-sided return path are sized to carry the magnetic flux. The wedge-shaped steel alloy pole pieces shape the magnetic field over the spherical air-gap.

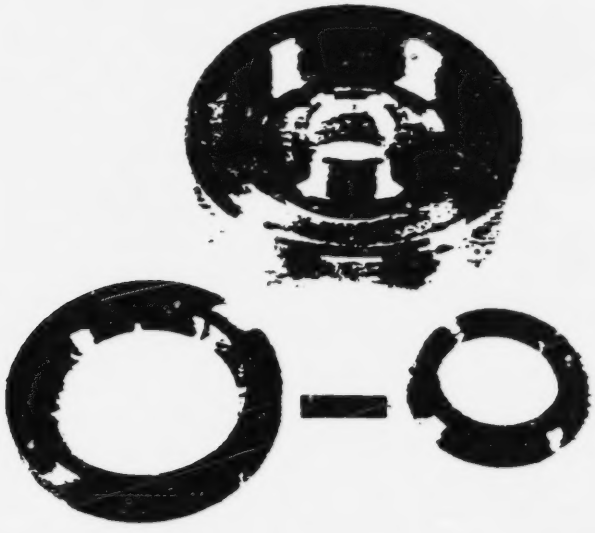

Figure 17. Prototype Motor/Generator Rotor

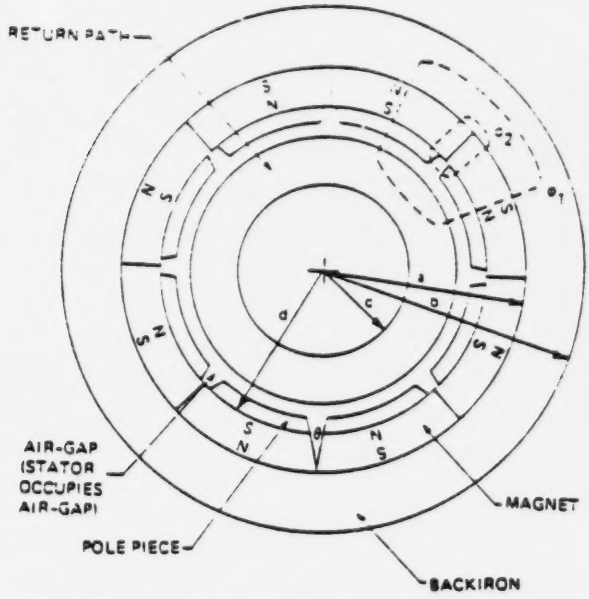

a = back-iron outer diameter
b = back-iron inner diameter
c = return path inner diameter
d = magnetic ring inner diameter
ϕ_1 = useful flux
ϕ_2 = leakage flux

Figure 18. Spherical Air-gap Ironless PM Rotor Sketch - Plan View

ORIGINAL PAGE IS
OF POOR QUALITY

ORIGINAL PAGE IS
OF POOR QUALITY

The stator, shown in figure 19, is a three-phase, 2/3 pitch design. Each phase is made up of 5 turns/pole/phase (120 stator turns total). The winding material is Litz wire, a braided cable made up of individual thin strands of copper wire. The type of Litz wire selected for this application is comprised of 96 strands of number 36 AWG wire. The free standing coils are potted in a high thermal conductivity epoxy for structural support and cooling.

Figure 19. Prototype Motor/Generator Stator

2.3 Flywheel and Spoke Structure

One of the requirements of a competitive flywheel energy storage system for space-based applications is high energy storage per unit mass (specific energy density). To accomplish this, the spin-induced stresses in the flywheel must approach the limits of the flywheel imposed by the flywheel material. Simple stress analysis of flywheels indicates that the greater the strength-to-weight ratio of the material, the higher the achievable specific energy density. Therefore, fiber-based composite materials, because of their high specific strength, should be employed.

On the other hand, although composites have good strength along the fiber, or tangential, direction, they are relatively weak along the radial direction. For example, the off axis strength of boron/epoxy composites is only 5.2% of the strength in the fiber direction [Foley 1986, p14]. In order to keep the stresses in the radial direction low and thereby maintain optimal energy density, composite flywheels usually take the form of relatively thin rings. Therefore, as the flywheel approaches

ultimate strain at the higher rotational speeds, it can undergo large radial displacements.

The problem with large radial displacements is that the classic non-compliant radial spoke can not support them. As the speed increases, these spokes will place large radial loads in an attempt to constrain the wheel's growth, resulting in wheel burst below predicted speeds. Flywheel systems have been developed with radially preloaded flywheels, loaded such that a compressive load always exists between the spoke and flywheel. The logic behind this scheme is that the flywheel never grows enough to put tension on the spokes. At the ultimate speeds, however, nearly the entire radial centripetal weight of the spoke would be supported by the inner hub assembly. Since the hub assembly of the ACCESS system contains the electromagnetic bearings and motor/generator rather than a solid shaft, it is simply not strong enough to support radial loads as large as these.

The size and shape of the flywheel combined with the sensitivity of the hub assembly leads to the realization that to preserve optimality, the attachment structure used between the hub and flywheel must be compliant so that it can grow with the wheel. Other requirements include the desire for controller simplification to decouple the tilt (angular) dynamics from the translational (radial) dynamics. The ACCESS laboratory module was sized for a boron/epoxy flywheel 13 cm tall with an inner and outer radius of 20 cm and 25 cm respectively. This 17 kg flywheel was to have an approximate top speed of 20000 rpm. Because of scheduling and cost constraints, a high-strength steel flywheel of similar inner radius and mass was used instead of the composite wheel. This flywheel has a maximum speed of approximately 16000 rpm. The important inertia properties of this wheel are given in Table XI.

TABLE XI. ACCESS LABORATORY FLYWHEEL INERTIA VALUES

	Flywheel	Hub	Total
Mass (kg)	17	19	36
Axial Moment of Inertia I_{zz} (kgm^2)	0.70	0.10	0.80
Radial Moment of Inertia I_{rr} (kgm^2)	0.37	0.090	0.46

Despite the many constraints placed on size, shape, and orientation of the ACCESS spokes, several different candidate configurations exist. A recent thesis by Foley [1986] develops and analyzes these different spoke configurations. Figures 20, 21, 22, and 23 are examples of spoke designs that were analyzed by Foley.

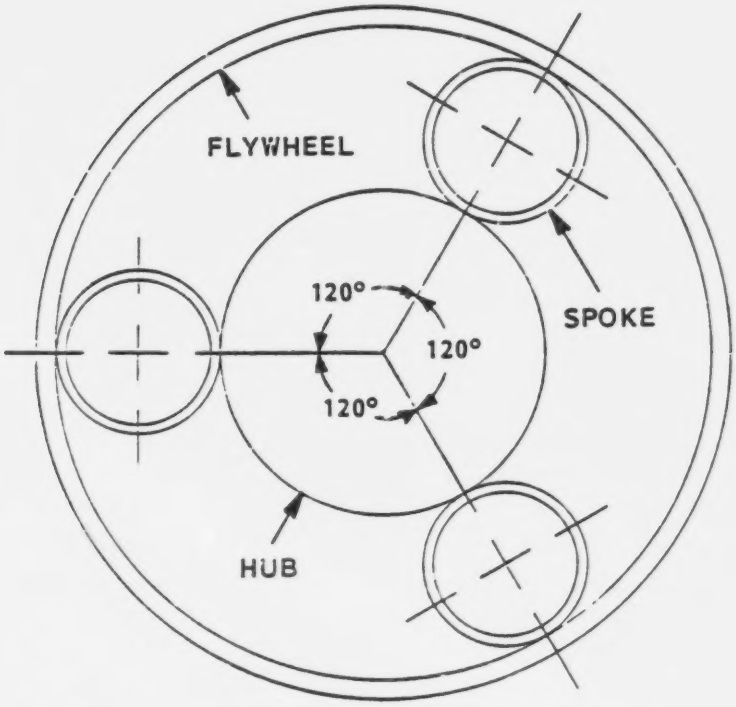

Figure 20. Configuration Using 3 Cylinder Supports

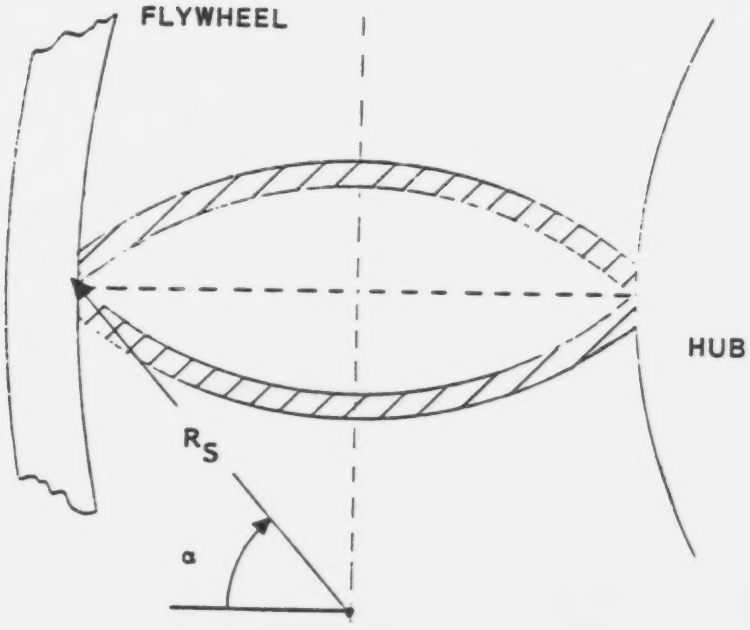

Figure 21. Sample Arc-spoke

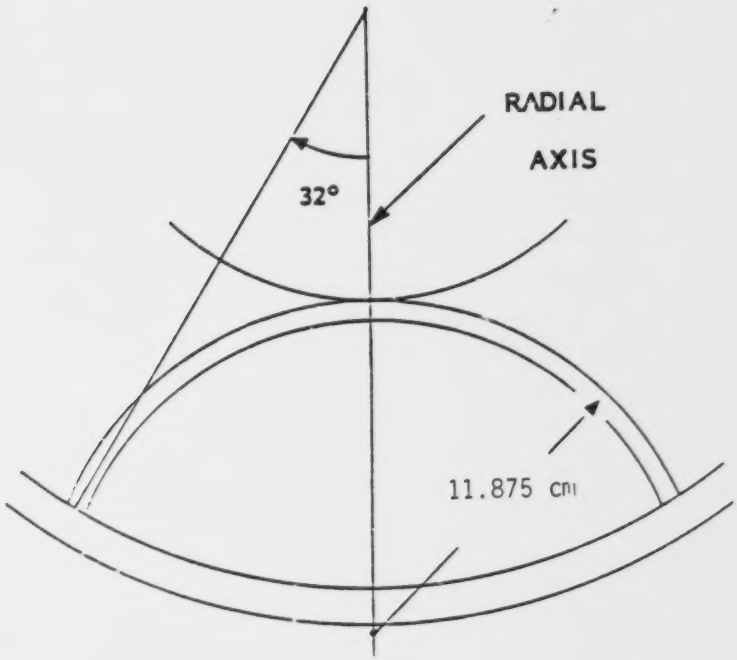

Figure 22. Best U-spring Spoke

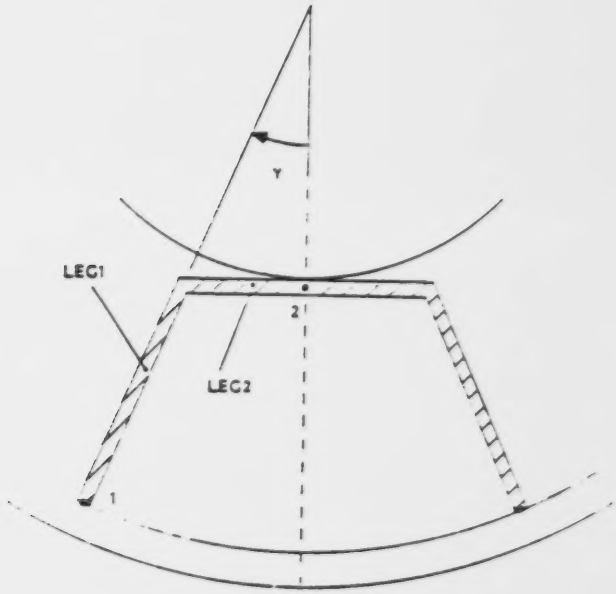

Figure 23. Sample Dogleg Spoke

The final design, an optimized dogleg spoke, is shown in figure 24. The spoke structure characteristics of concern for the dynamic model are the radial and angular stiffness and damping. The stiffnesses of the individual spokes were statically measured. Based on these measurements, the stiffnesses of the total spoke structure can be calculated. No measurements of the ACCESS spoke damping have been made. The damping parameters will be somewhat arbitrarily selected to give a loss factor at resonance of 0.01 (a damping ratio of 0.005). The measured, calculated, and assumed spoke structure characteristics are given in Table XII.

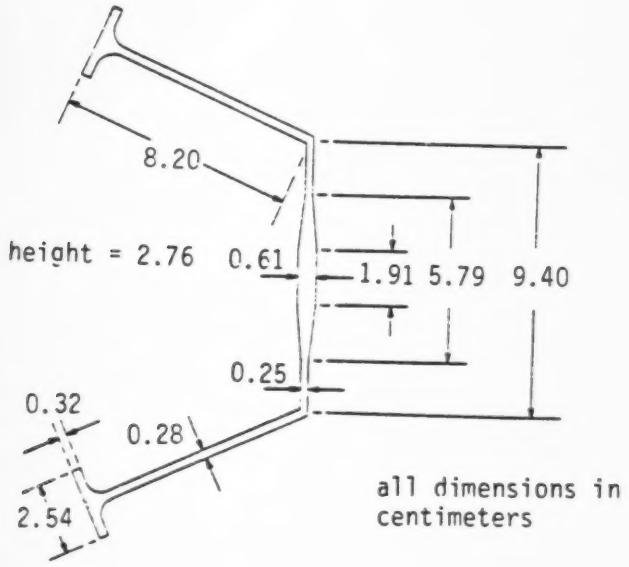

Figure 24. Optimized Dogleg Spoke

TABLE XII. ACCESS SPOKE CHARACTERISTICS

Translational Characteristics

Stiffness	k_r	4.1×10^6 N/m
Damping	c_r	61 kg/sec

Angular Characteristics

Stiffness	k_a	1.0×10^5 Nm/rad
Damping	c_a	0.87 kgm^2/sec

3. SYSTEM DYNAMICS MODEL

Based on the subcomponent models discussed in Chapter 2, a model of the system dynamics was developed. A general block-diagram of the system is shown in figure 25. The rotor is controlled by forces and torques provided by the actuator, the Lorentz-force, large angle magnetic bearing presented earlier. The positions and tilt angles of the hub and flywheel are measured and used as inputs to the controller. The outputs of the controller are signals controlling the power amplifiers that drive the magnetic bearing. For conventional magnetic bearings, the bearing forces and torques would also be a function of the displacements of the hub as well as input currents, as shown by the dashed lines. For the Lorentz-force bearing such as used in the ACCESS system, however, there is no force-displacement coupling to first order.

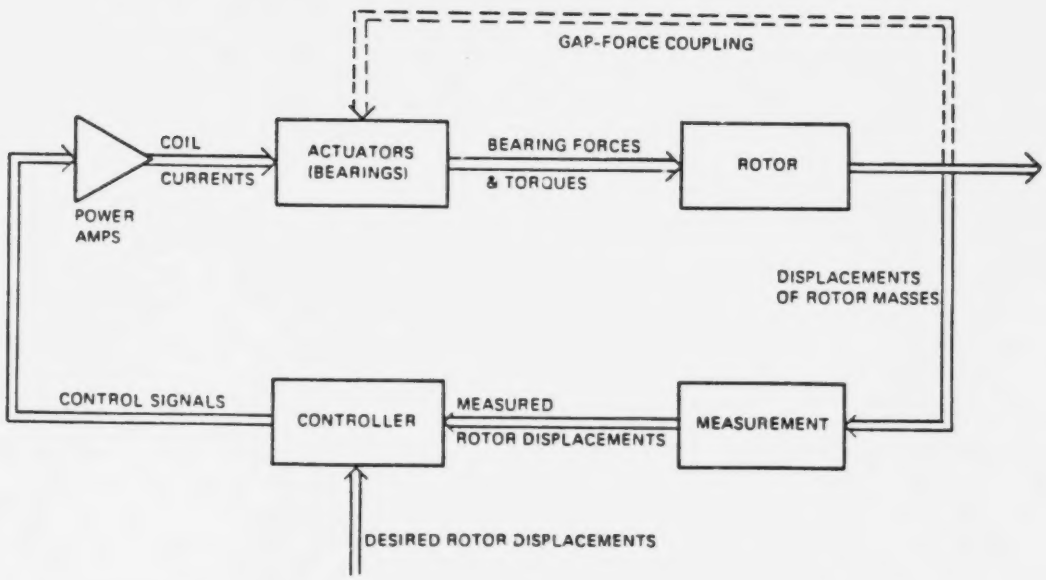

Figure 25. Block Diagram of a Magnetic Bearing System

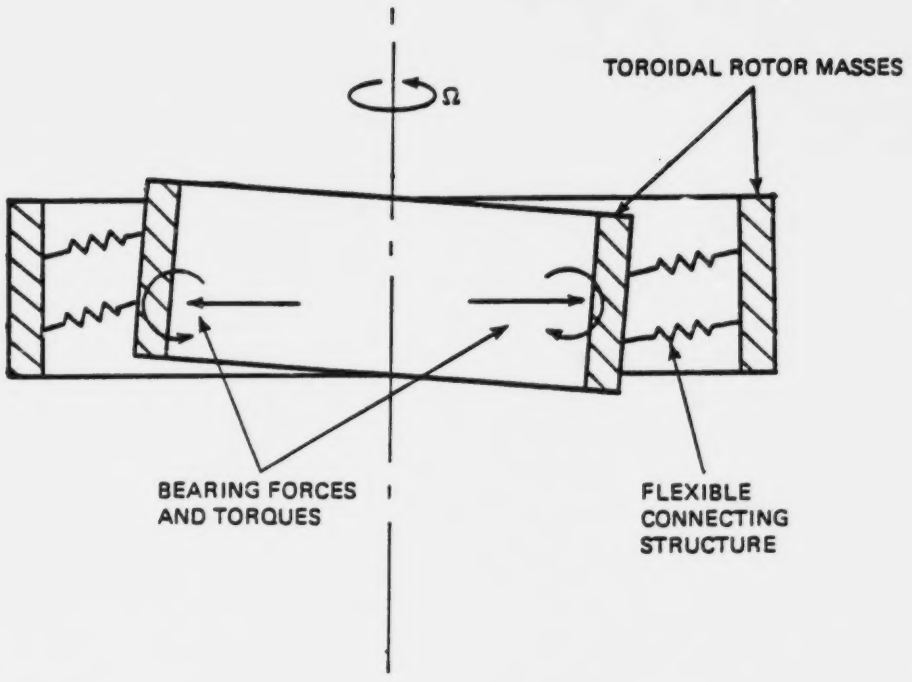

Figure 26. Cut-away of a Toroidal, Multi-body, Flexible Rotor System.

The ACCESS hardware is modelled as two rigid body masses, the hub and the flywheel, connected by a damped, elastic structure, the spokes system. The magnetic suspension force torque act on the hub, as shown in figure 26. Each of the rigid-body masses in figure 26 has three translational and three angular degrees of freedom. This research did not address the dynamics of two of these degrees of freedom, the translational degree of freedom along the axial direction or the angular degree of freedom associated with the spin axis. The axial, translational degree of freedom is neglected because to first order its dynamics are not a function of rotational speed and do not couple with the dynamics of the other degrees of freedom. Control of these axial dynamics is the subject of work by [Downer 1980] for an all-active magnetic bearing system. Angular displacement control of the spin axis angular degree of freedom is not usually desired, only angular velocity control. Also, these torsional dynamics are not usually controllable by the magnetic bearing system. They may have, however, important effects on the motor controller dynamics. This problem is not addressed in this report.

The model development will be briefly sketched here, more detail can be found in a recent thesis by Johnson [1987] and

Appendix A. The system model development starts by obtaining the relations between applied force and torque and the resulting position and orientation of each rigid body mass. Small angular motions are assumed, leading to linearized relations. The force and torque produced by the spoke structure are then related to the relative positions and orientations of the hub and flywheel. These relations describing the spoke structure will also be assumed linear. The bearing force and torque and measurement system descriptions are then added to complete the system model.

For use in the research reported here, perfect inertial and spoke geometries were assumed, analogous to assuming a perfectly balanced conventional rotor system. Other assumption, either made explicitly or implicitly include:

1) The flywheel and hub are assumed to behave as rigid-bodies over the frequency range of interest.

2) The rigid-bodies have an axis of symmetry, which is the nominal spin axis.

3) The dynamics of the rotational speed are slow compared to the flexible mode frequencies.

4) The angular orientation of the rigid bodies, that is the amount of tipping, is small.

5) The spoke structure is a linear, elastic structure with linear damping

6) The nominal spin axis of the hub and flywheel is an axis of symmetry for the spoke structure which, therefore, is assumed to have rotationally anisotropic translational and angular stiffnesses. This implies that there is no torque-radial displacement or force-angular displacement coupling and that the tensor relation between generalized displacements and generalized forces reduces to scalar relations [Foley 1986].

7) The force generated by the spoke structure acts through the centers of mass of the hub and flywheel.

8) The spokes are very light compared to the hub or flywheel masses.

9) The bearing force and torque depend only on input current and are linear with current.

10) The bearing force acts through the center of mass of the hub.

11) The measurement system measures the position of the hub

center of mass and the orientation of the hub nominal spin axis.

These assumptions lead to a model capable of predicting the non-synchronous response of the system, which is the focus of this report. With these assumptions, the system dynamics decouple into two separate models, one describing the translational (radial) dynamics and the other describing the angular (tilt) dynamics. Also, because of the axial symmetry, complex notation can be advantageously used, reducing the size of the system descriptions and providing increased physical insight [Johnson 1987, Chapter 4]. The following two sections present the translational and angular models along with their open-loop properties.

3.1 Translational Open-Loop Model

The open-loop translational model is described by a eight state system. The states consist of the flywheel and hub position and velocity in the x and y (radial) directions. Using complex notation, this state is given by

$$\underline{z} = [z_f,\ z_h,\ \dot{z}_f,\ \dot{z}_h]^T$$

where

$z = x + jy$,
j = square root of -1,
the f and h subscripts refer to flywheel and hub.

Put into state-space form, with complex state variables, these equations of motion are

$$\dot{\underline{z}} = \begin{bmatrix} 0 & I \\ -(K_t - j\Omega C_t) & -C_t \end{bmatrix} \underline{z} + \underline{f}_c$$

where the normalized radial damping matrix C_t and radial stiffness matrix K_t are

$$C_t = \begin{bmatrix} \frac{c_t}{m_f} & \frac{-c_t}{m_f} \\ \frac{-c_t}{m_h} & \frac{c_t}{m_h} \end{bmatrix} \qquad K_t = \begin{bmatrix} \frac{k_t}{m_f} & \frac{-k_t}{m_f} \\ \frac{-k_t}{m_h} & \frac{k_t}{m_h} \end{bmatrix}$$

where

k_t and c_t are the spoke radial stiffnesses and damping
m_f and m_h are the flywheel and hub masses,

$\underline{f}_c$ is a vector of normalized, complex bearing control forces

$$\underline{f}_c = [0,\ 0,\ 0,\ (f_x + jf_y)/m_h]^T$$

where

f_x and f_y are the bearing x and y direction forces,
and Ω is the rotational speed.

The important destabilizing effect of internal (spoke) damping can be seen in the ΩC_t term in the above equations.

Substituting the subcomponent values for the above parameters yields the following complex representation of the translational dynamics,

$$\dot{\underline{z}}(t) = A_c(\Omega)\underline{z}(t) + \underline{b}_c f_c(t)$$

$$y_c(t) = \underline{c}_c^T \underline{z}(t)$$

where

$\underline{z}$ = vector of complex hub and flywheel positions and velocities in units of meters or meters per second

f_c = complex force expressed in Newtons

y_c = complex scalar representing the hub measured position in units of meters.

Using the parameter values developed above, these matrices have the following numerical values for the laboratory module.

$$A_c = \begin{bmatrix} 0 & 0 & 1 & 0 \\ 0 & 0 & 0 & 1 \\ -2.47 \times 10^5 + j3.63\Omega & 2.47 \times 10^5 - j3.63\Omega & -3.63 & 3.63 \\ 2.16 \times 10^5 - j3.17\Omega & -2.16 \times 10^5 + j3.17\Omega & 3.17 & -3.17 \end{bmatrix}$$

$$\underline{b}_c = \begin{bmatrix} 0 \\ 0 \\ 0 \\ 5.26 \times 10^{-2} \end{bmatrix} \qquad \underline{c}_c^T = [0,\ 1,\ 0,\ 0]$$

where

Ω = rotational speed measured in rad/sec.

Note that this is a linear, time invariant system that is a function of the rotational speed Ω. Also, using the complex notation, this is single-input, single-output system that can be described by a complex coefficient transfer function (CCTF) [Johnson 1987, Section 4.11].

The controllability and observability of this system were examined over a wide speed range. The translational dynamics have been shown to be controllable through application of the bearing force and observable though measurements of the hub position [Johnson 1987]. The translational ACCESS model is therefore a well posed control problem.

The most important feature of the open-loop translational model is that it becomes unstable at super flexible rotational speeds. This is shown in figure 27, a root-locus of the pole and transmission zero locations of the complex representation as the rotational speed is changed. The system is described by a pair of poles at the origin corresponding to the rigid body motion of the hub and flywheel in both x and y directions. The other pole and transmission zeros describe the reduced-mass vibration of the hub-spoke-flywheel system. Using the complex representation, these flexible-mode resonances in the x and y directions can be considered as forward and backward whirl modes in the usual rotordynamic fashion [Johnson 1987, Section 5.2]. The pole and transmission zero with positive imaginary parts correspond to the forward whirl mode. The pole and transmission zero with negative imaginary parts correspond to the backward whirl mode.

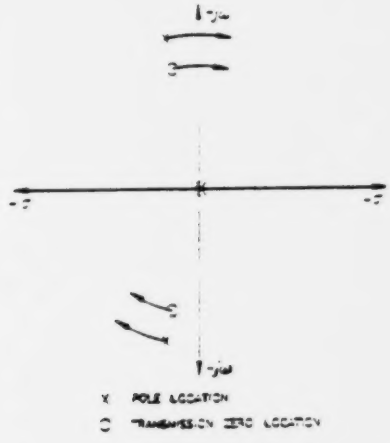

Figure 27. Root-Locus as a Function of Rotational Speed, Open-Loop Translational Model

As the rotational speed is increased, the pole and transmission zeros move from their zero speed locations, as shown by the arrows in figure 27. At super flexible rotational speeds, the forward whirl pole and transmission zero have moved into the right half plane, indicating that the system has become open-loop unstable. The movement of the forward whirl mode into the right-half plane can also be seen in figure 28, a plot of the flexible-mode damping versus rotational speed. The damping of the forward flexible mode (solid curve) becomes negative and the open-loop system unstable at a rotational speed of 680 rad/sec.

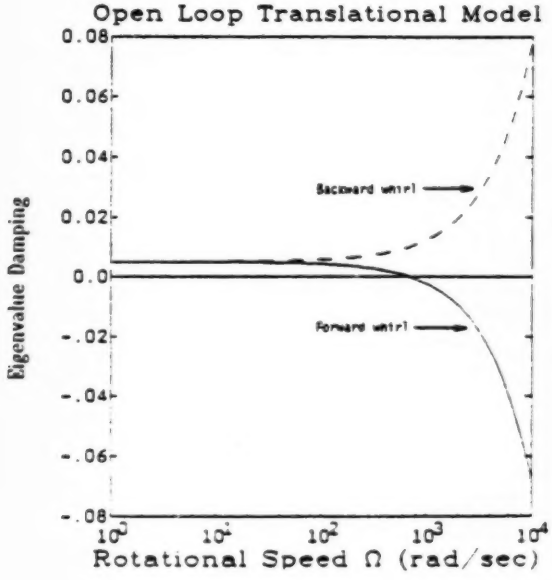

Figure 28. Eigenvalue Damping versus Rotational Speed for the Open-loop Translational Model

The Bode plot of the system at zero rotational speed is shown in figure 29. The system falls off at a slope of -2 because of the double integration of the rotor mass. The effect of the hub-spoke-flywheel resonance is seen by the zero (trough) and pole (peak) in the amplitude. Note that the resonance occurs at about 670 rad/sec, within the rotational speed range of the system. At a super-flexible rotational speed of 1000 rad/sec, the system has become unstable and the forward and backward transfer functions ($s = +j\omega$) and ($s = -j\omega$) have become distinct because of the complex nature of the representation [Johnson 1987, Chapter 4]. The magnitude response is similar to the zero speed case, but the forward (solid curve) and backward (dashed curve) transfer functions have different phase as can be seen in figure 30.

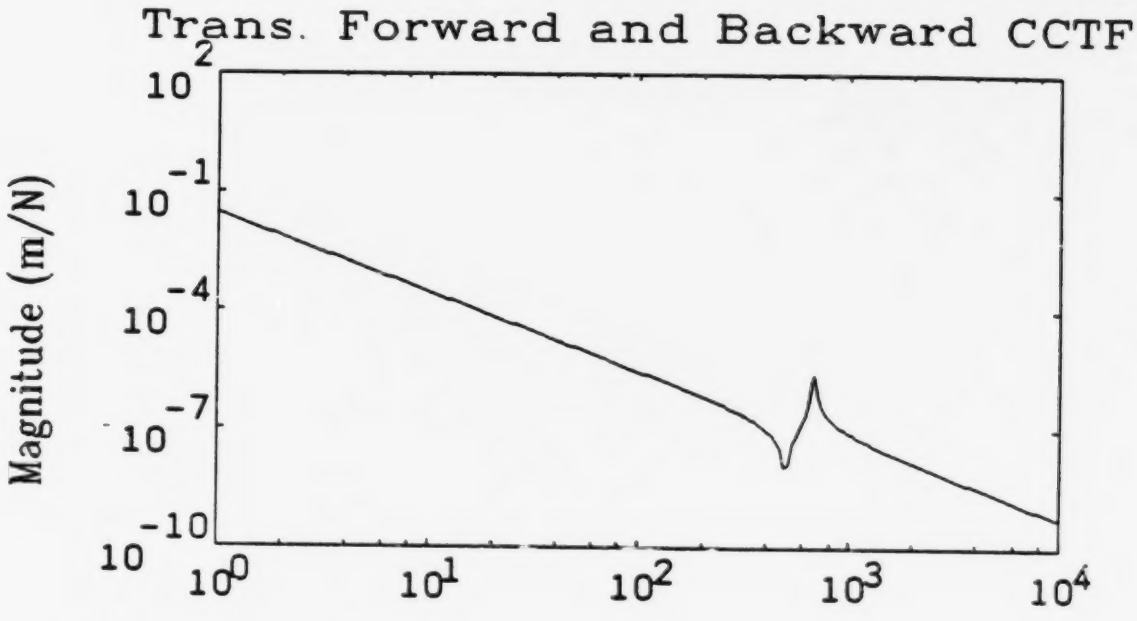

a) Magnitude

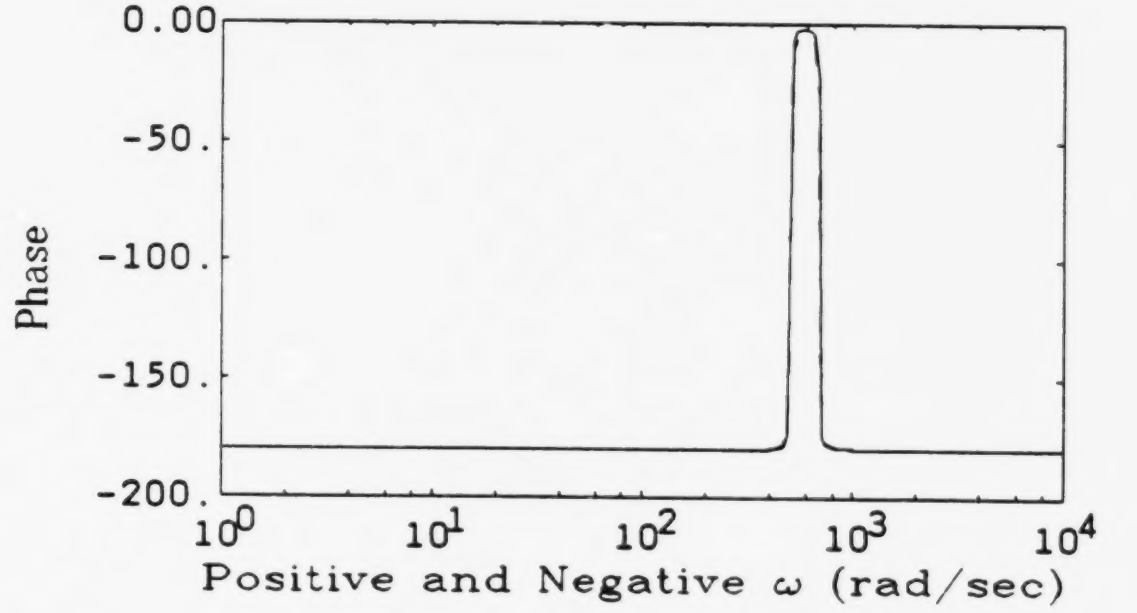

b) Phase

Figure 29. Bode Magnitude and Phase Plots of the Complex Coefficient Transfer Function for Positive and Negative Frequencies: Translational Model at a Sub-flexible Rotational Speed of 100 rad/sec

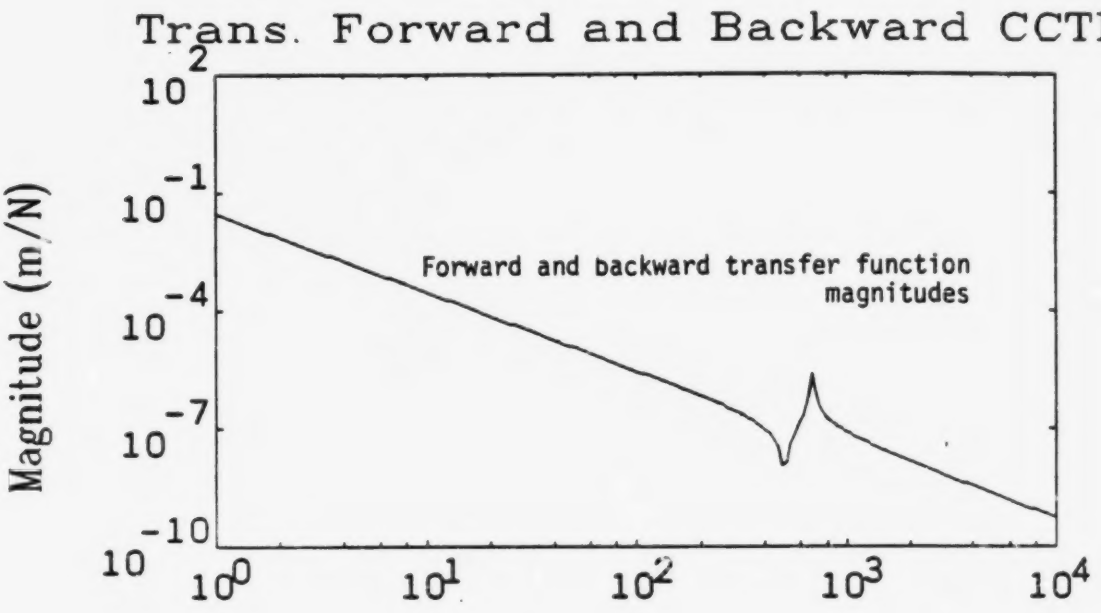

a) Magnitude

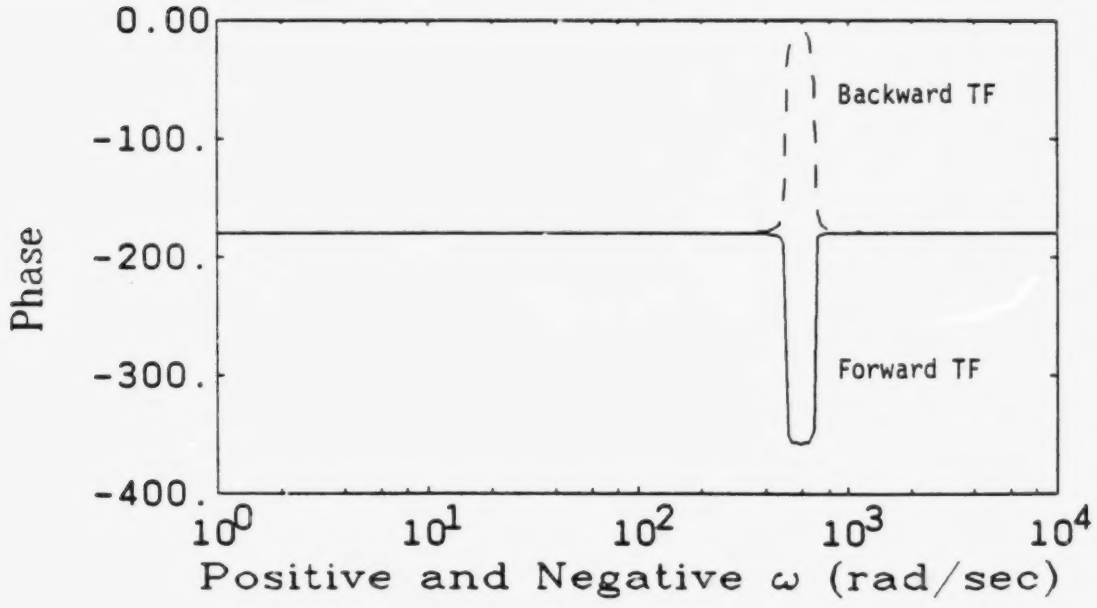

b) Phase

Figure 30. Bode Magnitude and Phase Plots of the Complex Coefficient Transfer Function for Positive and Negative Frequencies: Translational Model at a Super-flexible Rotational Speed of 1000 rad/sec

3.2 Angular Open-Loop Model

The open-loop angular model has a similar form to the translational model with the addition of gyroscopic terms. The angular model is described by an eight state system. The states consist of the flywheel and hub orientation (tilt) and angular velocity about the x and y (radial) directions. Using complex notation, this state is given by

$$\underline{z} = [\psi_f, \psi_h, \dot{\psi}_f, \dot{\psi}_h]^T$$

where

$\psi = \phi + j\theta$,
ϕ = tilt (orientation) of the body relative to the x axis
θ = tilt (orientation) of the body relative to the y axis
j = square root of -1,
the f and h subscripts refer to flywheel and hub.

Put into state-space form, with complex state variables, these equations of motion are

$$\dot{\underline{z}} = \begin{bmatrix} 0 & I \\ -(K_a - j\Omega C_a) & -(C_a - j\Omega G) \end{bmatrix} \underline{z} + \underline{\tau}_c$$

where the normalized angular damping matrix C_a, gyroscopic matrix G, and angular stiffness matrix K_a are given by

$$C_a = \begin{bmatrix} \frac{c_a}{I_{fr}} & \frac{-c_a}{I_{fr}} \\ \frac{-c_a}{I_{hr}} & \frac{c_a}{I_{hr}} \end{bmatrix} \quad G = \begin{bmatrix} 0 & \frac{I_{fz}}{I_{fr}} \\ \frac{I_{hz}}{I_{hr}} & 0 \end{bmatrix} \quad K_a = \begin{bmatrix} \frac{k_a}{I_{fr}} & \frac{-k_a}{I_{fr}} \\ \frac{-k_a}{I_{hr}} & \frac{k_a}{I_{hr}} \end{bmatrix}$$

where

- k_a and c_a are the spoke angular stiffnesses and damping
- I_{hr} and I_{fr} are the hub and flywheel radial moments of inertia,
- I_{hz} and I_{fz} are the hub and flywheel axial moments of inertia,

$\underline{\tau}_c$ is a vector of normalized, complex bearing control torques

$$\underline{\tau}_c = [0, 0, C, (\tau_x + j\tau_y)/I_{hr}]^T$$

where

τ_x and τ_y are the bearing x and y direction torques,

and Ω is the rotational speed.

Substituting the subcomponent values for the above parameters yields the following complex representation of the angular dynamics,

$$\dot{\underline{z}}(t) = \mathbf{A}_C(\Omega)\underline{z}(t) + \underline{b}_C r_C(t)$$

$$y_C(t) = \underline{c}_C^T \underline{z}(t)$$

where

$\underline{z}$ = vector of complex hub and flywheel orientations and angular velocities in units of radians or radians per second

r_C = complex torque expressed in Newton-meters

y_C = complex scalar representing the hub measured orientation in units of radians.

Using the parameter values developed above, these matrices have the following numerical values for the laboratory module.

$$\mathbf{A}_C =$$

$$\begin{bmatrix} 0 & 0 & 1 & 0 \\ 0 & 0 & 0 & 1 \\ -2.78 \times 10^5 + j2.32 & 2.78 \times 10^5 - j2.32 & -2.32 + j1.87 & 2.32 \\ 1.16 \times 10^6 - j9.68 & -1.16 \times 10^6 + j9.68 & 9.68 & -9.68 + j1.14 \end{bmatrix}$$

$$\underline{b}_C = \begin{bmatrix} 0 \\ 0 \\ 0 \\ 11.2 \end{bmatrix} \qquad \underline{c}_C^T = [0, \ 1, \ 0, \ 0]$$

where

Ω = rotational speed measured in rad/sec.

These complex matrices have a similar form to the

translational matrices except for the addition of gyroscopic terms proportional to rotational speed Ω. These gyroscopic terms appear in the last two diagonal elements of the complex state dynamics matrix A_C.

The controllability and observability of angular dynamics were investigated as a function of the rotational speed. For a wide speed range, $0 \leq \Omega \leq 10^5$, the angular model is controllable through application of the bearing torque and observable through measurements of the hub position. The angular ACCESS model is therefore a well posed control problem.

In contrast to the translational model, the angular model is open-loop stable at all rotational speeds. Unlike the translational model, the frequency of the open-loop eigenvalues is a strong function of rotational speed because of the gyroscopic effects. This is shown in figure 31, a root-locus of the open-loop pole and transmission zero locations versus rotational speed. At zero speed the system is described by two poles at the origin representing the rigid-body dynamics and the pair to poles and transmission zeros representing the flexible mode dynamics, similar to the translational model. As the rotational speed is increased the poles and transmission zeros move in the directions indicated by the arrows. Note that because of gyroscopic effects, one of the rigid-body poles located at the origin at zero speed moves upward along the jw axis, in contrast to the translational model.

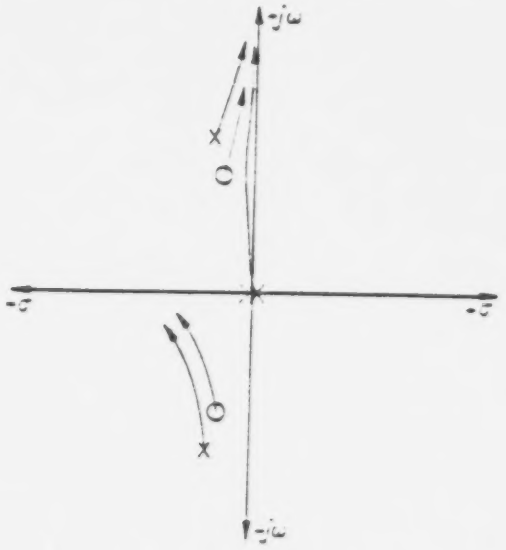

Figure 31. Root Locus versus Rotation Speed: Open-loop Angular Model

The movement of the open-loop poles as a function of rotational speed can be dramatically seen in figure 32, which are plots of open-loop eigenvalue frequency and damping versus rotational speed. Again, the forward whirl modes are indicated by solid curves and the backward whirl modes by dashed curves. Note that the forward whirl modes increase in frequency with increasing speed and the flexible backward mode decreases.

Bode plots of the open-loop angular dynamics are shown in figures 33 through 35. At zero rotational speed, figure 33, the Bode plot has a similar form to the translational dynamics but with a slightly higher flexible-mode eigenvalue frequency of 1200 rad/sec. As the rotational speed is increased, figures 34 and 35 the forward and backward transfer functions become distinct, both in phase and magnitude. Also note the overall reduction in open-loop gain as the speed is increased (compare figure 33a to 35a).

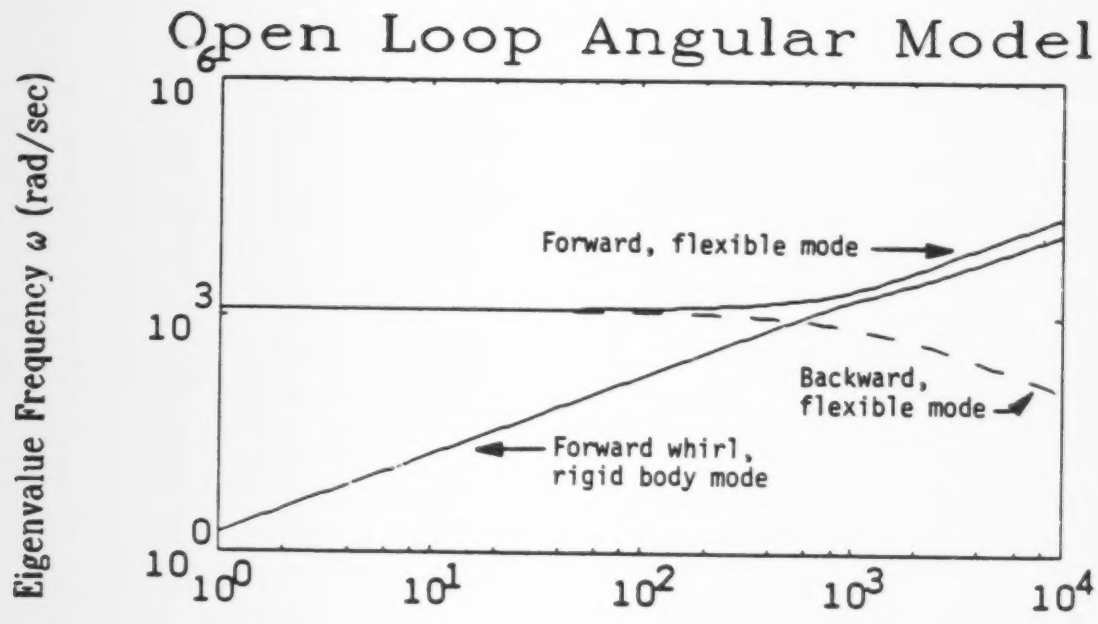

a) Eigenvalue Frequencies

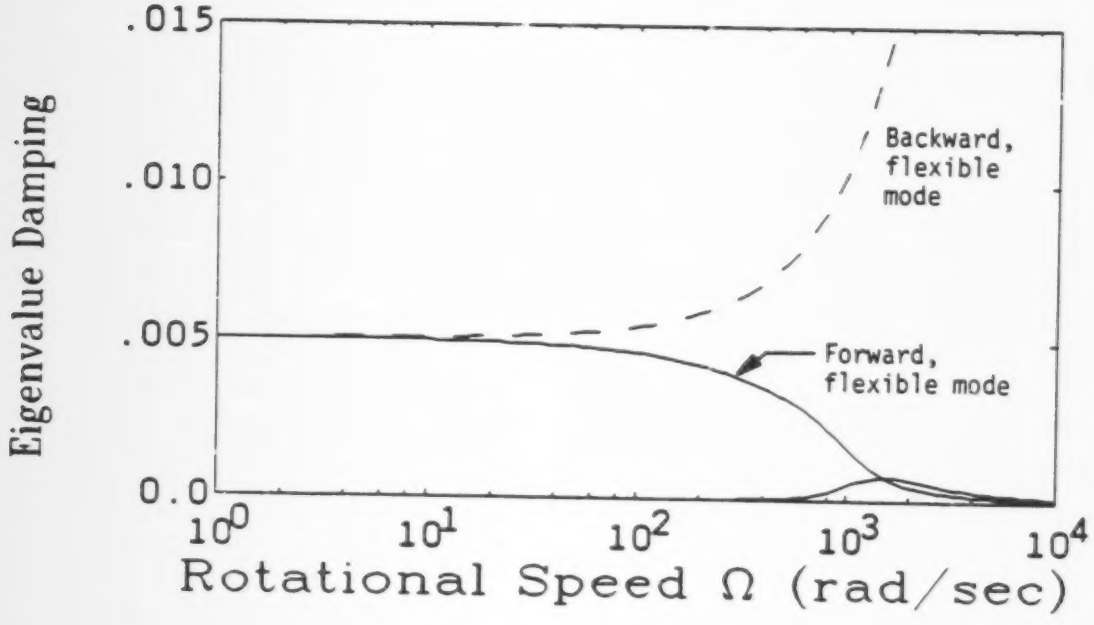

b) Eigenvalue Damping

Figure 32. Eigenvalue Frequency and Damping

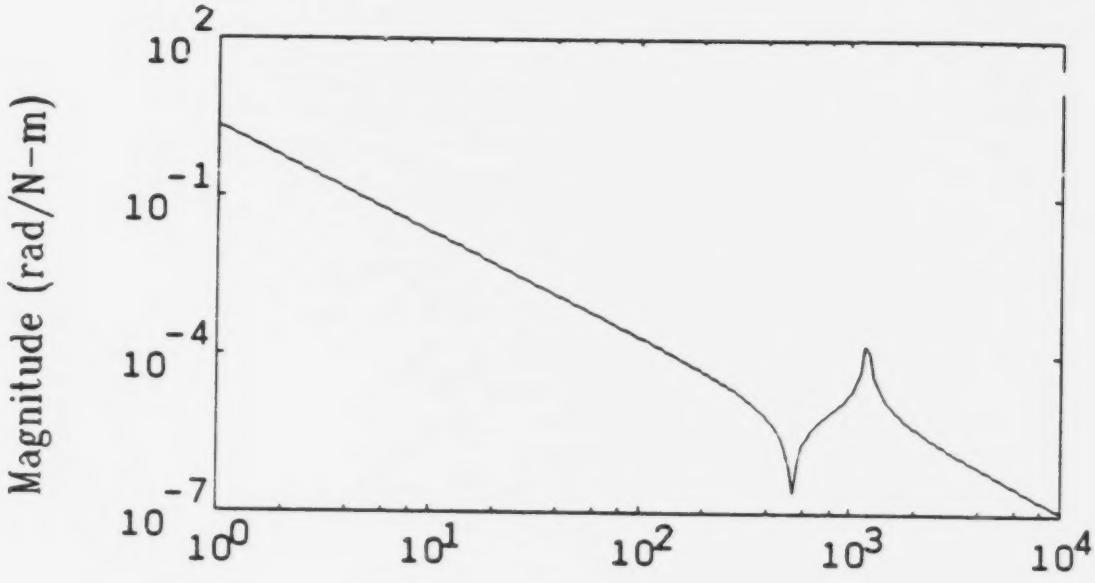

a) Magnitude

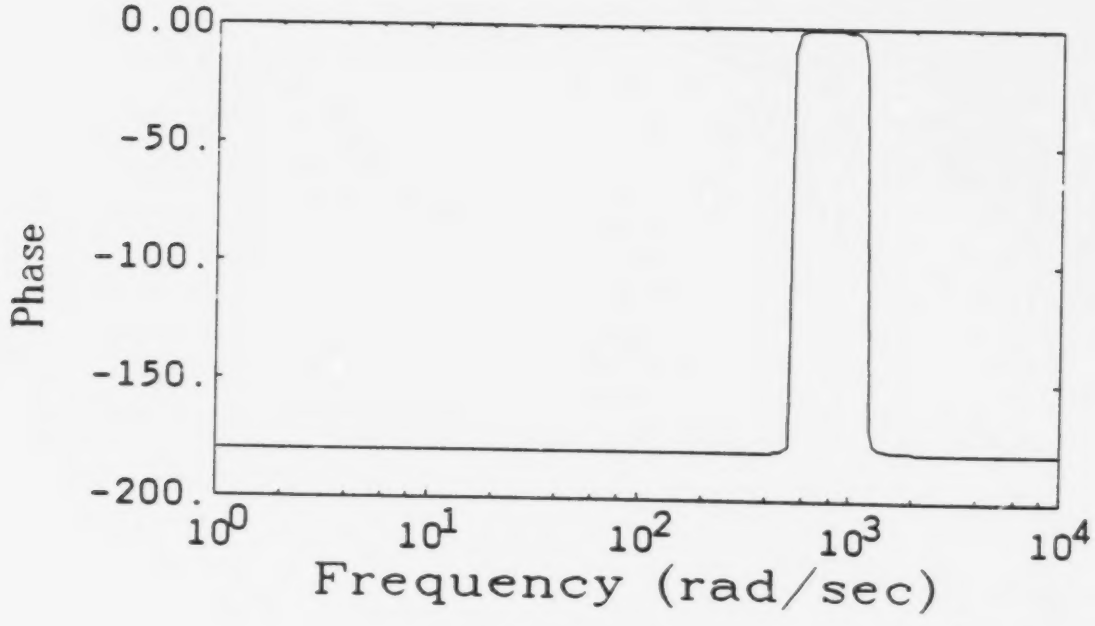

b) Phase

Figure 33. Bode Magnitude and Phase Plots of the Parallel Complex Coefficient Transfer Functions: Angular Model at Zero Rotational Speed.

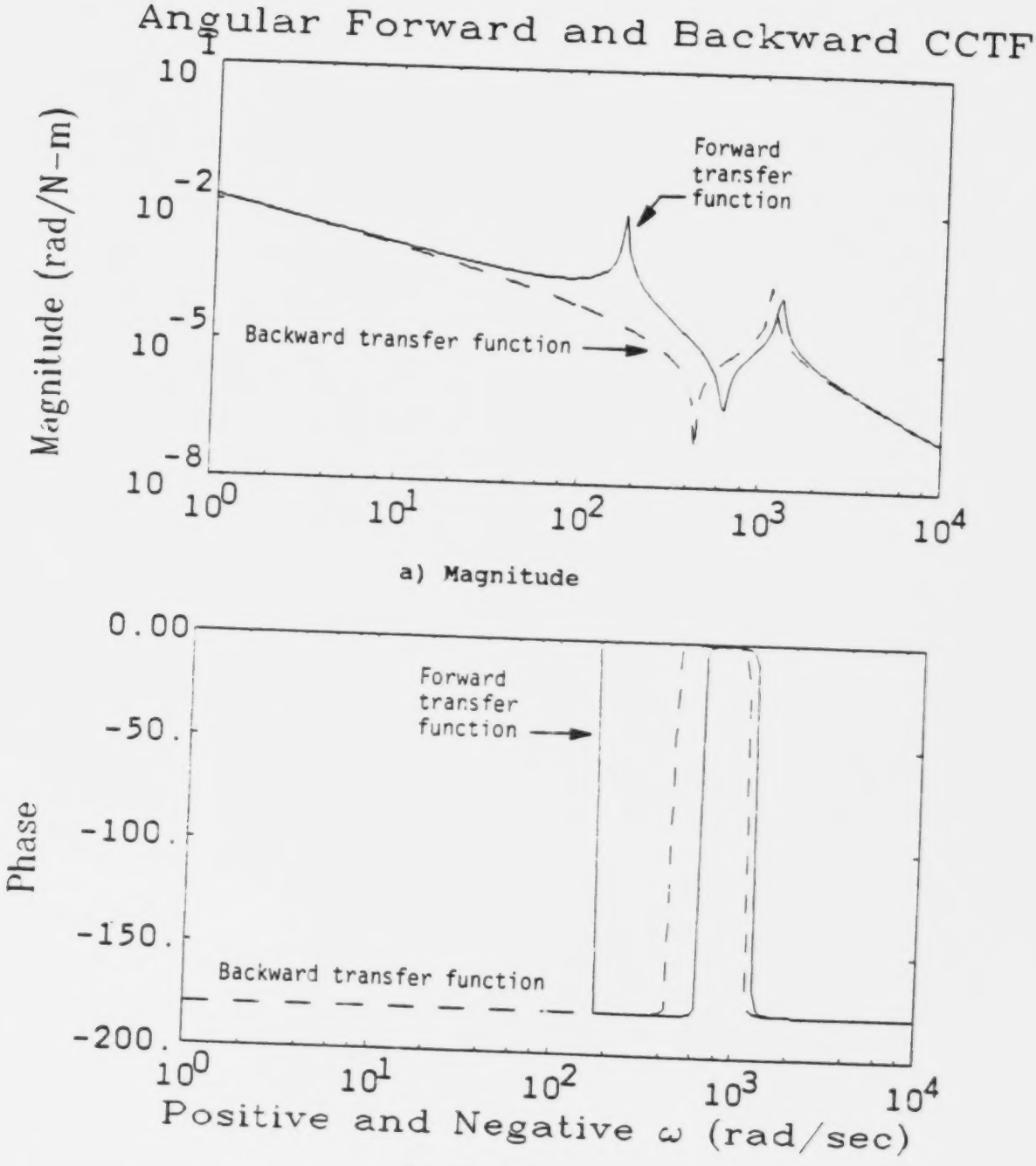

Figure 34. Bode Magnitude and Phase Plots of the Complex Coefficient Transfer Function for Positive and Negative Frequencies: Open-loop Angular Model at a Sub-flexible Rotational Speed of 100 rad/sec

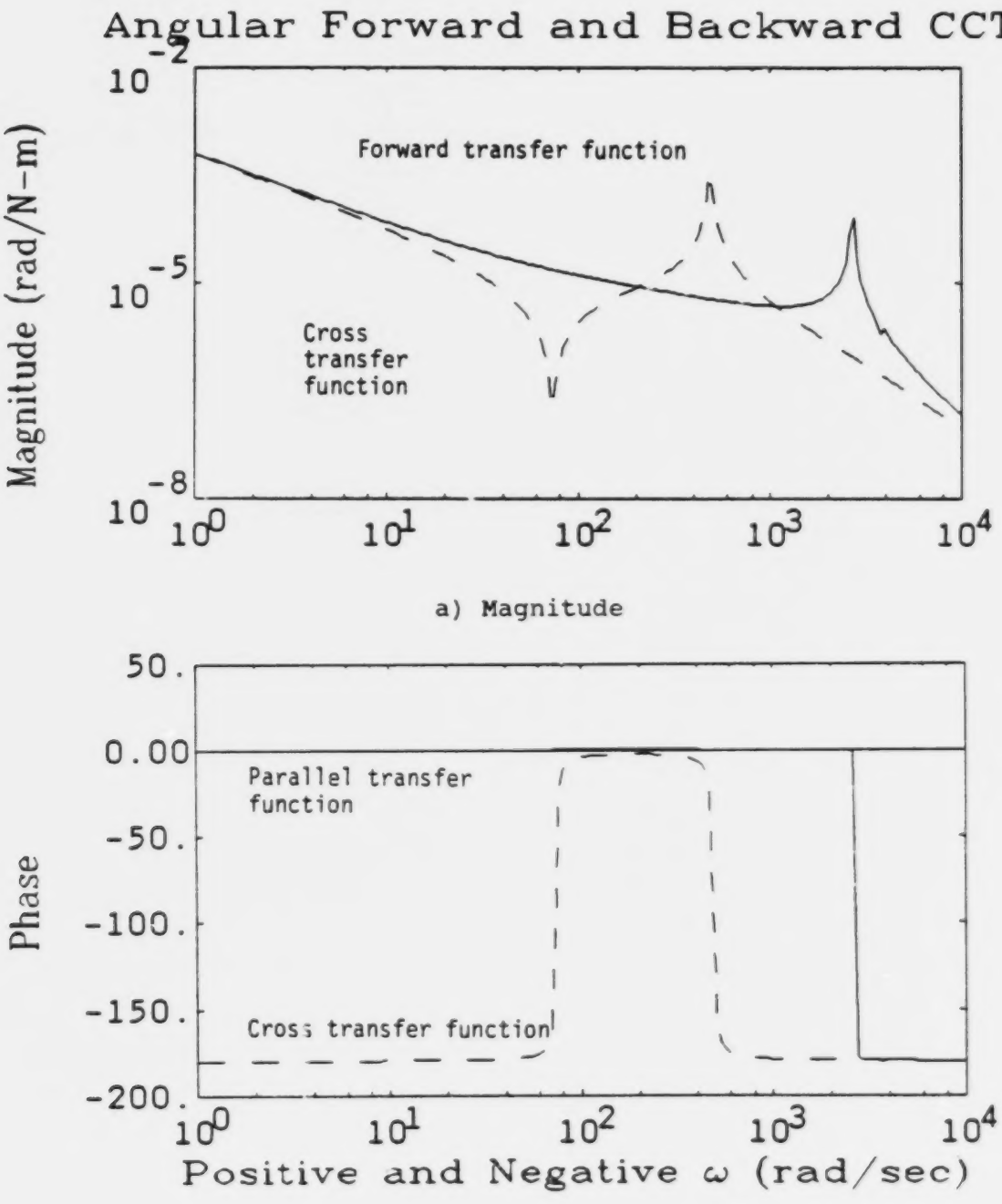

Figure 35. Bode Magnitude and Phase Plots of the Complex Coefficient Transfer Function for Positive and Negative Frequencies: Open-loop Angular Model at a Super-flexible Rotational Speed of 2000 rad/sec

4. STABILITY REQUIREMENTS

The open-loop ACCESS system was seen in the last chapter to present an interesting variety of control problems. The dynamics were decoupled into two models, a translational model and an angular model. Both models were seen to vary significantly with rotational speed. For the translational model, the open-loop damping of the flexible modes varies most strongly with rotational speed, with the forward flexible mode becoming unstable at super-flexible rotational speeds. These open-loop instabilities will place minimum bandwidth and gain requirements on stabilizing controllers. In conjunction with the movement of these open-loop poles into the right-half-plane (RHP), the transmission zeros associated with the forward flexible mode move into the RHP, becoming non-minimum phase transmission zeros. These non-minimum phase transmission zeros will place corresponding maximum bandwidth and gain restrictions on stabilizing output-feedback compensators.

The angular plant is also a strong function of rotational speed, with the frequencies of some of the open-loop poles being proportional to rotational speed. The open-loop singularities of the angular model vary more strongly with rotational speed than do the translational singularities. The control of the angular model over a wide speed range with a fixed-gain controller should, therefore, be more difficult than for the translational mo The open-loop singularities of the angular model, howe r, all remain in the Left-hand Plane (LHP) at all speeds, which eliminates the controller restrictions on bandwidth that are faced with the translational model.

The stability properties of the closed-loop translational and angular models are one of the major results of this study. The closed-loop stability properties were analyzed using recently developed control analysis tools for systems described by complex coefficient differential equations [Johnson 1987]. These include closed-loop eigenvalue locations of the complex representations and the "complex" SISO Nyquist gain and phase margins. In addition to these measures of stability and stability robustness, the research also explicitly determined the stability robustness to variation in plant speed and variation in spoke damping and stiffness.

A variety of controllers were investigated for both the translational and angular models [Johnson 1987]. These include:

1) Variable gain, full state feedback, linear quadratic regulators

2) Fixed gain, full state feedback, linear quadratic regulators

3) Fixed gain, output feedback compensators design using linear quadratic regulator and Kalman filter algorithms, the so called "Model Based Compensators" [Doyle 1981]

4) Fixed gain, output feedback, lead-lag compensators

Chapter 6 of this report will present representative controllers for the two models, a fixed-gain, model-based-compensator (MBC) for the translational model and a lead-lag compensator for the angular model. A more detailed description of the various controllers can be found in Appendix B and a more extensive presentation of the closed-loop results can be found in [Johnson 1987].

5. CONTROLLER EXAMPLES

5.1 Closed-Loop Translational Example

The closed loop translational example that will be presented is a fixed-gain, output-feedback, model-based-compensator. This particular controller features a closed-loop bandwidth (rigid-body cross-over) slightly below the flexible-mode frequency. The compensator was designed for a rotational speed of 1000 rad/sec. Recall that at this super-flexible rotational speed the open-loop system is unstable.

As for the open-loop plant, the closed-loop plant can be described by the complex coefficient transfer function (CCTF), a single-input, single-output transfer function with complex coefficients. For this compensator, the CCTF of the compensator is shown in figure 36. The forward whirl transfer function (positive frequencies) is given by the solid curve and the backward whirl transfer function (negative frequencies) by the dashed curve. Note that these transfer functions consist of a lead-lag with a notch at the flexible mode frequency. As can be seen in figure 36b, the forward whirl transfer function features a right-hand-plane (RHP) transmission zero.

The Nyquist plot of the loop transfer function, plant plus compensator, is shown in figure 37. For this figure, the plant rotational speed was set equal to the design rotational speed of 1000 rad/sec. Note that the Nyquist plot encircles the -1 point once in a clockwise direction as required for closed-loop stability with an open-loop unstable plant. From this plot, the phase margin is seen to be approximately 55° at the worst cross-over. The upward gain margin is approximately 20db and the downward gain margin is approximately 14 db.

At this rotational speed, the closed-loop eigenvalues of the plant are given in Table XIII below. These closed-loop eigenvalues have been divided into those associated with the LQR loop and those associated with the Kalman Filter loop.

TABLE XIII. CLOSED-LOOP EIGENVALUES FOR THE TRANSLATIONAL CASE

LQR Closed-Loop Eigenvalues	Kalman Filter Closed-Loop Eigenvalues
-120 + j120	-10 + j497
-120 - j120	-12 - j497
-18 + j680	-1600 + j680
-20 - j680	-1600 - j680

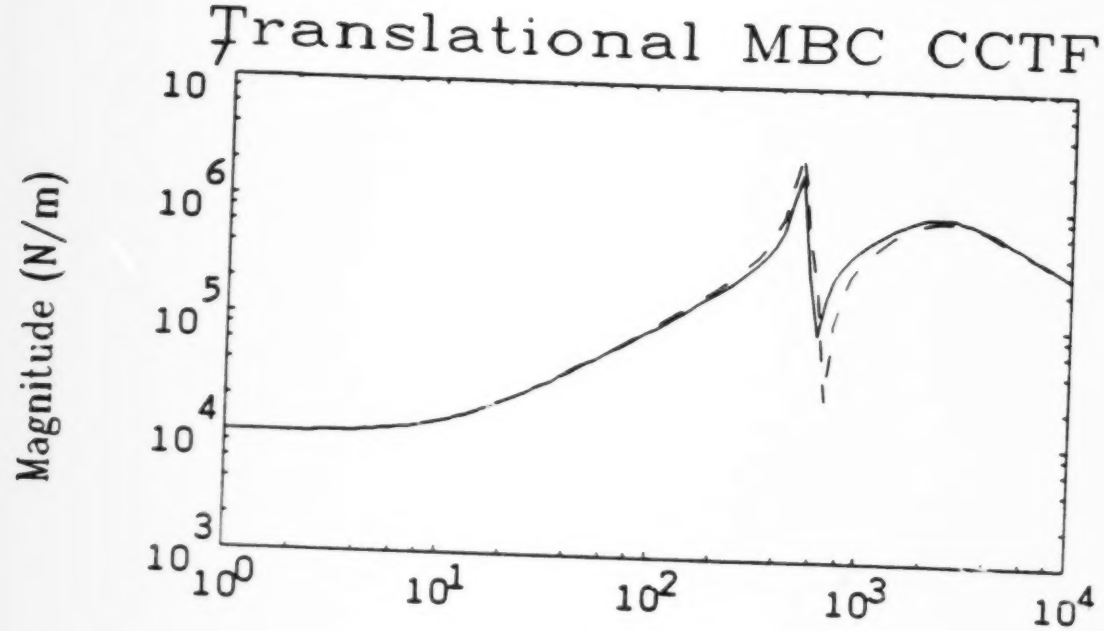

a) Magnitude

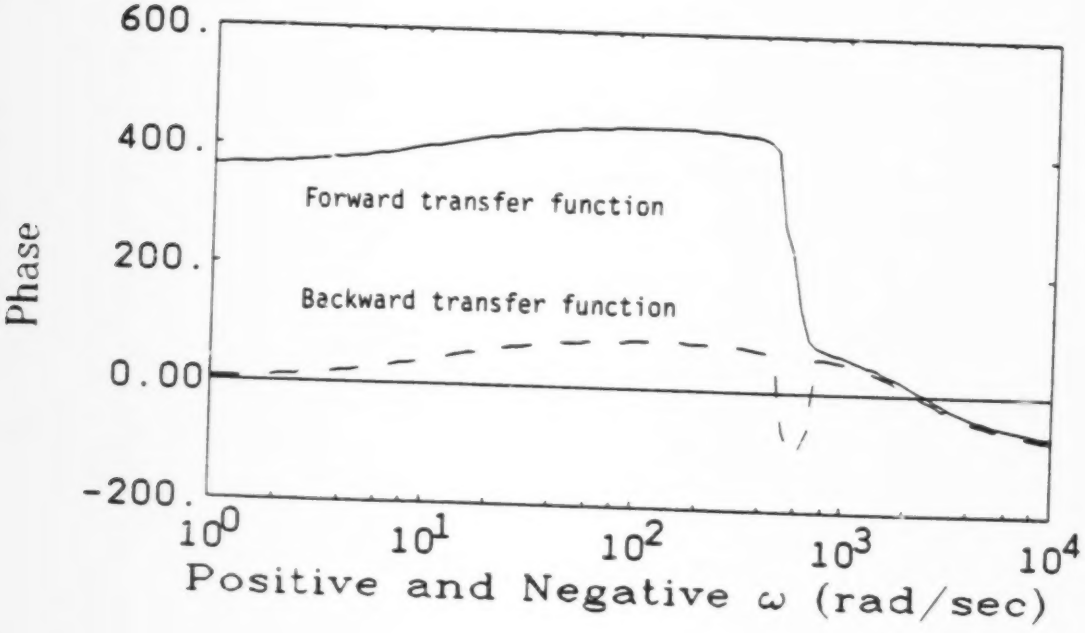

b) Phase

Figure 36. Bode Plot of Translational MBC: Medium-bandwidth Controller with Low-frequency Loop Recovery, 1000 rad/sec Rotational Speed

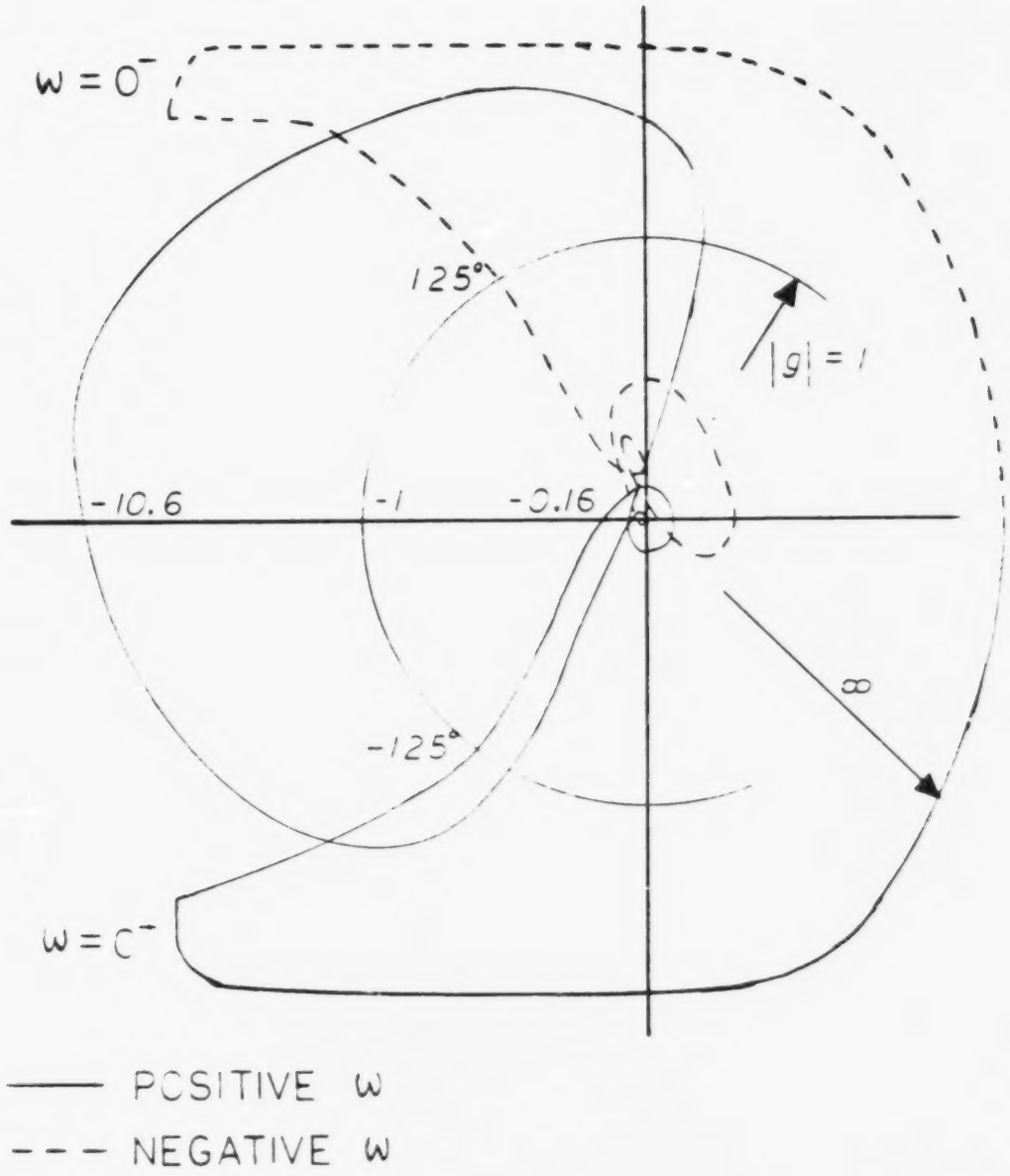

Figure 37. Nyquist Plot of Translational MBC & Plant Loop Transfer Functions: Medium-bandwidth Controller with Low-frequency Loop Recovery, 1000 rad/sec Rotational Speed.

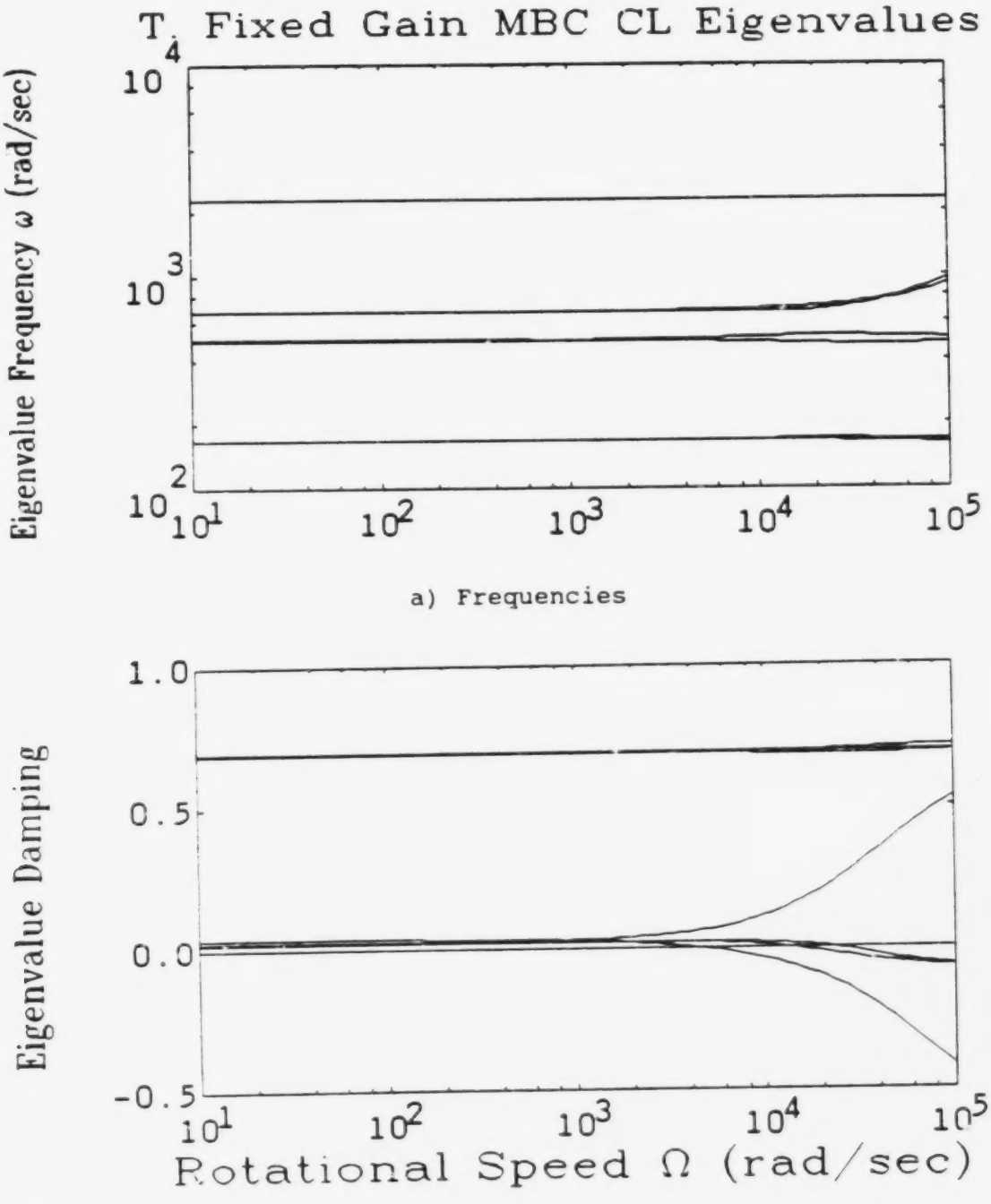

Figure 38. Translational Closed-loop Pole Locations versus Rotational Speed: Medium-bandwidth MBC designed at a Rotational Speed of 1000 rad/sec.

The two low-frequency LQR poles are associated with the cross-over frequency of the system and are placed in well damped positions. The poles associated with the flexible-modes have been placed in stable, lightly damped positions.

The results presented above are for a fixed rotational speed of 1000 rad/sec, the design rotational speed of the MBC. Figure 38, in contrast, presents the closed-loop eigenvalue frequencies and damping when the plant rotational speed is allowed to vary. In this figure, the model-based-compensator has been fixed and the plant varies because of its dependence on rotational speed. Note that the closed-loop system remains stable until a rotational speed of greater than 4000 rad/sec. This is outside the possible speed range of the ACCESS system and significantly greater than the rotational speed of 670 rad/sec at which the open-loop translational system becomes unstable.

5.2 Closed-Loop Angular Example

The closed-loop angular example that will be presented in this section is a simple fixed-gain, lead-lag compensator. This compensator is designed to have a rigid-body cross-over of approximately 200 rad/sec, which is below the flexible mode frequency of 1200 rad/sec, when the system is not spinning. The lead in the compensator is placed about a half decade below the desired zero-speed cross-over frequency and the lag about a half a decade above the flexible mode frequency. This can be seen in figure 39, the Bode magnitude and phase plots for this lead-lag compensator.

The loop gain for this compensator is shown in figure 40 for a plant rotational speed of 200 rad/sec. Again, the forward whirl transfer function is given by the solid curve and the backward whirl transfer function by the dashed curve. Note that the low-frequency cross-over has been significantly reduced from the desired zero-speed value because of the reduction in plant gain that occurs with increasing rotational speed. Because of this reduction in low-frequency gain, the negative phase margin has been reduced to approximately 30° from the zero speed value of greater than 60°. The positive phase margin, however, remains at about 60°. The upward and downward gain margins are formally infinite, reflecting the open-loop stable nature of the angular plant.

The closed-loop eigenvalues for this speed are given in Table XIV. The first two eigenvalues correspond to the forward and backward rigid-body modes. Note that because of gyroscopic effects, these two eigenvalues have split in frequency, with the forward whirl mode increasing in frequency compared to the backward whirl mode. They are both well damped, however. The next two eigenvalues are associated with the flexible modes of the system. Again, the forward and backward modes have split

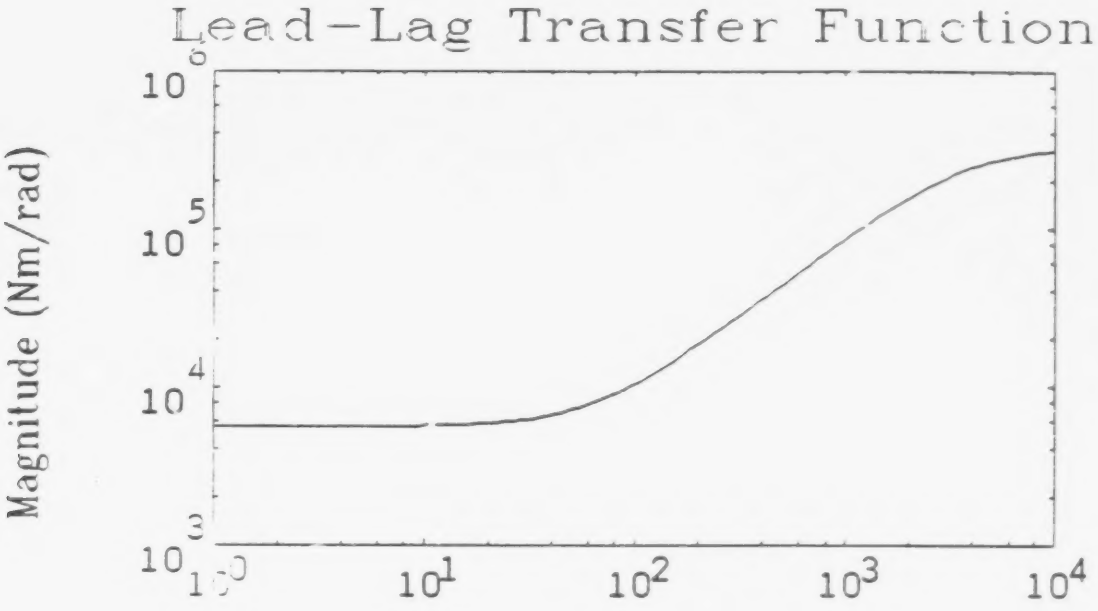

a) Magnitude

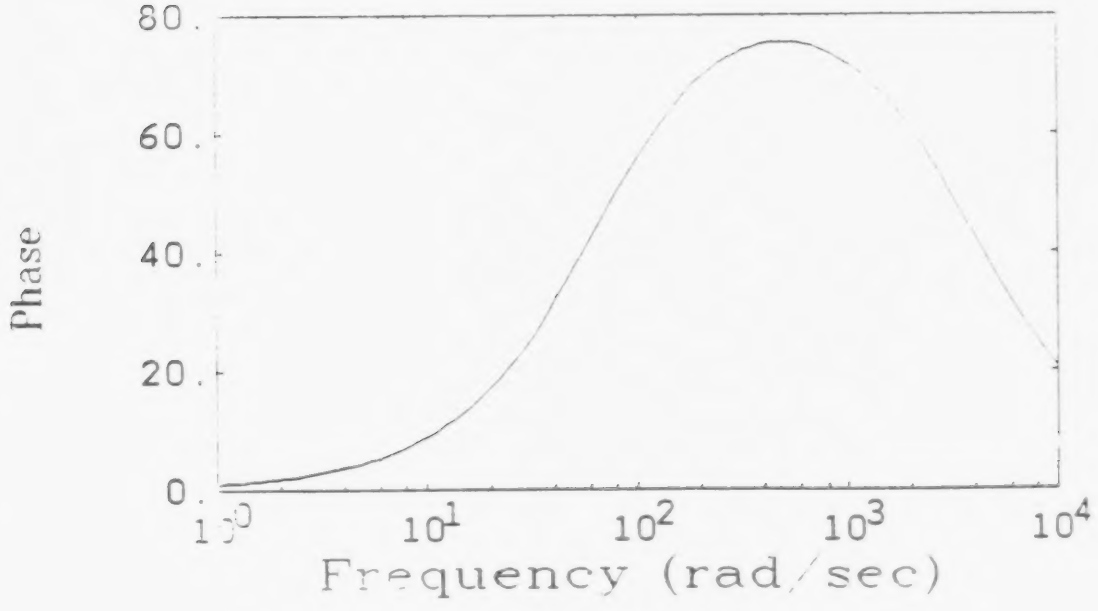

b) Phase

Figure 39. Bode Plot of the Lead-lag Compensator for the Angular model.

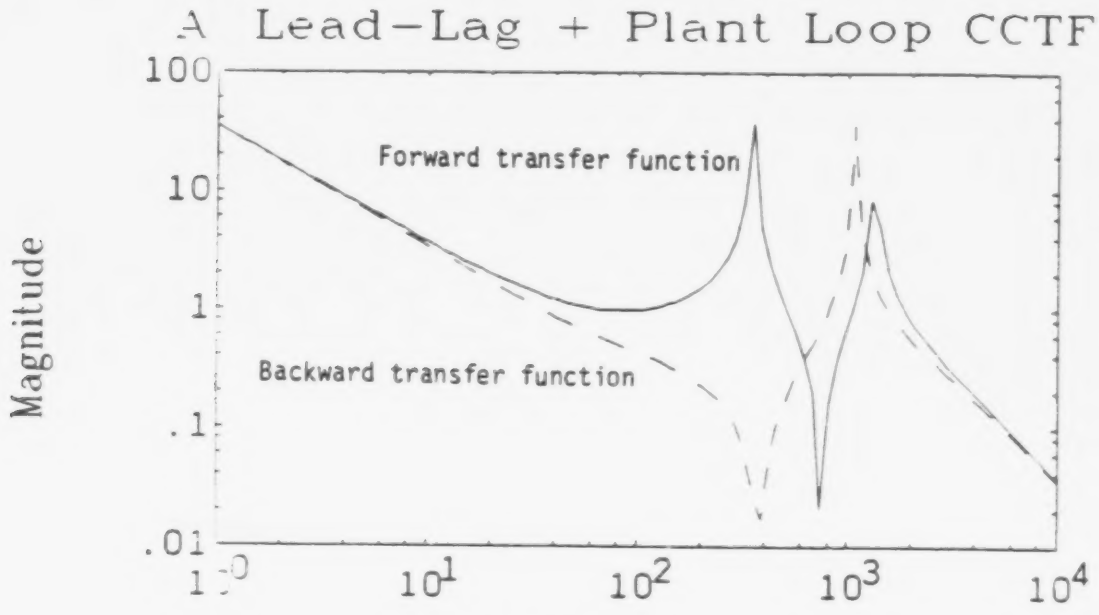

a) Magnitude

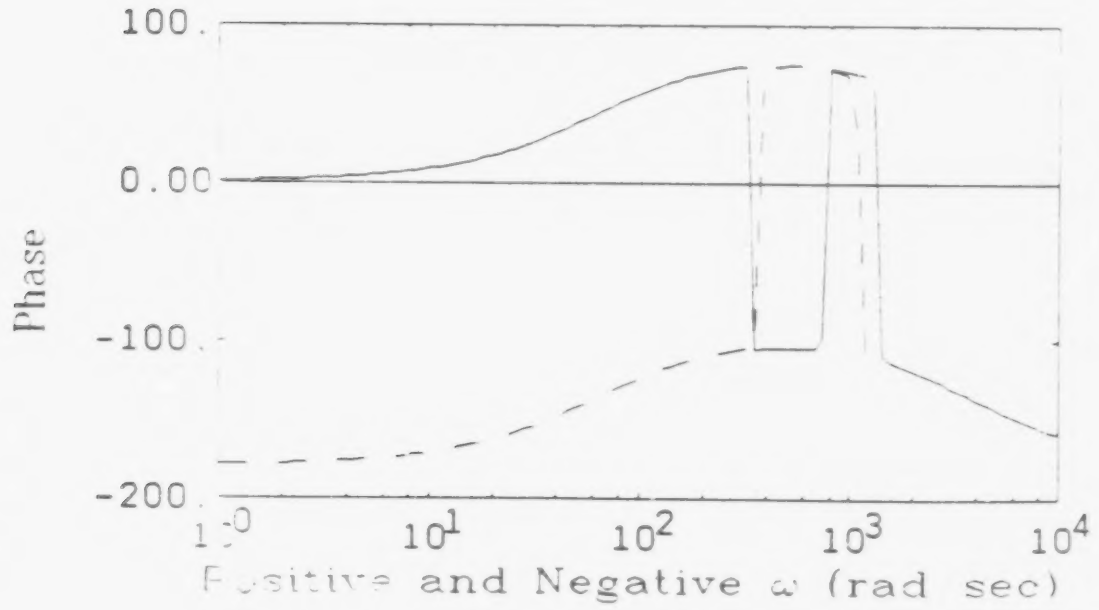

b) Phase

Figure 40. Bode Plot of the Angular Loop Transfer Function: Lead-lag Compensator at a Rotational Speed of 200 rad/sec.

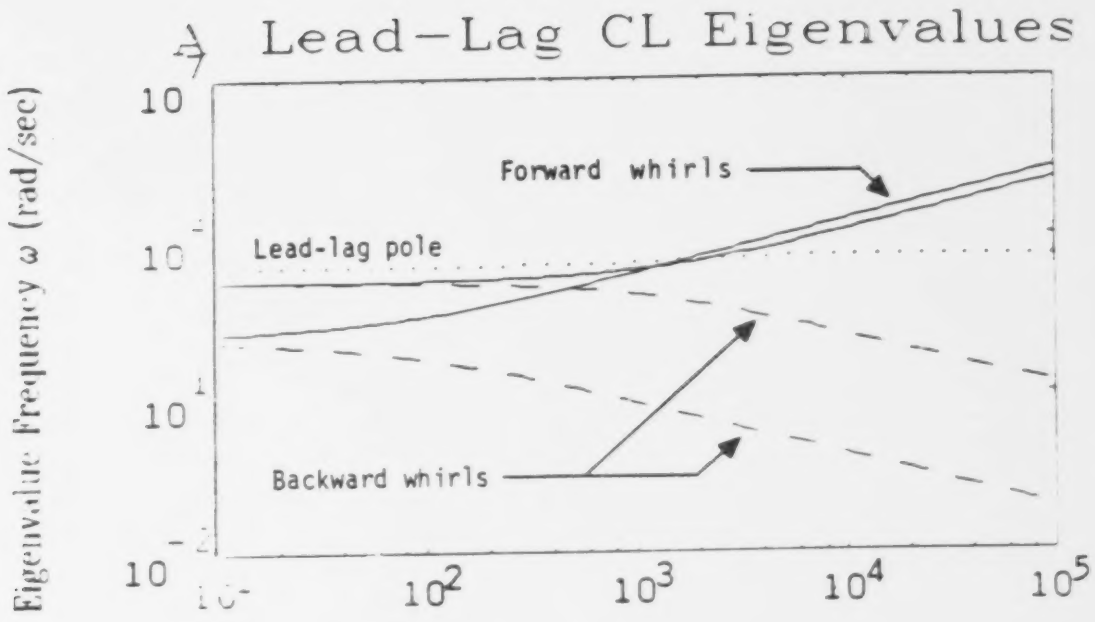

a) Frequency

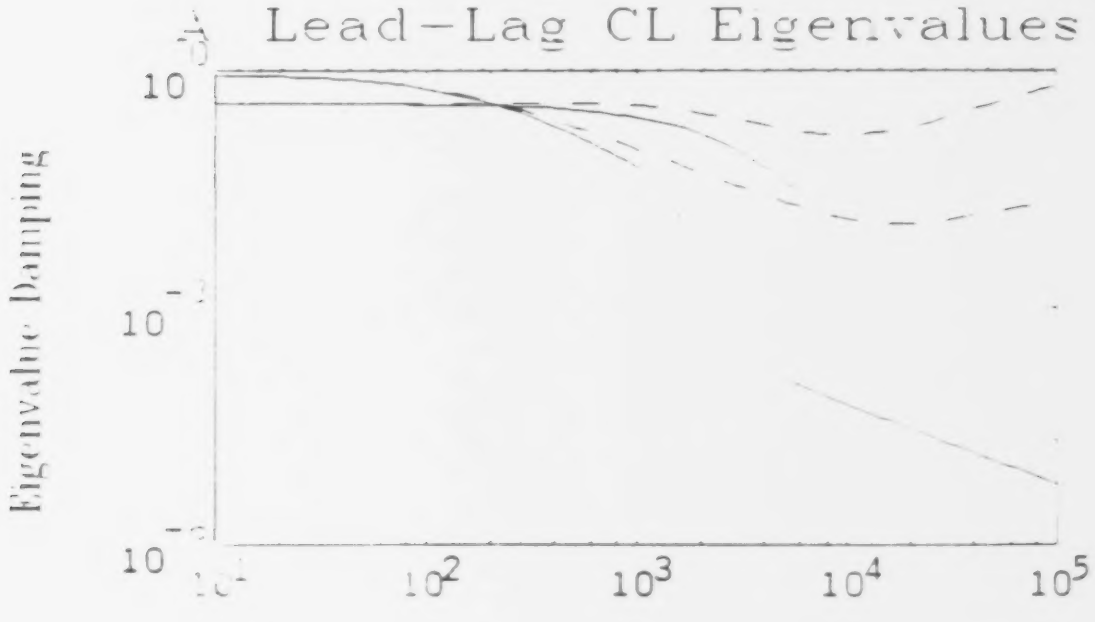

b) Damping

Figure 41. Angular Closed-loop Eigenvalues versus Rotational Speed: Lead-lag Compensator.

in frequency. These modes are significantly better damped than their open-loop locations. The last eigenvalue corresponds to the lead of the compensator.

TABLE XIV. ANGULAR CLOSED-LOOP EIGENVALUES

Eigenvalue Location
-177 + j247
-27 - j37
-532 - j1338
-489 + j1178
-2582 - j69

In contrast to the translational example, the angular model under lead-lag compensation remains stable at all rotational speeds. This can be seen in figure 41, a plot of the closed-loop eigenvalues versus rotational speed. The eigenvalue frequencies are shown in figure 41a where the forward whirl modes (solid curves), backward whirl modes (dashed curves), and compensator lag pole (dotted curve) can clearly be seen. The damping of the closed-loop eigenvalues is shown in figure 41b, where the system is seen to remain stable at all rotational speeds. At super-flexible rotational speeds, the damping of the forward whirl modes (solid curves) decreases significantly with increasing rotational speed. This is primarily caused by the increased frequency of these modes with increasing speed.

CONCLUSIONS

This report has presented the results of an investigation of the control an advanced Annular Momentum Control Device (AMCD), the AMCD Combined Control Energy Storage System (ACCESS). This system, which consists of high-speed, magnetically suspended flywheels, presents a variety of control problems because of the open-loop unstable nature of its operation at high rotational speeds and the variation of its dynamics as the rotational speed is changed. This research has included the development of a dynamic model of the system and the design of stabilizing controllers.

The ACCESS system was modelled as a two rigid-bodies, the hub and flywheel, connected by a damped, elastic structure, the spoke system. The system is controlled by a Lorentz-force suspension that applies force and torque to the hub. The bearing force and torque are controlled by a controller having access to measurements of hub position and orientation. This model, therefore, includes the effects of rotor flexibility, internal damping, and gyroscopic motion.

The system dynamics of concern to the bearing controller, which are the translational or radial motion and the angular or tipping motion of the rotor masses, are shown to decouple into separate translational and angular models. Each of these models describes a two-input, two-output system relating hub translational position to bearing force for the translational model and hub angular orientation to bearing torque for the angular model. These models exhibit "block-symmetric" structure because of the assumed rotational symmetry. Because of this block-symmetric structure, complex notation is used, providing a compact and powerful method of expressing the dynamics of these symmetric systems.

These complex coefficient system equations are used to describe both the translational and angular models. Over the operational speed range of the ACCESS system, these models are both controllable through the application of bearing force and torque and observable through measurements of hub position and orientation. The open-loop behavior of both models are seen to vary significantly with rotational speed. For the translational model, the open-loop damping of the flexible modes is shown to vary most strongly with rotational speed, with the forward flexible mode becoming unstable at super-flexible rotational speeds. In conjunction with the movement of the open-loop poles into the right half plane (RHP), the transmission zeros associated with these modes also move into the RHP, becoming nonminimum phase transmission zeros.

The angular plant is also shown to be a strong function of rotational speed, with the frequencies of some of the open-loop

poles proportional to rotational speed. Although the open-loop singularities of the angular model vary more strongly with rotational speed than for the translational model, all of the angular singularities remain in the left half plane for all rotational speeds, in contrast to the translational model.

Various feedback controllers were investigated for both the translational and angular models. These include variable-gain, full-state feedback controllers based on linear-quadratic regulators (LQR); fixed-gain, full-state feedback LQR's; output-feedback, model-based-compensators (MBC) designed using fixed-gain Kalman filters as state estimators in conjunction with fixed-gain LQR's; and simple output-feedback, lead-lag compensators. Two representative examples of these controllers were presented, a model-based-compensator for the translational model and a lead-lag compensator for the angular model. The conclusions presented below are based on the research reported here and on a more extensive variety of controllers, which can be found in Johnson [1987].

Using the variable-gain, full-state feedback LQR, the effect of different gains on closed-loop stability was investigated. The use of cross-axis feedback gains, which are gains relating the force along one axis to measurements of rotor positions or velocities along the perpendicular axis, was shown to have the opposite effect on the forward and backward whirl dynamics. These cross-axis gains, therefore, can be used to control differentially the forward and backward whirl dynamics. The parallel gains, in contrast, have the same effect on the forward and backward whirl dynamics.

The use of output-feedback compensators, both MBC's and simple lead-lag compensators, was extensively studied for the translational model. The various compensator designs were compared on the basis of nominal stability, stability robustness to speed variation, and stability robustness to variations in the spoke characteristics. For both model-based and lead-lag compensators, designs with cross-over frequencies near the flexible mode frequency generally have the best performance. In particular, the low- and high-bandwidth designs exhibited poor stability and stability robustness. In fact, the open-loop, RHP poles and transmission zeros exhibited by the translational model place minimum and maximum bandwidth constraints on stabilizing controllers as can be seen by the maximum and minimum constraints of figure 37.

Similar controllers were investigated for the angular model. Fixed-gain linear quadratic controllers, either full-state feedback LQR's or output feedback MBC's were found to have only limited stable speed ranges. This is caused by the extensive use of cross-axis feedback in these controllers. In

contrast, lead-lag compensators acting only on the parallel feedback paths stabilize the system at all rotational speeds.

For both models, simple lead-lag compensators acting on parallel measurements provide good stability and stability robustness over a wide speed range. For the translational model, the gain of the compensator and frequencies of the compensator pole and zero are constrained by stability requirements, as mentioned above. For the angular model, the compensator must provide lead over a large enough frequency range to allow for the variation in cross-over frequency that occurs because of gyroscopic effects.

BIBLIOGRAPHY

Anderson, W. and Keckler, C. [1973], **An Integrated Power/Attitude Control System (IPACS) for Space Vehicle Application**, presented at the Fifth IFAC Symposium on Automatic Control in Space, Genoa, Italy.

Anderson, W. and Groom, N. [1975], **The Annular Momentum Control Device (AMCD) and Potential Applications**, NASA TN D-7866, 1975.

Anderson, W., Groom, N., and Wolley, C. [1979], **Annular Suspension and Pointing System**, AIAA Journal of Guidance and Control 2, No 5, (Sept-Oct 1979).

Basore, P. [1982], **Self-stabilizing Magnetic Bearings for Flywheels**, PhD Thesis, Massachusetts Institute of Technology, Cambridge, Massachusetts, 1982.

Bleuler, H. [1984], **Decentralized Control of Magnetic Rotor Bearing Systems**, Doctor of Technical Sciences Dissertation, Swiss Federal Institute of Technology, Zurich.

Diamarogonas, A.D., and Paipetis, S.A., **Analytical Methods in Rotor Dynamics**, London: Applied Science Publishers, 1983.

Downer, J. [1980], **Analysis of a Single Axis Magnetic Suspension System**, S.M. Thesis, Massachusetts Institute of Technology, Cambridge, Massachusetts, January 1980.

Downer, J. [1986], **Design of Large Angle, Magnetic Suspensions**, ScD Thesis, Massachusetts Institute of Technology, Cambridge, Massachusetts, June 1986.

Doyle, J. and Stein, G., **Multi-variable Feedback Design: Concepts for a Classical/Modern Synthesis**, IEEE Trans. on Automatic Control AC-26, No 1, (February 1981).

Eisenhaure, D., Oberbeck, G. and Downer, J. [1977], **Development of a Low-loss Flywheel Magnetic Bearing**, 14th Intersociety Energy Conversion Engineering Conference Proceedings, American Chemical Society, 1, 1977.

Eisenhaure, D., Downer, J., Bliamptis, T., and Hendrie, S. [1984a], **A Combined Attitude, Reference, and Energy Storage System for Satellite Applications**, Presented at AIAA 22nd Aerospace Sciences Meeting, Reno, Nevada: January 9-12, 1984.

Eisenhaure, D., Downer, J., Hockney R., O'Dea, S., [1984b], **Multi-variable Function Utilization of Inertial Energy Storage Wheels in Spacecraft Applications**, In AIAA Guidance and Control Conference Proceedings, Seattle, Washington: August.

Foley, T. [1986], **Design of a Flexible Flywheel Support Structure for a Combined Energy Storage/Attitude Control System**, S.M. Thesis, Massachusetts Institute of Technology, Cambridge, Massachusetts, June 1986.

Groom, N. and Terray, D. [1978], **Evaluation of a Laboratory Test Model Annular Momentum Control Device**, NASA TP-1142.

Groom, N. and Miller, J. [1981], **A Microprocessor-Based Table Look-up Approach for Magnetic Bearing Linearization**, NASA TP-1838 (1981).

Groom, N. [1984], **Overview of Magnetic Bearing Control and Linearization Approaches for Annular Magnetically Suspended Devices.** An Assessment of Integrated Flywheel System Technology, NASA CP-2346, pp.297-306.

Gunter, E.J., **Dynamic Stability of Rotor-Bearing Systems**, Washington, D.C.: NASA, 1966.

Hubbard M, and McDonald, P. [1980], **Feedback Control Systems for Flywheel Radial Instabilities.** 1980 Flywheel Technology Symposium, Rep. No. CONF-801022, Dep. Energy, 1980.

Johnson, B. [1985a], **Active Control of a Flexible Rotor**, S.M. Thesis, Massachusetts Institute of Technology, Cambridge, Massachusetts, January 1985.

Johnson, B., Eisenhaure, D. and Paynter, H. [1985b], **Control of Flexible Rotor Systems**, Proceedings of the 20th Intersociety Energy Conversion Engineering Conference, Miami Beach, Florida: August 18-23, 1985.

Johnson, B. [1986], **Active Control of a Flexible, Two-Mass Rotor System: The Use of Complex Notation**, ScD Thesis, Massachusetts Institute of Technology, Cambridge, Massachusetts, February 1987.

Kaya, F, and Roberts, J. [1984], **Optimum Vibration Control of Flexible Transmission Shafts**, Proceedings of the Third International Conference on Vibrations in Rotating Machinery, University of York, England: September 11-13, 1984.

Keckler, C. and Jacobs, K. [1974], **A Spacecraft Integrated Power/Attitude Control System**, Proceedings of the Ninth Intersociety Energy Conversion Engineering Conference, San Francisco, CA.

Kennel, H. [1970], **A Control Law for Double-Gimballed Control Moment Gyros Used for Space Vehicle Attitude Control**, NASA TM X-64536.

Larkin, L. [1985], **Design and Optimization of a High Efficiency Motor/Generator for a Satellite Energy Storage System**, S.M. Thesis Massachusetts Institute of Technology.

Loewy, R.G., and Piarulli, V.J., **Dynamics of Rotating Shafts**, The Shock and Vibration Monograph Series SVM-4, published by The Shock and Vibration Information Center, Naval Research Laboratory, Washington, D.C., 1969.

McDonald, P., and Hubbard, M [1985], **An Actively Controlled Pendulous Flywheel with Magnetic Bearing**, Proceedings of the 20th Intersociety Energy Conversion Engineering Conference, Miami Beach, Florida: August 18-23, 1985.

Muramaki, C. [1982], **Development Activities on Magnetic Bearings for Space Use in National Aerospace Laboratory of Japan**, Proceedings of the Sixth International Workshop on Rare Earth Cobalt Permanent Magnets, Technical University of Vienna.

Nikolajsen, J., Holmes, R., and Gondhalekar, V. [1979], **Investigation of an Electromagnetic Damper for Vibration Control of a Transmission Shaft**, Proceedings of the Institution of Mechanical Engineers. 193, (1979).

Notti, J., Cormack III, A. and Schmill, W. [1974], **Integrated Power/Attitude Control System (IPACS) Study.** Volume 2 - Conceptual Designs. NASA CR-2384.

O'Dea, S, Burdick, P., Downer, J. and Eisenhaure, D. [1985], **Design and Development of a High Efficiency Effector for the Control of Attitude and Power in Space Systems**, Proceedings of the 20th Intersociety Energy Conversion Engineering Conference, Miami Beach, Florida: August 19-23, 1985.

Oglevie, R., and Eisenhaure, D. [1985], **Advanced Integrated Power and Attitude Control System (IPACS) Study.** NASA CR-3912.

Rao, J.S., **Rotor Dynamics**, New York: J. Wiley and Sons, 1983.

Roberson, R. [1958], **Principles of Inertial Control of Satellite Attitude**, Proceedings of the 9th International Congress of Aeronautics, Amsterdam, Holland, August 1958.

Robinson, A. [1984], **European Development Experience on Energy Storage Wheels for Space.** An Assessment of Integrated Flywheel System Technology. NASA CP-2346, pp. 65-73.

Rotors, H. [1941], **Electromagnetic Devices**, John Wiley & Sons, Inc., 1941.

Sabnis A., Dendy, J. and Schmidt, F. [1975], **A Magnetically Suspended Large Momentum Wheel**, Journal of Spacecraft and Rockets, 12 (July 1975).

Salm J, and Schweitzer, G. [1984], **Modelling and Control of a Flexible Rotor with Magnetic Bearings**, Proceedings of the Third International Conference on Vibrations in Rotating Machinery, University of York, England: September 11-13, 1984.

Schweitzer, G. [1974], **Stabilization of Self-Excited Rotor Vibrations by an Active Damper**. In **Dynamics of Rotors**, ed., FI Niordson, Springer-Verlag, New York: 1975. (From 1974 Proceedings, see Niordson).

Sindlinger R. [1976], **Magnetic Bearing Momentum Wheels with Vernier Gimballing Capability for 3-Axis Active Attitude Control and Energy Storage**, Proceedings of IFAC Symposium on Attitude Control in Space, Rotach-Egern, May.

Sindlinger R. [1977], **Magnetic Bearing Momentum Wheels with Vernier Gimballing Capability for 3-Axis Active Attitude Control and Energy Storage**, In Proceedings of the First International Conference on Attitude and Orbit Control Systems, Noordwijk, Netherlands: October 3-6, 1977.

Stanway, R., and O'Reilly, J. [1984], **State-Variable Feedback Control of Rotor-Bearing Suspension System**, Proceedings of the Third International Conference on Vibrations in Rotating Machinery, University of York, England, September 11-13, 1984.

Stocking, G. [1984], **Magnetically Suspended Reaction Wheel Assembly.** An Assessment of Integrated Flywheel System Technology, NASA CP-2346, pp. 265-279.

Teldix GmbH [1976], **Data Sheets for Space Components**, Heidelberg, West Germany: May 1976.

Tondl, A., **Some Problems of Rotor Dynamics**, Prague: Publishing House of the Czechoslavak Academy of Sciences, 1965.

Ulbrich, H., and Anton, E. [1984], **Theory and Application of Magnetic Bearings with Integrated Displacement and Velocity Sensors**, Proceedings of the Third International Conference on Vibrations in Rotating Machinery, University of York, England: September 11-13, 1984.

Weinberg, M. [1982], **Momentum Exchange Effectors for Space Applications**, P-1532, The Charles Stark Draper Laboratory, Inc., Cambridge, MA.

Wertz, J. [1978], Spacecraft Attitude Determination and Control, P. Reidel Publishing Co.

APPENDIX A

CARES MODEL DEVELOPMENT

This appendix develops an analytical model of the translational and angular (tilt) dynamics of the laboratory ACCES system. The ACCES system will be modelled as two rigid body masses, the hub and the flywheel, connected by a damped elastic structure, the spoke structure. The bearing forces and torques acting on the flywheel are controlled by a dynamic system, the controller, having access to hub position and orientation information. The model developed in this chapter will be used for the analysis and design of the controlier system.

A.1 Model Development

The development of rotor dynamic models is an area of extensive previous research. Recent books by [Rao 1983] and [Diamarogonas 1983] as well as earlier works by [Tondl 1965], [Gunter 1966], and [Loewy 1969] provide various derivations and models. With the abundance of rotor dynamic models available, the development in this thesis of another model may seem unnecessary. Indeed, many models of actively controlled rotor systems are conventional rotor dynamic models with more general bearing forces used in place of the conventional bearing models. The emphasis of the development in this thesis, however, is modelling, in a form suitable for controller analysis and design, the unique features of actively controlled rotor systems. The most important of these features is that the measurements of rotor position and orientation need not be colocated with actuation. Restated, the bearings (actuators) and measurement system (sensors) are not necessarily interacting with the same part of the rotor. In conventionally supported rotors, in contrast, the force produced at each bearing is a function of the time history of the position of the rotor at that bearing.

The development used here will start by obtaining the relations between applied force and torque and the resulting position and orientation of each rigid body mass. Small angular motions will be assumed, leading to linearized models. The force and torque produced by the spoke structure will then be related to the relative positions and orientations of the rigid bodies. These relations describing the spoke structure will also be assumed linear. The bearing force and torque and measurement system descriptions will then be added to complete the system model.

The approach just described will be used to develop a non-synchronous model, one that assumes perfect inertial and spoke geometries, analogous to a perfectly balanced conventional rotor system. A similar model that incorporates synchronous effects

can be found in [Johnson 1987]. This synchronous model adds the effects caused by non-alignment of elastic and inertial centers at each rigid body mass. This is analogous to a conventional rotordynamic model that includes the effect of mass unbalances.

Coordinate Systems

Three coordinate system will be employed to provide a sufficient frame work for the development of the CARES dynamics. The first is an fixed, inertial coordinate system given by the (X,Y,S) axes with unit vectors ($\underline{i}$, $\underline{j}$, $\underline{k}$). This coordinate system is important for two reasons. The first reason is that the equations of motion, Newton's First Law and the Law of the Moment of Momentum, require time derivatives to be taken with respect to an inertial coordinate system. The second reason is that the magnetic bearing and measurement system are assumed stationary in this coordinate system, meaning that the forces and torques applied by the magnetic bearing and positions and rotations measured by the measurement system are most naturally expressed in this frame.

A second type of coordinate system will be used to describe the position and orientation of the spin axis of each rigid body. These coordinate systems, called rotating coordinate systems, are attached to the rigid bodies but not spinning with them. Consider the coordinate system describing the position and orientation of one of the rigid body masses, as shown in figure A.1.1. This reference system is given by the $(X^{(r)},Y^{(r)},S^{(r)})$ axes with unit vectors ($\underline{i}^{(r)}$, $\underline{j}^{(r)}$, $\underline{k}^{(r)}$). The $S^{(r)}$-axis of this coordinate system is a principal axis of inertia of the rigid body and the origin of the coordinate system is coincident with the center of mass of the rigid body. The $S^{(r)}$ axis will be called the axial inertial axis of the rigid body.

Relative to this rotating coordinate system, the rigid body will have angular velocity $\Omega_S\underline{k}^{(r)}$. In other words, seen from the rotating coordinate system, the rigid body spins about the $S^{(r)}$-axis with rotational speed Ω_S. This rotating coordinate system will have the useful property that the moments of inertia of the rigid body are not functions of time when they are expressed in this coordinate system.

The rotating coordinate system $(X^{(r)},Y^{(r)},S^{(r)})$ is related to the fixed coordinate system (X,Y,S) by the following rotations and translations. The fixed (X,Y,S) coordinate system is rotated by the angle ϕ about the X axis to a new location given by the coordinate system (x",y",s"). This system can be rotated to a coordinate system (x',y',s') that is parallel to the rotating system $(X^{(r)},Y^{(r)},S^{(r)})$ by a rotation of θ about the y" axis. These rotations are shown in figures A.1.2a and A.1.2b. This intermediate (x',y',s') coordinate system can be transformed into the rotating coordinate system $(X^{(r)},Y^{(r)},S^{(r)})$ by a translation

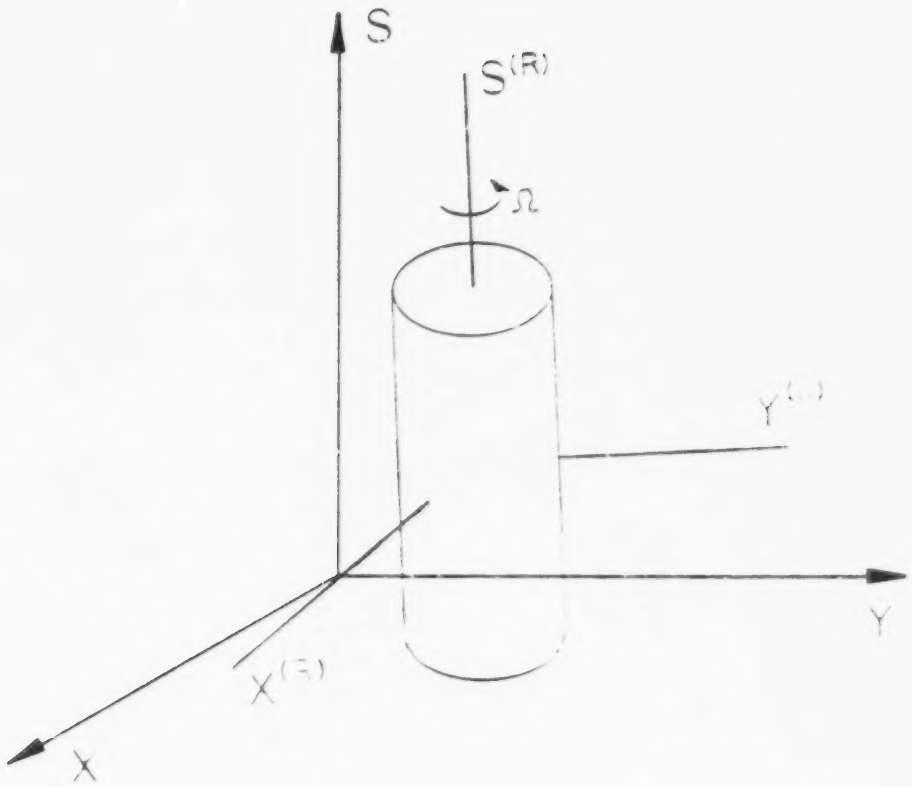

Rigid body spins with angular velocity Ω relative to the rotating $^{(R)}$ coordinate system.

Figure A.1.1. Rotating Coordinate System

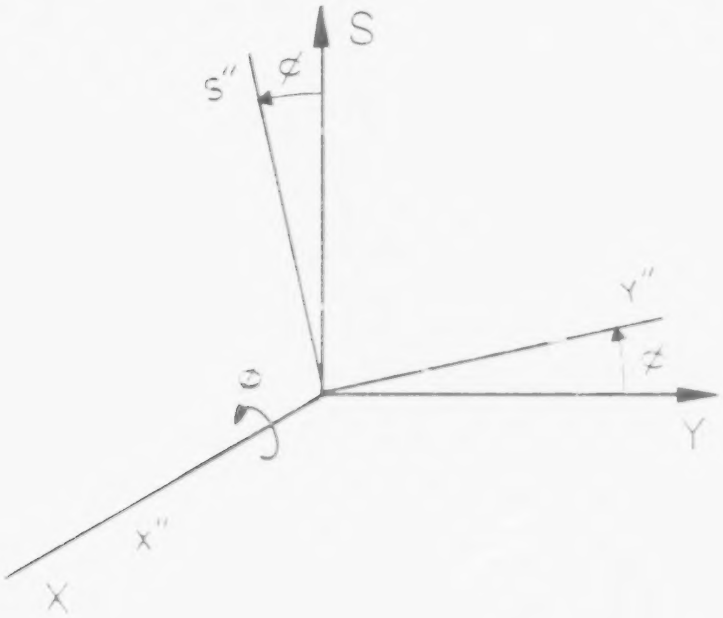

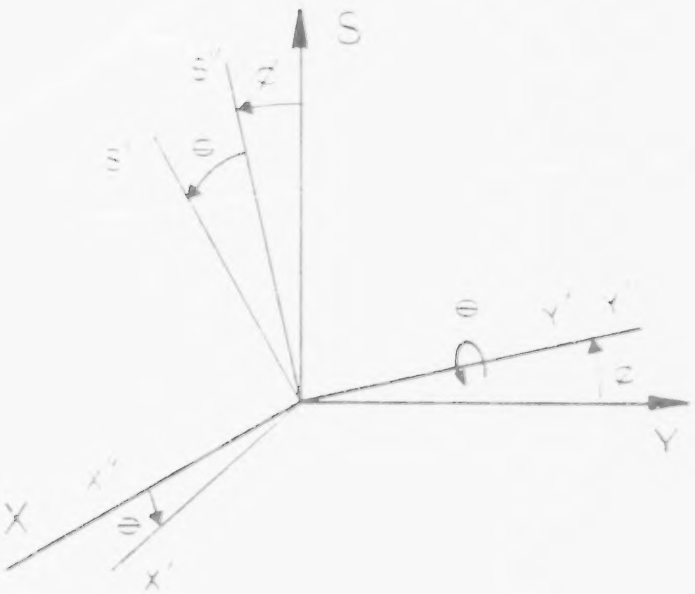

Figure A.1.2. Relation of Rotating Coordinate System to Fixed Coordinate System: Relative Angular Orientation

of the origin to a point (x,y,z) in the fixed (X-Y-S plane, as shown in Figure A.1.3. Note that while the rotating, or principal-axis-aligned, coordinate system does not spin with the rigid-body, the coordinate system will still rotate if either angles ϕ or θ change with time.

The third coordinate system is spinning about the S-axis of the fixed coordinate system with an angular velocity Ð, the nominal axial spin of the rigid bodies. This spinning coordinate system is given by the $(X^{(S)},Y^{(S)},Z)$ axes with unit vectors $(i^{(S)},j^{(S)},k)$. The spinning coordinate system is related to the inertial coordinate system by a rotation of Ðt about the S-axis, as can be seen in figure A.1.4. This will prove to be a useful coordinate system for describing the torques and forces produced by the spoke structure. Relative to this coordinate system, the spoke structure will appear stationary if the system is spinning at equilibrium.

Rigid-Body Motion

The motion of the rigid bodies is governed by Newton's First Law for translational motior and the law of moment of momentum for rotational motion. These are

$$\underline{M}_o = \frac{d\underline{H}_o}{dt} \qquad (A.1.1)$$

and

$$\underline{F} = m\frac{d\underline{v}_o}{dt} \qquad (A.1.2)$$

where

$\underline{M}_o$ = applied torque measured in the fixed reference system.

$\frac{d}{dt}$ = time derivative in the fixed reference system

$\underline{H}_o$ = absolute (referenced to the fixed system) angular momentum of the rigid body with respect to the center of mass o

$\underline{F}$ = applied force measured in the fixed reference system.

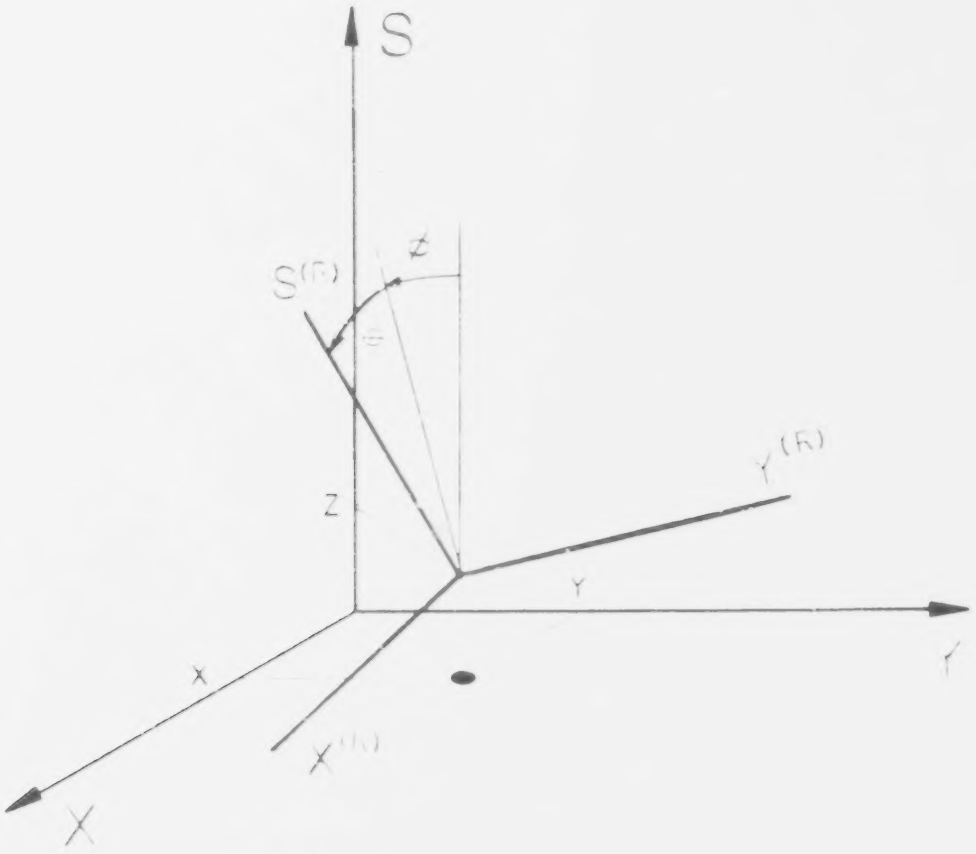

Figure A.1.3 Relation of Rotating Coordinate System to Fixed Coordinate System: Relative Angular and Translational Orientation

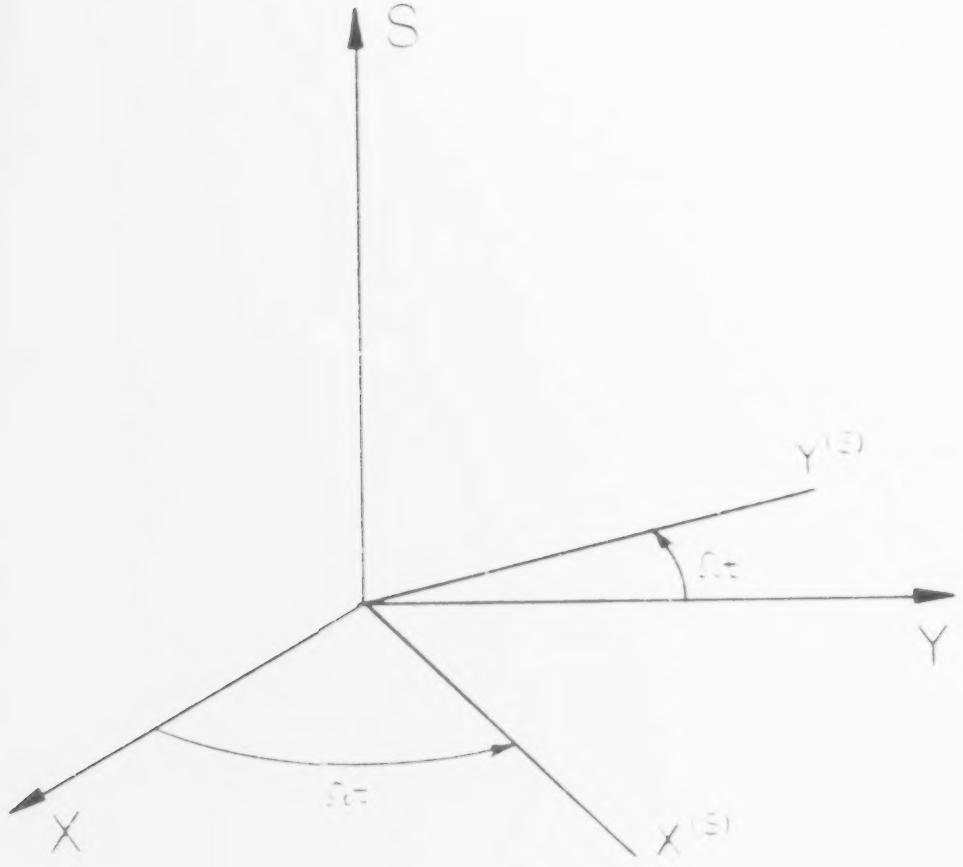

Figure A.1.4. Spinning Coordinate System

m = rigid-body mass
$\underline{v}_o$ = center of mass velocity relative to the fixed reference system.

The right hand side of Equation A.1.1 can be most easily evaluated by taking the time derivative relative to the rotating reference frame, where the moments of inertia are not functions of time, and relating these time derivatives with respect to the rotating frame to the time derivatives with respect to the inertial frame by

$$\frac{d}{dt}\underline{c}^{(i)} = \frac{d}{dt}\underline{c}^{(r)} + \underline{\Omega} \times \underline{c} \qquad \text{(A.1.3)}$$

where

time derivatives are taken with respect to the coordinate system indicated by the superscript

$\underline{c}$ is any vector

$\underline{\Omega}$ = angular velocity of the rotating frame as seen from the inertial frame

$\underline{\Omega} \times \underline{c}$ indicates the vector cross product.

The following assumptions will be used, allowing the applied forces and torques to be related to the resultant positions of the two rigid bodies by linear equations.

1) The flywheel and hub are assumed to behave as rigid-bodies.

2) The rigid bodies have an axis of symmetry, which is the nominal spin-axis.

3) The angular momentum of the rigid bodies along the $S^{(r)}$-axis is constant.

4) The Bryant angles ϕ and θ are small.

These are the usual assumptions of rotordynamics, discussed in more detail in [Tondl 1965; Gunter 1966; Rao 1983; and Diamarogonas 1983] among others. With these assumptions rigid body positions are related to applied forces and torques by

$$
\begin{aligned}
M_x &= I_{rr}\ddot{\phi} + I_{zz}\Omega\dot{\theta} \\
M_y &= I_{rr}\ddot{\theta} - I_{zz}\Omega\dot{\phi} \\
F_x &= m\ddot{x} \\
F_y &= m\ddot{y}
\end{aligned}
\qquad \text{(A.1.4)}
$$

where

the applied torques M_x and M_y, the applied forces F_x and F_y, the Bryant angles ϕ and θ, and the positions x and y are functions of time expressed relative to the fixed, inertial frame,

$\dot{(\ )}$ indicates differentiation with respect to time in the fixed, inertial frame, and

I_{rr} and I_{zz} are the (constant) principal moments of inertia with respect to the center of mass.

Note that a set of these equations is necessary for each rigid body mass. The first two of Equations A.1.4 are the "gyro equations" used for analyzing gyroscopic instruments [Crandall 1968].

Spoke Structure Forces and Torques

The applied forces and torques are developed by two mechanisms, the interconnecting spoke structure and the magnetic bearing. Consider the spoke structure first. As noted earlier, the spokes are modelled as a linear, damped elastic structure. The force and torque generated by the spoke structure are, therefore, linearly related to the relative translational and angular displacements and velocities seen across the spoke structure. These relative translational and angular displacements are given by the relative orientation and position of "elastic axes". There are elastic axes fixed in each rigid body and are denoted as the "hub elastic axes" and the "flywheel elastic axes". The origins of these elastic axes are the points in the rigid bodies through which the force generated by the spoke structure acts. These origins will be called the elastic centers or spoke centers of force. When the origins of the hub and flywheel elastic axes coincide, which is the zero force equilibrium configuration, no elastic force is produced by the spoke structure. At this zero force equilibrium position, the two elastic axes systems are defined to be coincident with the principal elastic axes of the spoke structure.

These elastic axes are fixed in each rigid body but do not, in general, coincide with the principal inertial axes of the rigid bodies. For the non-synchronous model under development in

this section, however, the elastic and inertial axes are assumed to coincide. This is analogous to assuming a perfectly balanced rotor in conventional rotor dynamic models.

In the $(X^{(s)},Y^{(s)},S^{(s)})$ axes system, which spins with the spoke system, the following linear relation between the relative displacements of the two rigid bodies and the forces and torques produced by the spoke structure is therefore assumed

$$\underline{F}_S = -k_t\underline{\Delta r} - c_t \frac{d^{(s)}}{dt}(\underline{\Delta r}) \qquad (A.1.5)$$

$$\underline{M}_S = -k_a\underline{\Delta T} - ca \frac{d^{(s)}}{dt}(\underline{\Delta T}) \qquad (A.1.6)$$

where

$\underline{F}_S$ = radial force acting on the flywheel mass due to the spoke structure

k_t = translational (radial) spring constant of the spoke structure

$\underline{\Delta r} = (x_f - x_h)\underline{i} + (y_f - y_h)\underline{j}$, the position of the flywheel center of mass relative to the hub center of mass

cr = radial damping constant of the spoke structure

$\underline{T}_S$ = radial torque acting on the flywheel due to the spoke structure

k_a = radial, torsional spring constant of the spoke structure

$\underline{\Delta T} = (\phi_f - \phi_h)\underline{i} + (\theta_f - \theta_h)\underline{j}$

c_a = radial, torsional damping constant of the spoke structure and

s superscript indicates differentiation with respect to the spinning reference frame.

The above relations are based either implicitly or explicitly on the following assumptions:

1) The spoke structure is modelled as a linear, elastic structure with linear damping.

2) The nominal spin axis of the hub and flywheel is a axis of symmetry for the spoke structure. The spoke structure, therefore, is assumed to have rotationally anisotropic translational and angular stiffnesses. This implies that there is no torque-radial displacement or force-angular displacement coupling and that the general tensor relation between generalized displacements and generalized forces reduces to scalar relations [Foley 1986].

3) The force generated by the spoke structure acts through the centers of mass of the two rigid bodies.

4) The spokes are massless.

Equations A.1.5 and A.1.6 give the force and torque generated by the spoke structure that act on the flywheel. The spoke structure generates an equal and opposite force and torque that act on the hub, of course. A derivation of the spoke structure force and torque equations and more detailed discussion of these assumptions are contained in thesis by [Foley 1986].

Again, Equation A.1.3 can be used to transform the time derivatives with respect to the spinning reference frame, as required in force and torque equations above, into time derivatives with respect to the fixed, inertial reference frame. This gives the spoke force and torque equations as

$$\underline{F}_S = -k_t\underline{\Delta r} - c_t \overset{(i)}{\frac{d}{dt}}(\underline{\Delta r}) + c_t(\underline{\Omega} \times \underline{\Delta r}) \qquad (A.1.7)$$

$$\underline{M}_S = -k_a\underline{\Delta T} - ca \overset{(i)}{\frac{d}{dt}}(\underline{\Delta T}) + c_a(\underline{\Omega} \times \underline{\Delta T}) \qquad (A.1.8)$$

where

$\underline{\Omega} = \Omega\underline{k}$, the angular velocity of the spinning frame as seen from the inertial frame

i superscript indicates differentiation with respect to the inertial frame.

Expressed in the inertial coordinate system, the scalar components of the force and torque generated by the spoke system are now given by

$$
\begin{aligned}
F_x &= -k_t(x_f - x_h) - c_t\Omega(y_f - y_h) - c_t(\dot{x}_f - \dot{x}_h) \\
F_y &= -k_t(y_f - y_h) + c_t\Omega(x_f - x_h) - c_t(\dot{y}_f - \dot{y}_h) \\
M_x &= -k_a(\phi_f - \phi_h) - c_a\Omega(\theta_f - \theta_h) - c_t(\dot{\phi}^f - \dot{\phi}^h) \\
M_y &= -k_a(\theta_f - \theta_h) + c_aD(\phi_f - \phi_h) - c_t(\dot{\theta}_f - \dot{\theta}_h)
\end{aligned}
\qquad \text{(A.1.9)}
$$

where the f and h subscripts denote flywheel and hub respectively. The important coupling effect of the internal damping can now be seen. For example, the spoke force in the x-direction is now a function of the y-direction displacements and the rotational speed Ω.

Lorentz Bearing

The Lorentz bearing is assumed to act as an ideal, linear actuator with currents as inputs and forces and torques acting on the hub as outputs. With these assumptions, the bearing forces can be written as

$$
\begin{aligned}
F_x &= k_{lt} i_x \\
F_y &= k_{lt} i_y \\
M_x &= k_{la} i_\phi \\
M_y &= k_{la} i_\theta
\end{aligned}
\qquad \text{(A.1.10)}
$$

where

F_x, F_y, M_x, and M_y now denote the bearing forces and torques

i_x, i_y, i_ϕ, and i_θ are the currents driving the Lorentz bearing

k_{lt} = Lorentz bearing translational force/input current proportionality constant

k_{la} = Lorentz bearing angular torque/input current proportionality constant.

At this point in the development, the forces generated by the Lorentz bearing are assumed to act through the hub center of mass.

A.2 Equations of Motion: Non-synchronous Model

The equations for the spoke forces and torques (Equations A.1.9) can be combined together with the bearing forces and torques (Equations A.1.10) and the force-torque/position-tilt relations (Equation A.1.4) to give the equations of motion as

$$
\begin{aligned}
m_f\ddot{x}_f + c_t(\dot{x}_f - \dot{x}_h) + k_t(x_f - x_h) + c_t\Omega(y_f - y_h) &= 0 \\
m_h\ddot{x}_h - c_t(\dot{x}_f - \dot{x}_h) - k_t(x_f - x_h) - c_t\Omega(y_f - y_h) &= k_{lt}i_x \\
m_f\ddot{y}_f + c_t(\dot{y}_f - \dot{y}_h) + k_t(y_f - y_h) - c_t\Omega(x_f - x_h) &= 0 \\
m_h\ddot{y}_h - c_t(\dot{y}_f - \dot{y}_h) - k_t(y_f - y_h) + c_t\Omega(x_f - x_h) &= k_{lt}i_y \\
I_{fr}\ddot{\phi}_f + c_a(\dot{\phi}_f - \dot{\phi}_h) + I_{fz}\Omega\dot{\theta}_f + k_a(\phi_f - \phi_h) + c_a\Omega(\theta_f - \theta_h) &= 0 \\
I_{hr}\ddot{\phi}_h - c_a(\dot{\phi}_f - \dot{\phi}_h) + I_{hz}\Omega\dot{\theta}_h - k_a(\phi_f - \phi_h) - c_a\Omega(\theta_f - \phi_h) &= k_{la}i_\phi \\
I_{fr}\ddot{\theta}_f + c_a(\dot{\theta}_f - \dot{\theta}_h) - I_{fz}\Omega\dot{\phi}_f + k_a(\theta_f - \theta_h) - c_a\Omega(\phi_f - \phi_h) &= 0 \\
I_{hr}\ddot{\theta}_f - c_a(\dot{\theta}_f - \dot{\theta}_h) - I_{hz}\Omega\dot{\phi}_h - k_a(\theta_f - \theta_h) + c_a\Omega(\phi_f - \phi_h) &= k_{la}i_\theta
\end{aligned}
\qquad (A.2.1)
$$

where

F_x, F_y, M_x, M_y now refer to the forces and torques produced by the magnetic bearing

I_{fr}, I_{fz}, I_{hr}, and I_{hz} are the radial (subscript r) and axial (subscript z) moments of inertia of the flywheel (subscript f) and hub (subscript h).

The model of the CARES system described by Equations A.2.1 is analogous to a conventional flexible rotor model that assumes the rotor masses are perfectly balanced and an axisymmetric shaft with linear stiffness and damping. Because of the lack of "unbalance" disturbances, this model is unsuitable for analysis of the synchronous response of the CARES system. The model is, however, appropriate for the analysis of non-synchronous performance including, most importantly, the stability of the rotor/bearing system.

A.2.1 Translational Dynamics: Non-synchronous Model

Note that these equations of motion separate into two uncoupled models, one for the translational dynamics and one for the angular or tilt dynamics. For the translational dynamics, the equations of motion are given by

$$
\begin{aligned}
m_f\ddot{x}_f + c_t(\dot{x}_f - \dot{x}_h) + k_t(x_f - x_h) + c_t\Omega(y_f - y_h) &= 0 \\
m_f\ddot{y}_f + c_t(\dot{y}_f - \dot{y}_h) + k_t(y_f - y_h) - c_t\Omega(x_f - x_h) &= 0 \\
m_h\ddot{x}_h - c_t(\dot{x}_f - \dot{x}_h) - k_t(x_f - x_h) - c_t\Omega(y_f - y_h) &= k_{lt}i_x \\
m_h\ddot{y}_h - c_t(\dot{y}_f - \dot{y}_h) - k_t(y_f - y_h) + c_t\Omega(x_f - x_h) &= k_{lt}i_y
\end{aligned}
\qquad \text{(A.2.2)}
$$

The notation can be simplified by introducing the complex displacement variable

$$z = x + jy \qquad (j = \sqrt{-1}) \qquad \text{(A.2.3)}$$

and the complex bearing force

$$F_c = F_x + jF_y \qquad \text{(A.2.4)}$$

Using this complex notation, the translational equations of motion are given by

$$
\begin{bmatrix} m_f & 0 \\ 0 & m_h \end{bmatrix}
\begin{bmatrix} \ddot{z}_f \\ \ddot{z}_h \end{bmatrix}
+
\begin{bmatrix} c_t & -c_t \\ -c_t & c_t \end{bmatrix}
\begin{bmatrix} \dot{z}_f \\ \dot{z}_h \end{bmatrix}
+
\begin{bmatrix} k_t - j\Omega c_t & -k_t + j\Omega c_t & z_f \\ -k_t + j\Omega c_t & k_t - j\Omega c_t & z_h \end{bmatrix}
=
\begin{bmatrix} 0 \\ F_c \end{bmatrix}
\qquad \text{(A.2.5)}
$$

Multiplying through by the inverse of the inertia matrix gives

$$\ddot{\underline{z}} + C_t\dot{\underline{z}} + (K_t - j\Omega C_t)\underline{z} = \underline{F}_c \qquad \text{(A.2.6)}$$

where the vector $\underline{z}$ is comprised of the complex flywheel and hub positions

$$\underline{z}^T = [z_f, z_h] = [x_f + jy_f, x_h + jy_h] \qquad \text{(A.2.7)}$$

the normalized radial damping matrix C_t and radial stiffness matrix K_t are

$$C_t = \begin{bmatrix} \frac{c_t}{m_f} & \frac{-c_t}{m_f} \\ \frac{-c_t}{m_h} & \frac{c_t}{m_h} \end{bmatrix} \qquad K_t = \begin{bmatrix} \frac{k_t}{m_f} & \frac{-k_t}{m_f} \\ \frac{-k_t}{m_h} & \frac{k_t}{m_h} \end{bmatrix} \tag{A.2.8}$$

and $\underline{F}_c$ is a vector of normalized, complex bearing control forces

$$\underline{F}_c = [0, \; F_c/m_h]^T = [0, \; (F_x + jF_y)/m_h]^T \tag{A.2.9}$$

Put into state-space form, with complex state variables, these equations of motion are

$$\begin{bmatrix} \dot{\underline{z}} \\ \ddot{\underline{z}} \end{bmatrix} = \begin{bmatrix} 0 & I \\ -(K_t - j\Omega C_t) & -C_t \end{bmatrix} \begin{bmatrix} \underline{z} \\ \dot{\underline{z}} \end{bmatrix} + \begin{bmatrix} \underline{0} \\ \underline{F}_c \end{bmatrix} \tag{A.2.10}$$

Using the complex notation, this is a four state system with state vector $[z_f, \; z_h, \; \dot{z}_f, \; \dot{z}_h]^T$ controlled by the complex force F_c.

Expanding back into real notation and substituting the Lorentz bearing force/current relation gives the following state-space form

$$
\begin{bmatrix} \dot{x}_f \\ \dot{x}_h \\ \ddot{x}_f \\ \ddot{x}_h \\ \dot{y}_f \\ \dot{y}_h \\ \ddot{y}_f \\ \ddot{y}_h \end{bmatrix} =
\begin{bmatrix}
0 & 0 & I & 0 & 0 & 0 & 0 & 0 \\
0 & 0 & 0 & I & 0 & 0 & 0 & 0 \\
\frac{-k_t}{m_f} & \frac{k_t}{m_f} & \frac{-c_t}{m_f} & \frac{c_t}{m_f} & \frac{-\Omega c_t}{m_f} & \frac{\Omega c_t}{m_f} & 0 & 0 \\
\frac{k_t}{m_h} & \frac{-k_t}{m_h} & \frac{c_t}{m_h} & \frac{-c_t}{m_h} & \frac{\Omega c_t}{m_h} & \frac{-\Omega c_t}{m_h} & 0 & 0 \\
0 & 0 & 0 & 0 & 0 & 0 & I & 0 \\
0 & 0 & 0 & 0 & 0 & 0 & 0 & I \\
\frac{\Omega c_t}{m_f} & \frac{-\Omega c_t}{m_f} & 0 & 0 & \frac{-k_t}{m_f} & \frac{k_t}{m_f} & \frac{-c_t}{m_f} & \frac{c_t}{m_f} \\
\frac{-\Omega c_t}{m_h} & \frac{\Omega c_t}{m_h} & 0 & 0 & \frac{k_t}{m_h} & \frac{-k_t}{m_h} & \frac{c_t}{m_h} & \frac{-c_t}{m_h}
\end{bmatrix}
\begin{bmatrix} x_f \\ x_h \\ \dot{x}_f \\ \dot{x}_h \\ y_f \\ y_h \\ \dot{y}_f \\ \dot{y}_h \end{bmatrix} +
\begin{bmatrix}
0 & 0 \\
0 & 0 \\
0 & 0 \\
\frac{k_{1t}}{m_h} & 0 \\
0 & 0 \\
0 & 0 \\
0 & 0 \\
0 & \frac{k_{1t}}{m_h}
\end{bmatrix}
\begin{bmatrix} i_x \\ i_y \end{bmatrix}
\tag{A.2.11}
$$

Using this real notation, the system has eight states and is controlled by the currents i_x and i_y that produce the translational forces F_x and F_y. This can be represented in standard form by

$$\dot{\underline{x}} = A\underline{x} + B\underline{u} \tag{A.2.12}$$

where

$\underline{x} = [x_f, x_h, \dot{x}_f, \dot{x}_h, y_f, y_h, \dot{y}_f, \dot{y}_h]^T$, the state vector

$\underline{u} = [i_x, i_y]^T$, the Lorentz bearing translational currents.

Note that the state dynamics matrix A and control effectivness matrix B can be partitioned as

$$A = \begin{bmatrix} A_r & -A_i \\ A_i & A_r \end{bmatrix} \qquad B = \begin{bmatrix} B_r & -B_i \\ B_i & B_r \end{bmatrix} \tag{A.2.13}$$

Matrices that can be partitioned as above will be called "block-symmetric" in this thesis. Block-symmetric matrices have the property that the diagonal partitions (A_r and B_r in Equation A.2.13) are identical and the off-diagonal partitions (A_i and B_i in Equation A.2.13) are identical but of opposite signs. The fact that the CARES dynamics are described by block-symmetric matrices allows the use of complex notation. The relation between systems described by these block-symmetric matrices and the use of complex notation is explored more fully in Chapter 4 of [Johnson 1987].

A.2.2 Angular Dynamics: Non-synchronous Model

The angular or tilt dynamics have a similar form to the translational dynamics but with the addition of gyroscopic terms. Referring to Equations A.2.1, the angular dynamics are given by

$$\begin{aligned}
&I_{fr}\ddot{\theta}_f + c_a(\dot{\theta}_f - \dot{\theta}_h) + I_{fz}\Omega\dot{\theta}_f + k_a(\theta_f - \theta_h) + c_a\Omega(\theta_f - \theta_h) = 0 \\
&I_{hr}\ddot{\theta}_h - c_a(\dot{\theta}_f - \dot{\theta}_h) + I_{hz}\Omega\dot{\theta}_h - k_a(\theta_f - \theta_h) - c_a\Omega(\theta_f - \theta_h) = k_{la}\theta_a \\
&I_{fr}\ddot{\theta}_f + c_a(\dot{\theta}_f - \dot{\theta}_h) - I_{fz}\Omega\dot{\theta}_f + k_a(\theta_f - \theta_h) - c_a\Omega(\theta_f - \theta_h) = 0 \\
&I_{hr}\ddot{\theta}_f - c_a(\dot{\theta}_f - \dot{\theta}_h) - I_{hz}\Omega\dot{\theta}_h - k_a(\theta_f - \theta_h) + c_a\Omega(\theta_f - \theta_h) = k_{la}\theta_a
\end{aligned} \tag{A.2.14}$$

Again, the notation can be simplified by introducing the complex angular displacement

$$\lambda = \theta_x + j\theta_y \tag{A.2.15}$$

and the complex bearing torque

$$M_c = M_x + jM_y \tag{A.2.16}$$

Using this complex notation and dividing through by the moments

of inertia, the angular dynamics are given by

$$\underline{\psi} + (C_a - j\Omega G)\underline{\dot{\psi}} + (K_a - j\Omega C_a)\underline{\psi} = \underline{M}_c \qquad (A.2.17)$$

where the vector $\underline{\psi}$ is comprised of the flywheel and hub angular displacements as

$$\underline{\psi} = [\psi_f, \ \psi_h]^T = [\phi_f + j\theta_f, \ \phi_h + j\theta_h]^T \qquad (A.2.18)$$

the vector $\underline{M}_c$ contains the normalized, complex bearing torques as

$$\underline{M}_c = [0, \ (M_x + jM_y)/I_{hr}]^T \qquad (A.2.19)$$

and the normalized angular damping matrix C_a, gyroscopic matrix G, and angular stiffness matrix K_a are given by

$$C_a = \begin{bmatrix} \frac{c_a}{I_{fr}} & \frac{-c_a}{I_{fr}} \\ \frac{-c_a}{I_{hr}} & \frac{c_a}{I_{hr}} \end{bmatrix} \qquad G = \begin{bmatrix} 0 & \frac{I_{fz}}{I_{fr}} \\ \frac{I_{hz}}{I_{hr}} & 0 \end{bmatrix} \qquad K_a = \begin{bmatrix} \frac{k_a}{I_{fr}} & \frac{-k_a}{I_{fr}} \\ \frac{-k_a}{I_{hr}} & \frac{k_a}{I_{hr}} \end{bmatrix} \qquad (A.2.20)$$

Put into state-space form, with complex state variables, these equations of motion for the angular dynamics are

$$\begin{bmatrix} \dot{\underline{\psi}} \\ \ddot{\underline{\psi}} \end{bmatrix} = \begin{bmatrix} 0 & I \\ -(K_a - j\Omega C_a) & -(C_a - j\Omega G) \end{bmatrix} \begin{bmatrix} \underline{\psi} \\ \dot{\underline{\psi}} \end{bmatrix} + \begin{bmatrix} \underline{0} \\ \underline{M}_c \end{bmatrix} \qquad (A.2.21)$$

Using the complex notation, this is a four state system with state vector $[\psi_f, \ \psi_h, \ \dot{\psi}_f, \ \dot{\psi}_h]^T$ controlled by the complex bearing torque M_c.

Expanding back into real notation gives the following real state-space form

$$
\begin{bmatrix} \dot{\phi}_f \\ \dot{\phi}_h \\ \ddot{\phi}_f \\ \ddot{\phi}_h \\ \dot{\theta}_f \\ \dot{\theta}_h \\ \ddot{\theta}_f \\ \ddot{\theta}_h \end{bmatrix} =
\begin{bmatrix}
0 & 0 & I & 0 & 0 & 0 & C & 0 \\
0 & 0 & 0 & I & 0 & 0 & 0 & 0 \\
\frac{-k_a}{I_{fr}} & \frac{k_a}{I_{fr}} & \frac{-c_a}{I_{fr}} & \frac{c_a}{I_{fr}} & \frac{-\Omega c_a}{I_{fr}} & \frac{\Omega c_a}{I_{fr}} & \frac{-\Omega I_{fz}}{I_{fr}} & 0 \\
\frac{k_a}{I_{hr}} & \frac{-k_a}{I_{hr}} & \frac{c_a}{I_{hr}} & \frac{-c_a}{I_{hr}} & \frac{\Omega c_a}{I_{hr}} & \frac{-\Omega c_a}{I_{hr}} & 0 & \frac{-\Omega I_{hz}}{I_{hr}} \\
0 & 0 & 0 & 0 & 0 & 0 & I & 0 \\
0 & 0 & 0 & 0 & 0 & 0 & 0 & I \\
\frac{\Omega c_a}{I_{fr}} & \frac{-\Omega c_a}{I_{fr}} & \frac{\Omega I_{fz}}{I_{fr}} & 0 & \frac{-k_a}{I_{fr}} & \frac{k_a}{I_{fr}} & \frac{-c_a}{I_{fr}} & \frac{c_a}{I_{fr}} \\
\frac{-\Omega c_a}{I_{hr}} & \frac{\Omega c_a}{I_{hr}} & 0 & \frac{\Omega I_{hz}}{I_{hr}} & \frac{k_a}{I_{hr}} & \frac{-k_a}{I_{hr}} & \frac{c_a}{I_{hr}} & \frac{-c_a}{I_{hr}}
\end{bmatrix}
\begin{bmatrix} \phi_f \\ \phi_h \\ \dot{\phi}_f \\ \dot{\phi}_h \\ \theta_f \\ \theta_h \\ \dot{\theta}_f \\ \dot{\theta}_h \end{bmatrix}
+
\begin{bmatrix}
0 & 0 \\
0 & 0 \\
0 & 0 \\
\frac{k_{1a}}{I_{hr}} & 0 \\
0 & 0 \\
0 & 0 \\
0 & 0 \\
0 & \frac{k_{1t}}{I_{hr}}
\end{bmatrix}
\begin{bmatrix} i_\phi \\ i_\theta \end{bmatrix}
$$

(A.2.22)

APPENDIX B. CONTROLLER DESIGN GOALS AND METHODS

This appendix discusses the various controller designs that were investigated. Section B.1 introduces the full-state feedback compensators that were investigated. Section B.2 discusses the corresponding output-feedback compensators that will be investigated.

B.1 Full-State Feedback: Linear Quadratic Regulators

The full-state feedback controllers that were investigated are the well known deterministic, linear-quadratic regulators. The LQR was examined both to understand achievable performance of a full-state feedback controller and as an indication of the closed-loop performance of the output-feedback, model-based compensator designed using linear quadratic Gaussian synthesis with loop transfer recovery. These model-based compensators will be discussed in the next section. In this section we consider the linear quadratic regulator as an full-state feedback controller.

The linear quadratic regulator has been extensively studied both because of its time optimal characteristics and its good frequency domain attributes [Kwakernaak, 1972]. The linear quadratic regulator is the optimal set of full-state feedback gains which will bring any initial state of the system to equilibrium, while minimizing the cost

$$J(t_1) = \int_0^{\tau_1} \underline{x}^T(\tau)Q\underline{x}(\tau) + \underline{u}^T(\tau)R\underline{u}(\tau)d\tau \qquad (B.1.1)$$

subject to the dynamic constraint imposed by the system state equations. In the time-optimal interpretation, the matrices Q and R express the relative costs assigned to deviations of the state from equilibrium and control effort. In this research, however, these will be considered as free design parameters used to achieve desirable frequency domain shapes of the loop transfer function matrix.

If the terminal time of the problem is made infinite ($t^1 \to \infty$), the optimal controller consists of the time-independent gains $K(\Omega_d)$ relating system state to control input as

$$\underline{u}(t) = -K(\Omega_d)\underline{x}(t) \qquad (B.1.2)$$

where the feedback gain matrix $K(\Omega_d)$ is given by

$$K(\Omega_d) = R^{-1}BS(\Omega_d) \qquad (B.1.3)$$

and $\mathbf{S}$ is the unique positive definite solution matrix[1] of the algebraic Riccati equation

$$-\mathbf{S}(\Omega_d)\mathbf{A}(\Omega_d) - \mathbf{A}(\Omega_d)^T\mathbf{S}(\Omega_d) - \mathbf{Q} + \mathbf{S}(\Omega_d)\mathbf{B}\mathbf{R}^{-1}\mathbf{B}\mathbf{S}(\Omega_d) = 0 \quad (B.1.4)$$

Note that the feedback gains $\mathbf{K}(\Omega_d)$ are a function of the design rotational speed (Ω_d) because the system dynamics matrix $\mathbf{A}(\Omega_d)$ used in the algebraic Riccati equation is a function of rotational speed.

The closed-loop system controlled by the LQR is shown in figure B.1.1. The inputs are the command reference, shown set equal to zero, and the two synchronous disturbances, both functions of the rotational speed Ω. The full state of the system is fed back to the input through the LQR gains $\mathbf{K}$. Note that the closed-loop system is a function of both the design rotational speed Ω_d, through the LQR gains $\mathbf{K}(\Omega_d)$, and the actual rotational speed Ω, through the disturbances and the system dynamics matrix $\mathbf{A}(\Omega)$.

In this research, the state weighting matrix $\mathbf{Q}$ is a ways set equal to $\mathbf{C}\mathbf{C}^T$, meaning that only the plant output will be weighted. For the translational model, then, only the hub position is weighted and for the angular model hub orientation is weighted. The control weighting matrix $\mathbf{R}$ always had the form

$$\mathbf{R} = \rho\mathbf{I} \quad (B.1.5)$$

where ρ is a scalar that determines the cross-over frequency of the loop transfer function

$$\mathbf{G}_{lq}(s) = \mathbf{K}(\Omega_d)(s\mathbf{I} - \mathbf{A}(\Omega))^{-1}\mathbf{B} \quad (B.1.6)$$

This open-loop transfer function, the so called "LQ loop" can be found in figure B.1.1 when the loop is broken at the point marked 1. The $\mathbf{Q}$ and $\mathbf{R}$ matrices are chosen such that the LQ loop has desirable frequency domain characteristics. This design methodology is similar to SISO design technique of achieving desirable system performance through shaping of the open-loop bode magnitude plots. The measure used for these MIMO systems, however, will be the maximum and minimum singular values of the LQ loop.

---

1 See Kwakernaak [1972, p238] for sufficient conditions.

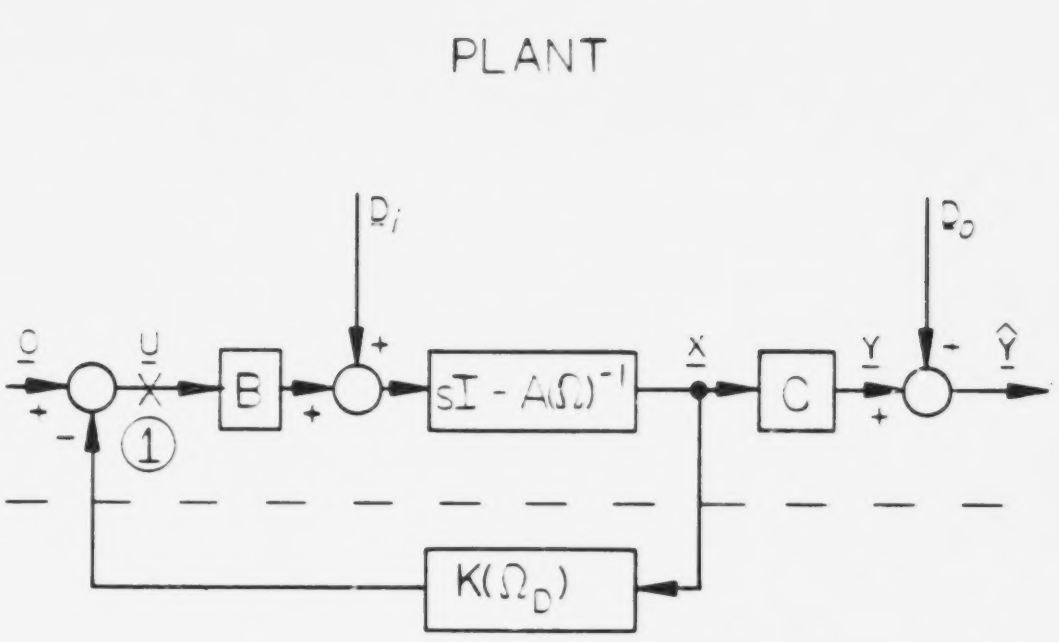

Figure B.1.1. Linear Quadratic Regulator Loop Configuration

If the actual rotational speed Ω is equal to the design rotational speed Ω_d and the control weighting matrix **R** is diagonal, which it always was for the designs used in this research, the LQ loop possesses the following desirable stability robustness properties. The simultaneous and independent stability margins in all feedback paths are:

1) Upward gain margin is infinite

2) Downward gain margin is at least 6db

3) Phase margins are at least ± 60°

Again, these good stability margins are only guaranteed when the design and rotational speeds are the same.

Another property of the LQ loop that was used extensively is the "root square locus". Given the design choices made for **Q** and **R** and assuming a fixed design rotational speed Ω_d equal to the actual rotational speed Ω, the closed-loop pole locations are only a function of the design parameter ρ (Equation B.1.5). The root-square locus method can be used to find the locations of these closed-loop poles as ρ varies [Kwakernaak 1972, p281]. If the design parameter ρ approaches infinity, the so called "expensive control" problem, the closed-loop poles of the LQR approach the open-loop poles of the plant transfer function[1]

$$G_p(s) = C(sI - A)^{-1}B \qquad (B.1.7)$$

if an open-loop pole lies in the LHP. If the open-loop pole lies in the RHP, the closed-loop pole approaches the LHP image of the open-loop pole. If the design parameter ρ approaches zero, the so called "cheap control" problem, some of the closed-loop poles of the LQR approach the open-loop zeros of $G_p(s)$. The remainder of the closed-loop poles go to infinite along the stable branches of multiple Butterworth patterns.

During this research, results were developed for the LQR in both fixed- and variable-gain configurations. In the variable gain configuration, the design rotational speed Ω_d is kept equal to the actual rotational speed Ω. This results in a variable gain controller $K(\Omega)$. The closed-loop performance of the system with the variable-gain configuration is a function of the two design parameters **R** and **Q** and the rotational speed Ω. In the fixed-gain configuration, the feedback gain matrix **K** is fixed based on the design parameters **R**, **Q**, and the design rotational speed Ω_d. The plant, of course, still changes with changing rotational speed. The closed-loop performance of the system with

---

1 Because of the design choose setting $Q = CC^T$.

the fixed-gain LQR is a function of the two design parameters R and Q, the design rotational speed Ω_d, and the actual rotational speed Ω. These variable- and fixed-gain linear quadratic regulators were investigated for a variety of design parameters and rotational speeds.

B.2 Output Feedback: Model Based Compensators

Although the performance of full-state feedback controllers was investigated, the main thrust of the controller development was aimed at output feedback compensators based on measurement of hub position and orientation. This section discusses a specific class of compensators, the model based compensators (MBC) designed using linear quadratic Gaussian synthesis with loop transfer recovery (LQG/LTR) that will be extensively examined in the following chapters.

The MBC designed using the LQG/LTR procedure consists of a Kalman filter combined with a linear quadratic regulator. The Kalman filter is used as a full-state observer to estimate the state of the system. This estimated state is used by the LQR to produce the controller output. This configuration is shown in figure B.2.1. The transfer function of the model based compensator is given by $\mathbf{K}_{mbc}(s)$ and of the plant by $\mathbf{G}_p(s)$. The system output $\underline{Y}(s)$ is comprised of the plant output corrupted by the spoke disturbance $\underline{D}^I(s)$. The compensator has as its input the system output corrupted by the measurement error $\underline{D}^O(s)$.

The internal structure of the model based compensator and plant are shown in figure B.2.2. As can be seen in this figure, the compensator structure mimics the plant structure, hence the name "model based compensator." The $\mathbf{A}(\Omega_d)$, B, and C matrices of the compensator are all determined by the plant model and the choice of design rotational speed Ω_d. The matrix $\mathbf{K}(\Omega_d)$ comes from the solution to the LQR problem, as discussed in section B.2. This feedback matrix is a function of the design parameters R and Q as well as the design rotational speed Ω_d. The Kalman filter matrix $\mathbf{H}(\Omega_d)$ formally comes from the solution of the steady state Kalman filter problem, which will be discussed below. Using the loop transfer recovery method, this matrix will be determined by the plant model, which is a function of the design rotational speed Ω_d, and a free design parameter .

The LQG/LTR methodology attempts to design the Kalman filter gain matrix $\mathbf{H}(\Omega_d)$ such that the good frequency domain shape and stability robustness of the full-state feedback LQ loop is recovered in an output feedback compensator. In order to achieve this goal, the Kalman filter design is used in a very specific way, the so called "accurate measurement" Kalman filter problem. Consider the stochastic, linear, time-invariant system

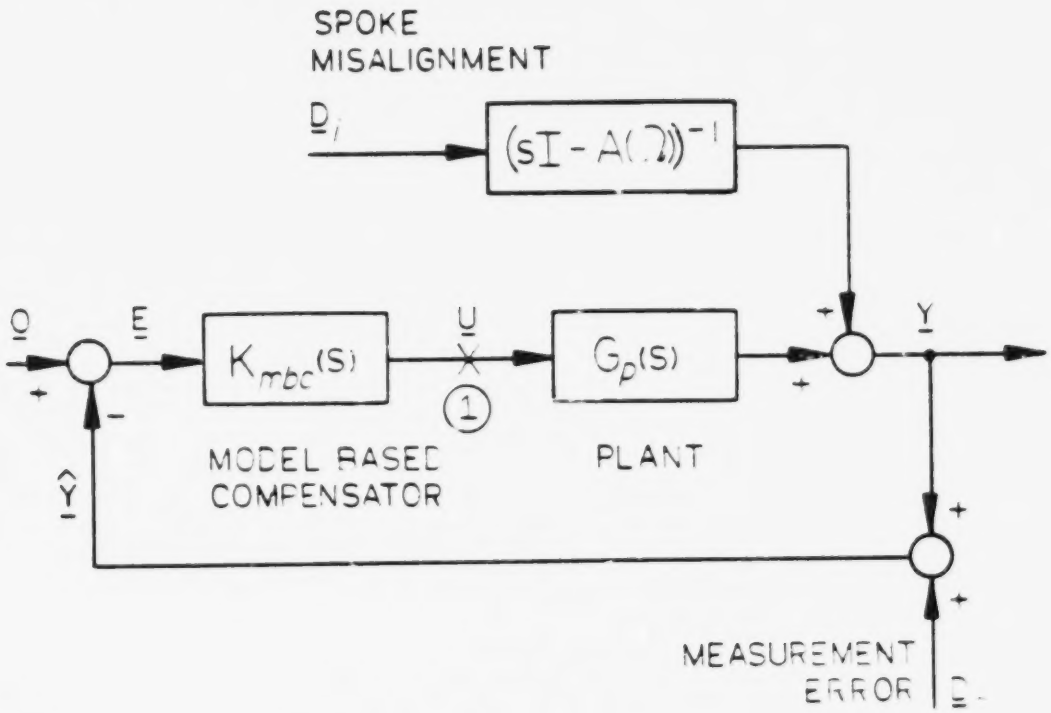

Figure B.2.1. Model Based Compensator Loop Configuration

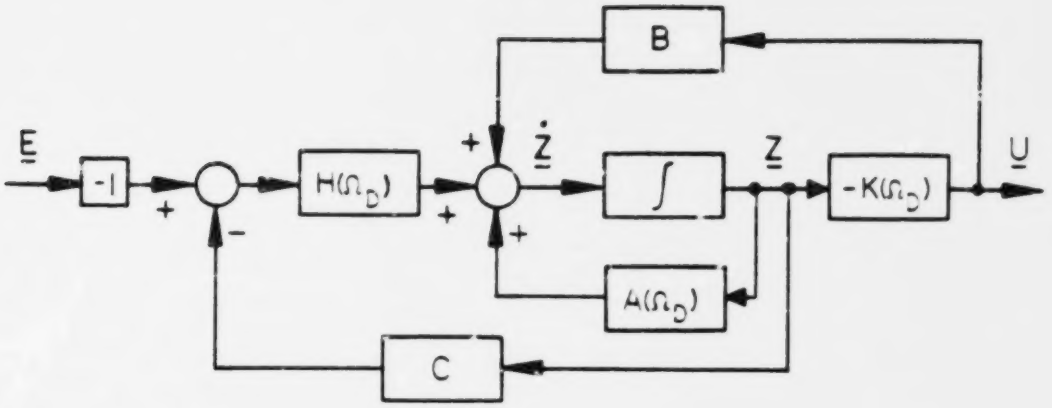

a) Model based compensator $K_{mbc}(s)$

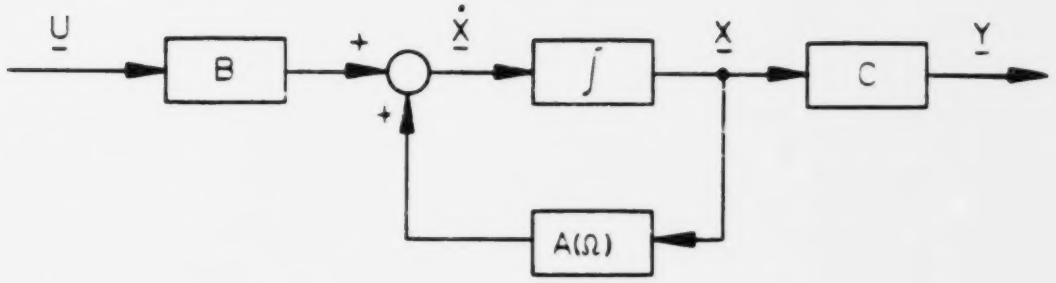

b) Plant

Figure B.2.2. Block Diagram of Model Based Compensator and Plant

$$\dot{\underline{x}}(t) = \mathbf{A}\underline{x}(t) + \underline{w}(t) \qquad \text{(B.2.1)}$$

$$\underline{y}(t) = \mathbf{C}\underline{x}(t) + \underline{v}(t) \qquad \text{(B.2.2)}$$

where the process noise $\underline{w}(t)$ is assumed white with zero-mean as

$$E[\underline{w}(\tau)\underline{w}^T(t)] = \mathbf{B}\mathbf{B}^T\delta(t - \tau) \qquad \text{(B.2.3)}$$

and the measurement noise $\underline{v}(t)$ is assumed white with zero-mean and unit intensity indexed by the design parameter as

$$E[\underline{v}(\tau)\underline{v}^T(t)] = \mu\mathbf{I}\delta(t - \tau) \qquad \text{(B.2.4)}$$

Under the assumption that $[\mathbf{A}, \mathbf{B}]$ is stabilizable and $[\mathbf{A}, \mathbf{C}]$ detectable, the Kalman filter gain matrix H is given by

$$\mathbf{H} = \frac{1}{\mu}\Sigma\mathbf{C}^T \qquad \text{(B.2.5)}$$

where the error covariance matrix is the solution to the algebraic Ricatti equation

$$\mathbf{A}\Sigma + \Sigma\mathbf{A}^T + \mathbf{B}\mathbf{B}^T - \frac{1}{\mu}\Sigma\mathbf{C}^T\mathbf{C}\Sigma = 0 \qquad \text{(B.2.6)}$$

If $G_p(s)$ is has no non-minimum phase transmission zeros, the loop transfer function of the MBC approaches the loop transfer function of the LQR as the design parameter $\mu \to 0$. More specifically, for the MBC of Figure B.2.1, if

1) the design rotational speed Ω_d is equal to the actual rotational speed and

2) the plant transfer function $G_p(s) = \mathbf{C}(s\mathbf{I} - \mathbf{A})^{-1}\mathbf{B}$ has no non-minimum phase transmission zeros,

then the loop transfer function of figure B.2.1 broken at point 1, which is given by

$$\mathbf{K}_{mbc}(s)\mathbf{G}_p(s) = \mathbf{K}(s\mathbf{I} - \mathbf{A} + \mathbf{B}\mathbf{K} + \mathbf{H}\mathbf{C})^{-1}\mathbf{H}\mathbf{C}(s\mathbf{I} - \mathbf{A})^{-1}\mathbf{B}, \qquad \text{(B.2.7)}$$

converges, pointwise in s, to the LQ loop transfer function

$$G_{lq}(s) = K(sI - A)^{-1}B \qquad (B.2.8)$$

This, then, is the important result. By the use of the accurate measurement Kalman filter, the good loop shape and stability robustness of the full-state feedback, linear quadratic loop can be recovered[1] in a output-feedback compensator [Doyle 1981] In practice, the design parameter μ will be used to control the frequency range over which the LQ loop is recovered.

This important loop recovery result, however, is contingent on the two premises, which will not always be satisfied. Since the goal is to design fixed-gain compensators, obviously the design rotational speed will not always match the actual rotational speed, which is assumed to vary. This will, of course, be true for both the translational and angular model. Also, the translational model exhibits non-minimum phase transmission zeros at super-flexible speeds, which also violates the necessary conditions for loop recovery. In these cases, good stability robustness and disturbance is not guaranteed. As was shown during this research [Johnson 1987], however, the MBC will retain good stability properties in many of the super-flexible cases[2].

With the LQG/LTR approach and the design choices already discussed, three design parameters will specify the MBC. These parameters are:

1) The linear quadratic regulator parameter ρ which controls the bandwidth of the LQ loop.

---

1 For general MIMO systems the LQ loop is recovered in loop transfer function of the MBC when the loop is broken at the plant input only. For two-input, two-output, block-symmetric systems such as the ACCESS translational and angular models, however, the loop transfer function matrix of the loop broken at the plant input $K_{mbc}(s)G_p(s)$ is equal to the loop transfer function matrix when the loop is broken at the plant output $G_p(s)K_{mbc}(s)$. This can be easily seen by using the complex formulation and the fact that the multiplication of complex scalars commutes. For the ACCES system, therefore, the good stability robustness and distrubance rejection properties of the LQ loop are reflected in the MBC loop transfer function matrix broken at either the plant input or output.

2 The use of model based compensators in conjunction with non-minimum phase systems is an area of current research.

2) The Kalman filter parameter μ which controls the bandwidth of the loop recovery.

3) The design rotational speed Ω_d, which effects both the compensator through both the LQ gain matrix $K(\Omega_d)$ and the Kalman filter matrix $H(\Omega_d)$.

The closed-loop system, of course, is a function of these three design parameters and the actual rotational speed. The closed-loop performance of the translational and angular models controlled by MBC's for variety of design parameters ρ, μ, and Ω_d and with varying rotational speed Ω were investigated during this research. Besides these model based compensators, more conventional output-feedback controllers using lead-lag compensators were also investigated.

NASA
National Aeronautics and Space Administration

Report Documentation Page

1. Report No.	2. Government Accession No.	3. Recipient's Catalog No.
NASA CR-4138		

4. Title and Subtitle	5. Report Date
Modelling and Control of an Annular Momentum Control Device	April 1988
	6. Performing Organization Code

7. Author(s)	8. Performing Organization Report No.
James R. Downer and Bruce G. Johnson	
	10. Work Unit No. 506-46-11-03

9. Performing Organization Name and Address	11. Contract or Grant No.
The Charles Stark Draper Laboratory, Inc. 555 Technology Square Cambridge, MA 02139	NAS9-16023 and NAS9-17560
	13. Type of Report and Period Covered
12. Sponsoring Agency Name and Address	Contractor Report
National Aeronautics and Space Administration Langley Research Center Hampton, VA 23665-5225	14. Sponsoring Agency Code

15. Supplementary Notes

James R. Downer and Bruce G. Johnson: SatCon Technology Corporation, 71 Rogers Street, Cambridge, MA 02142

Langley Research Center Technical Monitor: C. R. Keckler - This report was prepared by SatCon Technology Corporation under subcontract DL-C-274044 to the Charles Stark Draper Laboratory, Inc.

16. Abstract

This report documents the results of a modelling and control study for an advanced momentum storage device supported on magnetic bearings. The control challenge posed by this device lies in its dynamics being such a strong function of flywheel rotational speed. At high rotational speed, this can lead to open-loop instabilities, resulting in requirements for minimum and maximum control bandwidths and gains for the stabilizing controllers.

Using recently developed analysis tools for systems described by complex coefficient differential equations, the closed properties of the controllers were analyzed and stability properties established. Various feedback controllers are investigated and discussed. Both translational and angular dynamics compensators are developed, and measures of system stability and robustness to plant and operational speed variations are presented.

17. Key Words (Suggested by Author(s))	18. Distribution Statement
Modelling Control Magnetic Bearings	Unclassified—Unlimited Subject Category 31

19. Security Classif. (of this report)	20. Security Classif. (of this page)	21. No. of pages	22. Price
Unclassified	Unclassified	114	A06

NASA FORM 1626 OCT 86

NASA-Langley, 1988

For sale by the National Technical Information Service, Springfield, Virginia 22161-2171